Surrogate-Based Multi-Objective Optimization of Modulated Wave Laser Powder Bed Fusion Using Active Learning: Balancing Time and Quality

by

Thomas McCarthy

B.Sc. Mechanical Engineering, University of New Brunswick, 2023

A Thesis Submitted in Partial Fulfillment
of the Requirements for the Degree of

Master of Science in Engineering

in the Graduate Academic Unit of Mechanical Engineering

Supervisor: Clodualdo Aranas Jr., Ph.D., Mechanical Engineering

Examining Board: Rickey Dubay, Ph.D., Mechanical Engineering, Chair
Hamed Asgari, Ph.D., Mechanical Engineering
Saqib Hakak, Ph.D., Computer Science

This thesis is accepted by the Dean of Graduate Studies

THE UNIVERSITY OF NEW BRUNSWICK

February, 2025

ABSTRACT

Additive manufacturing, and more specifically laser powder bed fusion (LPBF), complements conventional manufacturing by producing a low volume of highly complex functional metallic components. The mode of laser emission, either continuous (c-LPBF) or modulated (m-LPBF), has a pronounced impact on the resulting component. Although both have merits, the c-LPBF process dominates commercial machines and academic efforts. To promote further exploration of m-LPBF, which has the potential to reduce defects and enhance microstructural control, the process must strike a balance between component quality and the industry's demand for increased production. In this work, a multi-objective optimization framework was adopted to balance time and quality of m-LPBF produced Ti-6Al-4V as a function of key processing parameters. Lacking an analytical model, Bayesian inference of Gaussian process regression was utilized to relate laser power, exposure time, point distance, and hatch spacing to the as-built relative density, serving as a proxy for quality, while batch active learning efficiently sampled the design space. In combination, this model accurately captured the relationship in a modest number of experiments and, in conjunction with the application of non-dominated sorting genetic algorithm II, was able to determine a non-dominated set of solutions approximating the Pareto front. Despite the model's accuracy, the current work highlights the need for a sufficiently large data set to accurately reflect the underlying mechanisms occurring in the m-LPBF process.

ACKNOWLEDGEMENTS

I’d like to express my sincere gratitude to my supervisor, Dr. Clodualdo Aranas Jr., who has provided mentorship, support, advice, and countless opportunities for personal and professional growth. Thank you for creating a space in which curiosity is encouraged.

To the past and present members of the ADRL team, thank you for the many laughs, memories, and conversations shared. May we all find the ever-illusive work-life balance.

To the members of my examining committee: Dr. Rickey Dubay, Dr. Hamed Asgari, and Dr. Saqib Hakak - thank you for offering feedback and guidance on my work. The unique perspective each of you has contributed to this project from your respective fields has no doubt resulted in a more well-rounded study.

To the TronosJet team, and particularly Mark Kirby and James Adye, thank you for taking the time to share your valuable insights on the LPBF process.

To my family and Bailey, thank you for sharing in my excitement in success, and disappointment in failures. Your unconditional support continues to be my foundation.

I’d like to acknowledge the individuals behind the research upon which this work is built. Your perseverance and dedication to your work have provided me with much inspiration, motivation, curiosity, and insight for which I am grateful.

Lastly, this work was financially supported by the National Sciences and Engineering Research Council of Canada and the New Brunswick Innovation Foundation. Without your financial support, this work would not have been possible.

Table of Contents

ABSTRACT ii

ACKNOWLEDGEMENTS iii

Table of Contents iv

List of Tables vii

List of Figures viii

1. Introduction 1

    1.1 Research Purpose, Significance, and Objectives 4

    1.2 Research Limitations 5

2. Literature Review 8

    2.1 Additive Manufacturing 8

    2.2 Laser Powder Bed Fusion 10

        2.2.1 Continuous vs. Modulated Laser Emission 11

    2.3 Titanium Alloy: Ti64 14

    2.4 Competing Interests: Porosity and Processing Rate 15

    2.5 Volumetric Energy Density 20

    2.6 Process-Property Modelling 22

        2.6.1 Surrogate Modelling in LPBF 24

    2.7 Frequentist vs. Bayesian Inference 27

2.8 Active Learning 31

2.9 Process-Property Optimization 35

2.10 Summary of Literature Review 40

3. Methodology 42

3.1 Materials, Manufacturing, and Experimental Measurement 42

3.2 Design of Experiments: Central Composite Design 44

3.3 Gaussian Process Regression 47

3.4 Active Learning: Batch Sampling..53

3.5 Multi-Objective Optimization: NSGA-II 55

4. Results and Discussion 59

4.1 Powder Characteristics...59

4.2 Initial Print: Central Composite Design 61

4.3 Model Configuration..63

4.3.1 Preliminary Model Configuration 63

4.3.2 Preliminary Model Convergence 65

4.4 Active Learning 69

4.4.1 Evolution of Marginal Posterior Probability Distribution 69

4.4.2 Experimental Learning Curves 75

4.4.3 Process Consistency 78

4.5 Model Inference..81

4.6 Multi-Objective Optimization: Pareto Front 86

5. Conclusion 90

Bibliography 93

Curriculum Vitae

List of Tables

Table 1. Nominal chemical composition of Ti64 powder [112]. 42

Table 2. Coded levels of the design space. 46

Table 3. Measured particle size distribution. 59

Table 4. Gaussian process model predictive performance with various model configurations (AARE [%], MSE). 64

List of Figures

Figure 1. Summary of research motivation and gap. 4

Figure 2. LPBF process schematic [46]. 11

Figure 3. Continuous vs. modulated laser emission temporal profiles [15]. 12

Figure 4. Simulation results of velocity field during keyhole pore bubble formation [58]. 17

Figure 5. Inter-track lack-of-fusion porosity formation mechanism [54]. 18

Figure 6. Effect of additional data on the posterior distribution [88]. 30

Figure 7. An illustrative example of a Pareto front in the objective space. 37

Figure 8. Illustrative 3-factor central composite design [73]. 45

Figure 9. a) Particle size distribution, and b) particle morphology. 60

Figure 10. a) Relative density measurements and the Logit transformed response, b) histogram of the relative density, and c) histogram of the Logit transformed relative density. 61

Figure 11. Trace of the marginal posterior distribution of a) β, b) σ_f^2, c) σ_n^2, d) ℓ_1, e) ℓ_2, f) ℓ_3, and g) ℓ_4 using the constant mean and squared exponential kernel functions over 11 independent sampling trials. The burn-in period is denoted by the dashed vertical line. The kernel density estimate of the sampled marginal distribution after the burn-in period for each trace is illustrated to the right. Positive density outside the support of the prior distribution is attributed to the kernel density estimate, as no samples exist in these regions. Marginal chains and distributions from each trial are plotted using different colors but become indistinguishable. 66

Figure 12. Running mean plot of the marginal posterior distribution of a) β, b) σ_f^2, c) σ_n^2, d) ℓ_1, e) ℓ_2, f) ℓ_3, and g) ℓ_4. The running mean considers only samples taken after the burn-in period using the constant mean and squared exponential kernel functions..........68

Figure 13. Evolution of the marginal posterior distribution of the hyperparameters a) β, b) σ_f^2, c) σ_n^2, d) ℓ_1, e) ℓ_2, f) ℓ_3, and g) ℓ_4. 70

Figure 14. Evolution of the likelihood function for each iteration of MCMC as a function of ℓ_4, a) $p\left(\boldsymbol{y_1}\middle|\beta^{(i)},\sigma_f^{2^{(i)}},\sigma_n^{2^{(i)}},\ell_1^{(i)},\ell_2^{(i)},\ell_3^{(i)},\ell_4\right)$, b) $p\left(\boldsymbol{y_2}\middle|\boldsymbol{y_1},\beta^{(i)},\sigma_f^{2^{(i)}},\sigma_n^{2^{(i)}},\ell_1^{(i)},\ell_2^{(i)},\ell_3^{(i)},\ell_4\right)$, c) $p\left(\boldsymbol{y_2},\boldsymbol{y_1}\middle|\beta^{(i)},\sigma_f^{2^{(i)}},\sigma_n^{2^{(i)}},\ell_1^{(i)},\ell_2^{(i)},\ell_3^{(i)},\ell_4\right)$, d) $p\left(\boldsymbol{y_3}\middle|\boldsymbol{y_2},\boldsymbol{y_1},\beta^{(i)},\sigma_f^{2^{(i)}},\sigma_n^{2^{(i)}},\ell_1^{(i)},\ell_2^{(i)},\ell_3^{(i)},\ell_4\right)$, and e) $p\left(\boldsymbol{y_3},\boldsymbol{y_2},\boldsymbol{y_1}\middle|\beta^{(i)},\sigma_f^{2^{(i)}},\sigma_n^{2^{(i)}},\ell_1^{(i)},\ell_2^{(i)},\ell_3^{(i)},\ell_4\right)$. 74

Figure 15. Evolution of the predictive distribution of the validation samples.................76

Figure 16. Error progression of both validation and testing data sets.............................77

Figure 17. a) Levene's test of homogeneity (p=0.009). Confidence intervals of variance estimates with Bonferroni correction for family-wise significance, $\alpha = 0.05$, and b) Welch’s ANOVA with unequal variance (p=0.677) with Games-Howell multiple comparisons..79

Figure 18. Predicted Logit relative density as a function of exposure time and point distance. Hatch spacing of a) 30 µm, b) 50 µm, and c) 70 µm. The dashed white lines indicate constant equivalent velocity...82

Figure 19. Effect of laser power and exposure time on power density. 83

Figure 20. Pareto front: relative density and build rate. Region (1) indicates relative density less than 90 %, region (2) indicates relative density between 90 % and 99 %, and region

(3) indicates relative density greater than 99 %. The slope is illustrative and not to scale, or representative of the precise data used in its approximation. 87

1. Introduction

Since the Industrial Revolution, the manufacturing industry has continued to grow and evolve based on the pursuit of efficiency and scale. Most recently, the fourth Industrial Revolution, termed Industry 4.0, has introduced novel technologies with unprecedented advantages. Of these technologies, additive manufacturing (AM) has received notable attention for its ability to produce functional components in a variety of high-impact industries while providing enhanced design freedom in addition to economic and environmental benefits.

Among AM technologies, laser powder bed fusion (LPBF) has emerged as a frontrunner for metallic materials, including the prominent titanium-based Ti-6Al-4V (Ti64) alloy, due to its ability to fabricate complex components with relatively high dimensional accuracy; however, it is characterized by a low material processing rate limiting its application to the small-scale production [1], [2], [3], [4], [5], [6], [7], [8], [9], [10], [11]. LPBF technologies can be further distinguished by their mode of laser emission: specifically modulated emission (m-LPBF), otherwise referred to as pulsed, which intermittently transfers energy to the powder bed, and continuous emission (c-LPBF), characterized by a continual transfer of energy [12], [13]. Despite inconclusive evidence on the merit of each emission mode, c-LPBF dominates commercial machines and, by extension, academic efforts [12], [14], [15]. This indicates a need for further research on its m-LPBF counterpart.

A significant body of literature has previously established that the quality of AM printed components, for which porosity, or equivalently relative density, often serves as a proxy, largely depends on the processing parameters. Researchers have identified four primary parameters as having a pronounced effect on the c-LPBF process: laser power, scan speed, hatch spacing, and layer thickness [5], [16], [17], [18]. Considering m-LPBF, the problem's dimensionality increases through independent control of exposure time and point distance, which in turn define an equivalent scan speed [17], [19], [20].

At this point, it is typically suggested that improper selection of these parameters can result in process-induced porosity and undesirable mechanical properties, thus hindering the further adoption of AM in industries with demanding quality standards. Nevertheless, it has recently been argued that some finite amount of porosity within as-built parts may be acceptable under certain circumstances, for example, as in Refs. [4], [9], [21]. In these cases, porosity can be exchanged for increased productivity. Thus, a multi-objective framework can be considered that more accurately captures the competing interests faced by practitioners, including the balance between time and quality.

Irrespective of what level of porosity, if any, is acceptable to the practitioner, accurate models for the objectives of interest are typically required to optimize the process [5]. Previous research has established simple analytical relationships relating processing parameters to build rate, representing the productivity or time of the process. Nevertheless, due to the complex nature of AM, there are currently no closed-form analytical process-property relationships, and therefore, costly experimental methods are often used to determine appropriate processing conditions [22], [23]. To mitigate the costly nature of determining suitable processing conditions, researchers have developed numerous empirical relationships and approximations to model the LPBF process and resulting properties based on two distinct multi-disciplinary methods: physics-based and data-driven

[24], [25]. Despite being able to accurately capture the process, the computational burden of physics-based methods can make them unsuitable to be used with iterative optimization methods [26], [27]. Alternatively, data-driven approaches utilize recent progress in applied mathematics, statistics, and computer science. In such a manner, they are able to efficiently make inferences on unobserved conditions based on observed data [26], in essence approximating the relationship between independent and dependent variables. In conjunction with an appropriate optimization algorithm, these methods offer the ability to achieve desirable mechanical properties and an acceptable compromise between quality and time for a given application.

The essence of the above is captured in **Figure 1**, from which this work lies at the intersection. Despite insufficient evidence to suggest a favorable mode of laser emission under all circumstances, c-LPBF dominates the commercial market, and by extension, limited exploration of m-LPBF has been performed. To promote further exploration of the m-LPBF process, an understanding of the effects of processing parameters on qualities of interest must first be established. Although the most prominent quality of interest is relative density, recent work, including Refs. [4], [21], suggests that the industry may be willing to prudently sacrifice relative density in certain cases in exchange for increased productivity. Considering this as a multi-objective optimization problem, each objective must be expressed as a function to determine the complete tradeoff between quality and productivity. A simplified analytical function can be used for build rate as a proxy for productivity; however, data-driven models must be established for relative density. Supervised data-driven methods rely on large quantities of labeled training instances, which may be prohibitively expensive for metal-based AM processes. This promotes the application of active learning, a method of intelligent and intentional sampling, as a strategy to efficiently establish an effective model with limited data. To this end, it is hypothesized that the integration of data-driven modelling, active learning, and multi-objective optimization will be able to determine the tradeoff between productivity and quality of m-LPBF printed components and promote the further exploration of this form of LPBF.

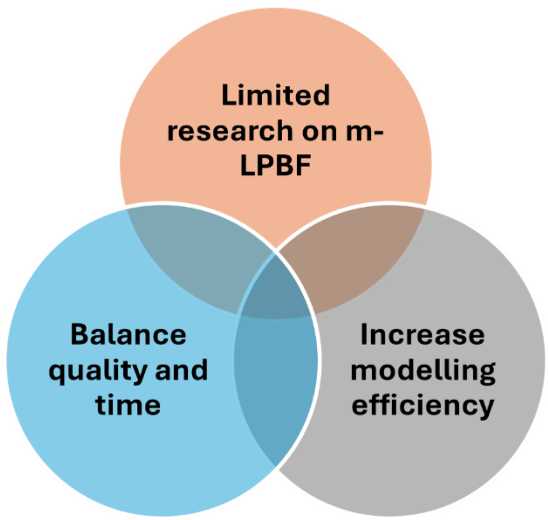

Figure 1. Summary of research motivation and gap.

1.1 Research Purpose, Significance, and Objectives

The double-edged sword of AM is that the complexity that allows the economic, design, and environmental benefits of the process also leads to a limited understanding of the phenomena taking place and their effects on the resulting mechanical properties. For metal-based AM, significant effort has been devoted to c-LPBF leading to increased technological maturity; however, limited research has been devoted to its m-LPBF counterpart. As a result, it could be argued that the potential applications of m-LPBF remain relatively unexplored. Trends within literature have arguably suggested that the first step towards technological maturity for c-LPBF has been mitigating process-induced defects. In fact, Ref. [28] suggests that this should be the first optimization step in material research and development when considering LPBF. Nevertheless, as mentioned above, it has also been suggested that an acceptable level of porosity may exist in exchange for increased productivity. To this end, to further promote the exploration of m-LPBF it is necessary to determine the relationship between quality and time of m-LPBF manufactured components.

This work addresses this gap by leveraging recent progress in LPBF process modelling. With the overarching objective of determining the relationship between quality and time in m-LPBF Ti64 as-built components, this work can be decomposed into the following sub-objectives:

- Efficiently develop a data-driven surrogate model to relate key m-LPBF processing parameters to relative density, a proxy for quality, of Ti64 as-built components using an active learning framework.
- Interpret the data-driven model with respect to the literature's current understanding of the physical process to determine its ability to capture the expected underlying mechanisms.
- Determine the relationship between the quality and processing rate of Ti64 as-built components using a multi-objective optimization framework.

1.2 Research Limitations

Although significant progress is enclosed within the following dissertation toward its objectives, the following principal limitations are noted for the current study:

- In this study, the project timeline and allocated resources constrained active learning to a total of three iterations, including the initial sampling. Thus, the effect of additional iterations can only be hypothesized as in **Section 4.4.1**. Furthermore, without additional resources, samples from the obtained non-dominated set of solutions could not be printed. Thus, the accuracy of the obtained solutions can only be estimated by the accuracy observed on the testing and validation data sets.
- Archimedes method is a cost-effective technique to obtain bulk measurements of the relative density of metal-based AM components. Nevertheless, its implementation is often complicated by the surface roughness of the printed component, which, in conjunction with the properties of the measuring fluid, can cause variability in experimental measurements. In the current work, the design space considered includes undesirable process parameter combinations, which are expected to result in unstable prints and increased surface roughness, further amplifying the limitations mentioned above. X-ray CT is an alternative approach for considering bulk density; however, this method is prohibitively expensive for the current study and introduces its own limitations.
- The Gaussian process regression model utilized in this work assumes independent and identically distributed normal noise on the transformed observations. Although commonly used, incorporating a more flexible error structure that accounts for heteroskedasticity, and potential non-normality could enhance the predictive performance of the Gaussian process model.
- Lastly, in the current practical application of active learning, it is not possible to observe whether the obtained results outperformed other query strategies or even

baseline random sampling. An interesting discussion related to determining a suitable active learning strategy for practical implementation can be found in Ref. [29]. Furthermore, the active learning process involves a degree of randomness. In the current study, sources of randomness include generating the posterior distribution through sampling and creating a subpopulation from the larger unlabeled pool. As a result, variability is expected between replicate experiments. On its own, it cannot be concluded whether the expected behavior of the chosen query strategy is superior to alternative active learning strategies, and the efforts required to draw such conclusions are prohibitively expensive.

2. Literature Review

2.1 Additive Manufacturing

Society has been using layer-wise construction for thousands of years; however, Beaman and their co-authors argue it was not until the early 20th century that any process resembles what we currently consider AM [1]. Beaman, a pioneer in the field of AM and an early developer of powder bed fusion, provides a comprehensive historical perspective on the development of AM [1]. In their work, they highlight that Baker's 1925 patent [30], which was assigned to Westinghouse Electric and Manufacturing Company, could be considered the first metal AM process in which they described a method of using a fusible metal electrode to create objects using a series of superposed layers. However, without a digital model, they suggest that this description falls short of the common perception of modern AM and that a clear differentiation between a simple layer-wise manufacturing method and modern AM was provided by ASTM, which is currently the most widely adopted definition of the process [1], [3].

> *"Additive manufacturing (AM), n—*a process of joining materials to make objects from 3D model data, usually layer upon layer, as opposed to subtractive manufacturing methodologies"

The ASTM standard further classifies AM into 7 categories based on the process and feedstock [1], [31]: namely binder jetting, directed energy deposition, material extrusion, material jetting, powder bed fusion, sheet lamination, and vat photopolymerization. Within the 7 classifications of AM, LPBF has been suggested to be among the most prominent techniques for manufacturing metallic functional components, according to Ref. [7], representing more than 50% of the metal-AM market, due to its high dimensional accuracy; however, the process suffers from low processing rates [1], [2], [3], [4], [6], [8], [9], [11], [32].

It rarely goes unsaid in AM literature that compared to conventional methods, AM offers numerous unprecedented benefits. These benefits include but are not limited to enhanced design freedom, material efficiency, on-demand manufacturing, repairing components, and potential reduction of environmental impact [2], [3], [9], [33], [34], [35], [36]. Due to the layer-wise manufacturing style AM is based upon, complex geometries with internal cavities can be created, lending the process to applications ranging from biomedical implants to aerospace components [33], [34], [37], [38], [39].

In their reviews of AM, Refs [3] and [34] highlight various benefits of AM and opportunities for future research efforts, among which particular attention is devoted to economic and environmental benefits. Due to the significance of these benefits to today's society and the manufacturing industry, the key findings of their reviews are briefly summarized in the following paragraphs and supplemented where required. Conventional manufacturing requires large capital expenses in the form of tools, dyes, lubricants, and other auxiliary resources resulting in a large cost-per-unit with low production volumes [3], [34]. As the quantity of production increases, the cost-per-unit decreases: a phenomenon known as economy of scale. Inversely, AM offers a fixed cost-per-unit and opens opportunities for cost effective low volume manufacturing [1], [40]. Furthermore, AM offers the potential to disrupt the conventional supply chain, with it being suggested that local AM facilities can eliminate the need to transport products long distances and maintain large inventories [3], [34], [36], [41]. Alternatively, an on-site on-demand manufacturing model could be adopted, minimizing traditional non-value-added expenses [3], [34].

In addition to economic and design incentives, Refs. [3] and [34] highlight that AM offers a potentially environmentally conscious alternative to conventional manufacturing methods. As an example, considering the passenger aerospace industry in the United States, Ref. [33] estimated that if rapid adoption is achieved, AM has the potential to reduce energy consumption by as much as 1.2 – 2.8 billion gigajoules of energy consumed and 92.1 – 215.0 million metric tons of greenhouse gas emissions between 2014 and 2050 – a result directly aligning with Canada's net zero emission initiative [42].

2.2 Laser Powder Bed Fusion

Attributed to Carl R. Deckard, powder bed fusion is the process of selectively fusing metallic, plastic, ceramic, or composite powder to create components in a layer-wise fashion [1], [43]. Powder bed fusion can be further characterized by the heat sources used: particularly laser-based or electron-beam-based [2], and whether or not the powder feedstock is fully melted or sintered. Considering LPBF, the process first deposits a thin layer of powder over a substrate material, from which a slice of the desired component's cross-sectional area is selectively scanned, thus fusing the current and previous layer [2]. The substrate is lowered by a predefined distance, a new layer of powder is deposited over the previously scanned cross-section, and the process is iterated until the full component is formed [2], [37], [38]. Additional techniques have been proposed to improve the quality of the manufactured component including preheating the powder bed to reduce residual stresses [44] and introducing a shielding gas to eliminate oxidation of the molten material [45]. Subtle distinctions can be made between commercial machines [12], [14]; however, a full schematic of the overarching LPBF process is shown below in **Figure 2** [46].

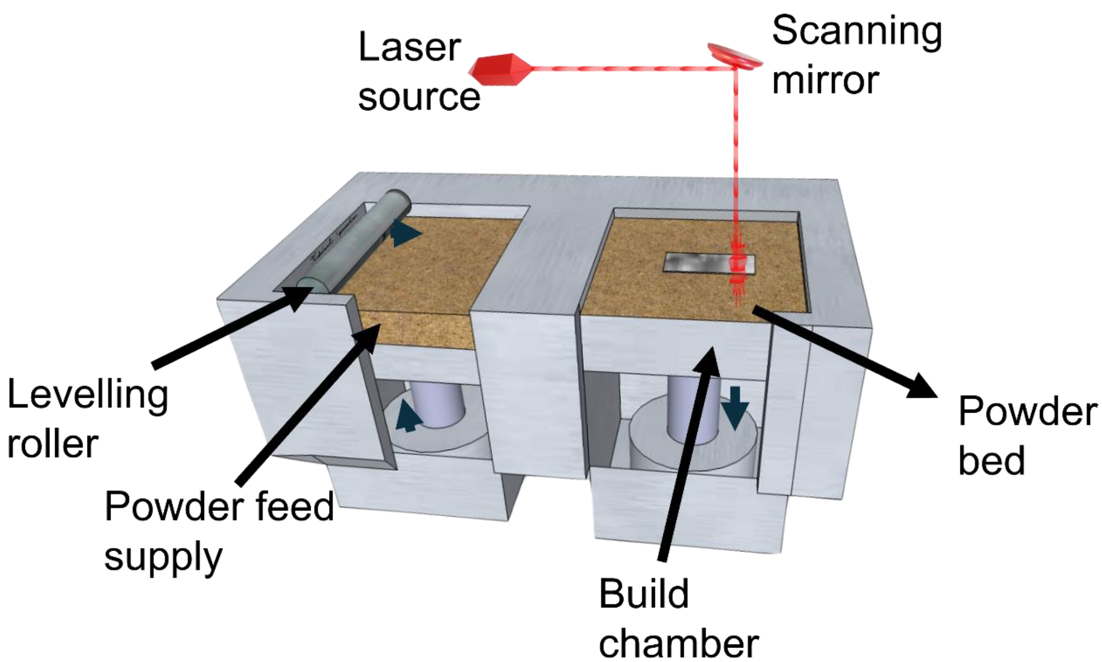

Figure 2. LPBF process schematic [46].

2.2.1 Continuous vs. Modulated Laser Emission

An often-overlooked nuance of the LPBF process is the emission mode of the laser energy source. Two distinct modes of laser emission can be found in commercial machines distinguished by their temporal profiles, as illustrated in **Figure 3** [15]: namely continuous and modulated emission [12], [15].

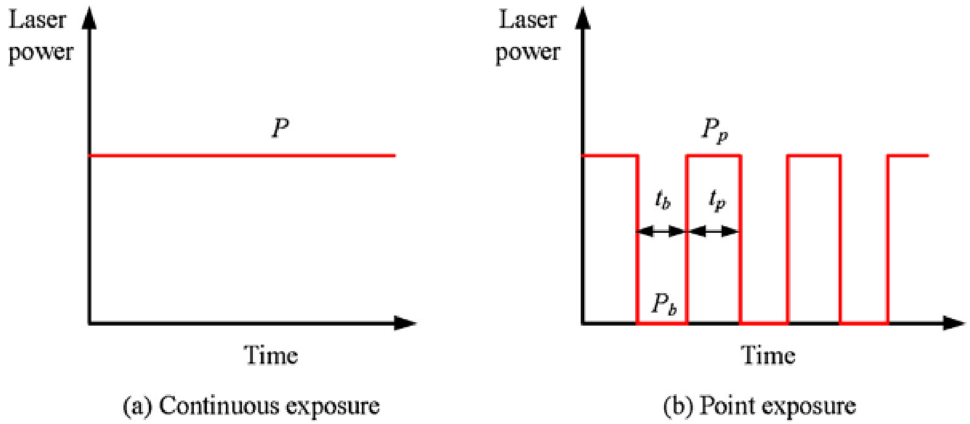

Figure 3. Continuous vs. modulated laser emission temporal profiles [15].

Continuous laser emission is characterized by the sustained transfer of energy between the laser energy source and powder bed along the scanning path [13]. As a result, under suitable conditions, a continuous and uninterrupted melt pool is formed [13]. Under c-LPBF, four parameters are typically regarded as having the most influence over the process: laser power, scanning speed, hatch spacing, and layer thickness [16], [17], [18]. On the other hand, modulated laser emission is characterized by the intermittent transfer of energy from the laser to the powder bed along the scanning path [13]. Under this mode of emission, the dimensionality, and thus the control over the process, is increased by decomposing the scanning speed into exposure time and point distance [17], [19], [20]. In addition, exposure time can be related to the duty cycle and, in turn, the average power of the modulated wave [14]. It is worth noting that although **Figure 3 (b)** illustrates an ideal square waveform, its implementation results in the presence of a rise and fall time describing the time required to vary the signal from its low to high and high to low states, respectively [47].

Compared to its m-LPBF counterpart, c-LPBF dominates the commercial LPBF market and has, by extension, received a disproportionate amount of research efforts in literature [12], [14], [15]. In fact, in their literature survey, Demir et al. [14] found that only 69 of 1966 publications on selective laser melting, one of the alternative names for LPBF [38], employed modulated laser emission between 1997 and 2016. Based on this inequality, it would be expected that c-LPBF has demonstrated repeated and undisputed dominance over m-LPBF; however, no such dominance has been established. In fact, there remains ambiguity over the superiority of each mode of emission [14].

Demir et al. [14] suggest that compared to c-LPBF, m-LPBF allows greater control over the heat introduced to the system, making it suitable for small or heat-sensitive components. Using a simulation study, Ding et al. [15] found that under the same input energy, m-LPBF yielded higher peak temperatures in the melt pool and faster cooling rates, leading to finer microstructural features. Furthermore, the enhanced control over the heat introduced, and by extension the resulting microstructure, has been suggested to make m-LPBF more suitable for printing highly crack-susceptible materials [13]. On the other hand, Demir et al. [14] demonstrated that the transition from m-LPBF to c-LPBF is accompanied by an increase in relative density at the expense of a decrease in dimensional accuracy – trends which they attribute to a corresponding increase in melt pool width. Thereafter, Biffi et al. [12] found that under optimal processing parameters, both modes of laser emission are suitable for producing high-density components; however, they found that under optimal processing conditions, m-LPBF produced a higher crystallographic texture and, as a result, exhibited higher anisotropy.

It is not the goal of this summary to identify a superior mode of emission for the LPBF process under all circumstances, but rather to suggest that both modes of operation have merit and may be suitable for different applications. As a result, it is argued that further efforts are required towards m-LPBF to reach the same level of maturity as its c-LPBF counterpart. Due to the disproportionate amount of literature, both c-LPBF and m-LPBF are discussed herein, with the distinction between the laser emission mode only made when relevant.

2.3 Titanium Alloy: Ti64

As the most widely used titanium alloy in industry, significant efforts and resources have been devoted to understanding the properties of LPBF-processed Ti64 [2], [3], [38]. Fortunately, the overwhelming wealth of literature on this alloy system has been synthesized by various researchers – notably to the current work is the reviews of Cao et al. [38] and Bartolomeu et al. [37]. Since the current work focuses on process modelling, a complete discussion of the complex metallurgical phenomena related to this material system during LPBF is omitted from this work. The reader is referred to the wealth of literature for more details; however, for the sake of completeness, the above works and fundamentals are briefly summarized.

Known for its superior specific strength, excellent corrosion resistance, and biocompatibility, Ti64 is classified as an $\alpha+\beta$ alloy owing to the presence of both α stabilizing (Al) and β stabilizing (V) elements [37], [38]. This alloy can exhibit a hexagonal close-packed structure known as α-phase and a body-centered cubic structure known as β-phase [2], [37], [38]. Due to the high cooling rates induced by the LPBF process, the rapid solidification of the melt pool results primarily in the transformation of β to a martensitic phase known as α', resulting in increased hardness and strength at the expense of the ductility of the material in its as-built state [2], [37], [38]. In fact, Bartolomeu et al. [37] summarize that yield and tensile strengths of LPBF Ti64 can be found in the literature to range from 802-1273 (MPa) and 960-1421 (MPa), respectively – values they suggest can exceed the minimum requirements of Ti64 for medical implants and aerospace components. Despite the increased strength, the same report found that the tensile strain was found in the literature to be between 1.4 – 12.7 (%) [37], the majority of which fall below the minimum requirements [37], [38]. The ductility of the material can be restored through heat treatment at the expense of a reduction in strength, and an acceptable compromise between ductility and strength can be achieved for heat-treated LPBF-processed Ti64 [37], [38]. Similar results were observed in Ref. [48]. This indicates that LPBF offers an effective way to manufacture complex components using Ti64 without detrimentally affecting the resulting mechanical properties.

2.4 Competing Interests: Porosity and Processing Rate

As a relatively new manufacturing process when compared to conventional methods, many current limitations of AM remain to be resolved. Amongst others, these include the limited compatible materials, variability in mechanical properties, processing defects, post-processing requirements, capital costs, build volumes, and processing rates [1], [3], [9], [33], [34], [49], [50], [51]. Among these, the interplay between porosity and processing rate of as-built components, competing objectives that depend on the chosen processing parameters [9], is particularly important to LPBF and the current study.

As one of the principal defects discussed in literature, considerable research efforts have been devoted to understanding and preventing porosity, and its detrimental effects are now well understood [31]. Tensile testing indicated that pores can act as crack initiation sites, leading to poor ductility and defect-driven failure [49], while wear performance has been shown to be adversely affected by the presence of porosity [52]. Similarly, fatigue life has been shown to be dependent on the shape, quantity, and position of pores with high porosity leading to crack initiation and a decrease in fatigue life [53]. DebRoy et al. [2] summarize that porosity can be attributed to three principal mechanisms, namely keyhole formation, gas entrapment, and lack of fusion – each of which is clearly summarized in their original review. As in the work of Yang et al. [54], gas entrapment, which is typically related to material feedstock, for example either through powder atomization [55] or recycling [56], is not of primary concern to the current study.

Keyhole melting occurs when excessive energy is introduced into the material causing vaporization within the melt pool. This can be observed either along the melt pool track, but also in areas where the laser changes directions [9], [39], [57], [58]. Wang et al. [58] report two stages involved in keyhole pore formation: bubble formation and solidification. First, the recoil pressure of the vaporized material results in a depression on the print surface and allows deeper penetration of the laser, hence a deeper melt pool is observed [9], [54], [59]. The keyhole bubble is formed due to the collapse of the melt pool depression; however, different theories have been presented for the driving mechanism of the collapse. For example, Khairallah et al. [57] primarily attributed this collapse to the reduction in recoil pressure and the increase in surface tension forces as the temperature of the melt pool decreases, whereas Wang et al. [58] utilized simulation models to relate the collapse of the keyhole to a strong reverse flow within the melt pool as illustrated in **Figure 4**. Irrespectively, the pore is formed when it becomes entrapped by the solidification front [54], [58].

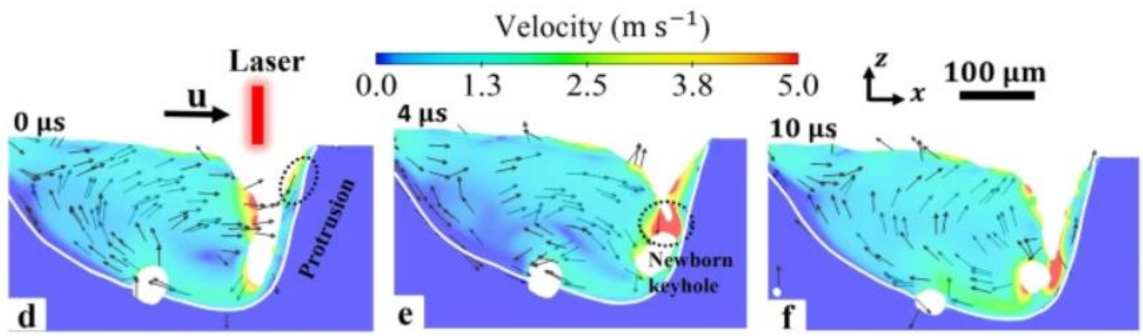

Figure 4. Simulation results of velocity field during keyhole pore bubble formation [58].

Unlike keyhole porosity, which is attributed to excessive energy density, lack of fusion can be attributed to insufficient energy density [39], [54]. As a result, inadequate melt pool overlap is observed, leading to inter-track and inter-layer voids [54], [60]. Typically, lack of fusion porosity is described as large, irregularly shaped pores containing both atmospheric gas originally present in the powder bed and unfused or partially fused particles [39], [54]. An illustrative example of the formation of inter-track lack of fusion porosity is presented in **Figure 5** [54]. Whereas it was briefly mentioned above that keyhole porosity can be exacerbated when changing scanning directions, the simulation work of Yang et al. [54] illustrated that lack-of-fusion porosity could be promoted by surface roughness causing inhomogeneous powder distributions and an increase in effective layer thickness due to shrinkage of the previous layer.

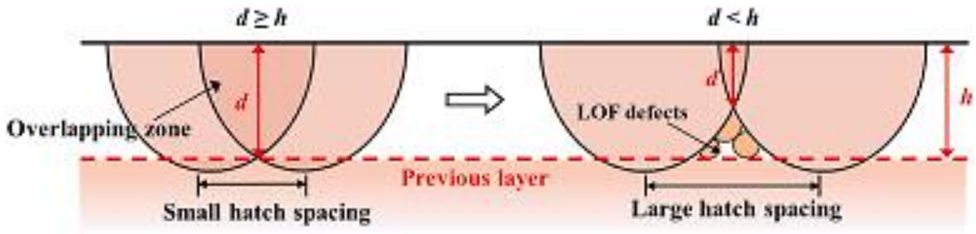

Figure 5. Inter-track lack-of-fusion porosity formation mechanism [54].

The key takeaway of the above description of the formation mechanisms of keyhole and lack of fusion porosity is that they are directly related to the energy applied to the powder bed. At a high level, insufficient energy results in partial melting and lack of fusion, while excessive energy results in highly complex unstable melt pools that form porosity upon collapse and solidification. Porosity then becomes a Goldilocks problem in which insufficient or excessive energy is detrimental to the process, a balance between which must be obtained. As discussed in **Section 2.5**, energy is directly related to the processing parameters. Thus, processing parameters directly control the absence or the formation of porosity within the as-built component.

Based on the detrimental effects of porosity on the resulting mechanical properties, it is not surprising that a large body of literature focuses solely on the mitigation and elimination of porosity in as-built LPBF components. In such cases, a lower bound of the success criteria typically is relative density exceeding at least 99 % as in the works of Refs. [4], [14], [17]. If mitigating porosity continues to be considered the sole objective, low processing rates will continue to restrict the LPBF process to the production of high-value, low-volume components [4], [10]. Furthermore, the simulation study performed by Ding et al. [15] suggested that the processing rate of m-LPBF may be inferior to that of c-LPBF under equivalent parameters, only exacerbating the hindrance. To promote the potential abilities of m-LPBF, the processing rate must be considered as a primary objective.

Even in the most stringent industries where 99.9 % relative density is required, the work of Schwerz et al. [10] showed that incorporating the processing rate as an objective can yield a 10-fold increase in build rate with negligible change in tensile properties and reduced texture by properly tuning the processing parameters. However, the allowable defects within printed components are highly dependent on their type, size, and the desired application of the component [10], [61]. Hyer and Petrie [21] argue that components may exist for which it is acceptable to sacrifice mechanical properties by intentionally inducing porosity in exchange for increasing processing rates. Alternatively, Oliveira et al. [9] describe a situation in which local processing parameters can be determined with various levels of induced porosity based on the load distribution within the component. Nevertheless, Ti64 is an expensive alloy with highly desirable mechanical properties. In the case that a sacrifice in mechanical properties, either at a global or local level, is acceptable, it may be more beneficial to reduce the cost of the component by reconsidering material selection or exploring topology optimization. Although possible, the author perceives that a more probable case in which porosity may be acceptable, and the case considered in the current study, is when post-processing treatments are applied irrespective of the printed state. In any case, porosity can be exchanged for increased productivity; however, their tradeoff must be further understood [21].

LPBF printed components, especially when processed using m-LPBF, exhibit high anisotropy compared to their conventionally manufactured counterparts [12]. Hot isostatic pressing (HIP), the process of plastically deforming near-net-shaped as-printed components at elevated temperatures, can eliminate anisotropy and, as a by-product, enclose porosity due to multi-axial compressive loading [4], [38], [62]. In effect, it may be argued that HIP serves as a method of microstructural control while reducing processing-related defects. In cases where HIP is applied for microstructural control, it may be beneficial to induce a certain amount of as-printed porosity to increase the overall processing rate [4], [63]. Despite excessive initial lack-of-fusion porosity, Kaletsch et al. [63] showed that printed IN718 samples subjected to a combined HIP and aging post-processing procedure could reduce porosity from 9.9 % to below 0.3 %. Their results achieved higher fatigue properties than as-built samples which attained 99.9 % relative density and were subjected to conventional heat treatment. Similarly, by defining a 5 % porosity threshold, Herzog et al. [4], found that a wider processing window could obtain near fully dense components when subjected to HIP. Accounting for upscaling the component to account for the compressive deformation, their illustrative example suggested that combining LPBF with HIP can still reduce the combined processing time.

2.5 Volumetric Energy Density

Despite perhaps appearing complex, at its core, LPBF is simply a process governed by the energy within its system. Thus, even if just for a historical perspective of process optimization, a review of LPBF would not be complete without at least a brief discussion of its volumetric energy density (VED). As one of the first methods to optimize the process, VED has been widely adopted by the research community as a method of reducing the complexity of LPBF by relating influential processing parameters to a single metric [50]. VED is typically described as a measure of the energy introduced to the powder per unit volume [17], [64]. For c-LPBF systems, VED is expressed as **Eq 1** where P (W) is the laser power, v (mm/s) is scanning speed, h (mm) is hatch spacing, and t (mm) is layer thickness [15], [50], [64]. Considering independent control over exposure time, ET (s), and point distance, PD (mm), and assuming no losses, the VED of a m-LPBF system can be expressed as **Eq 2** [13], [15], [17].

$$VED = \frac{P}{vht} \quad \textbf{Eq 1}$$

$$VED = \frac{P \cdot ET}{PD \cdot h \cdot t} \quad \textbf{Eq 2}$$

A wealth of literature has used VED as a method of optimizing the LPBF process, the process of which is well established within the field. A brief overview of the overarching theme is as follows: traditional volumetric energy density methods involve plotting volumetric energy density versus the observed porosity or another quality indicator to graphically determine an optimal range. Considering porosity, from this plot, a range of VED is identified as *'optimal'* if its porosity is below a defined threshold. Although many researchers have developed optimum processing conditions based on VED, energy density does not adequately capture the complex physics taking place in the LPBF process [65]. Notably, VED fails to account for the various parameter sets which can be chosen to achieve a single energy density [8], [13], [17], [19], [66], [67]. For example, in the highly cited work of Scipioni Bertoli et al. [65], it was shown that for single-track scans, an increase in both laser power and scan speed at constant energy density caused the surface morphology to transition from smooth to irregular, and finally discontinuous. Highlighted in the work of Liu [50], similar findings were reported in the work of Prashanth et al. [68]

which indicated that the tensile properties (yield strength, ultimate tensile strength, and ductility) decrease as laser power and scan speed are decreased at constant energy density. The author attributed this to the corresponding decrease in relative density from 99.5 % to 40 %. Combined, these two examples illustrate that a given VED alone is not indicative of the expected quality of a component. Due to the insufficient description of the LPBF process provided by VED, a more robust methodology is required [69].

2.6 Process-Property Modelling

Having identified the shortcomings of VED, significant research has been devoted to modelling the LPBF process accounting for the independent effects of its most prominent processing parameters. There are two methods in which this can be accomplished: either physics-based or data-driven [24], [25]. Many researchers have attempted to address this problem using both approaches, creating a large body of diverse literature. In summary, physics-based modelling takes advantage of recent computational techniques, such as finite element methods and computational fluid dynamics, to simulate melt pool dynamics and the resulting effects. Various models have been developed with the capability of considering, for instance, three-dimensional fluid dynamics and heat transfer, time-dependent recoil pressures, and particle distributions [57]. Although valuable in understanding the underlying phenomena taking place, for example, they were relied on heavily in **Section 2.4** to describe the porosity formation mechanisms, Refs. [26], [27] suggests these methods can be impractical when optimizing the process due to their large computational expense. As an alternative, data-driven techniques have been applied to reduce computational and experimental expenses by using observed data to make inferences about unobserved conditions [26].

Surrogate models, sometimes referred to as meta models or response surfaces [70], are the approximation of an unknown or expensive function in terms of a simple model. In conjunction with a suitable optimization algorithm, a surrogate model can act as the objective function and be used to efficiently determine an optimal point within a given design space [71]. This is referred to as surrogate-based optimization. As noted by Tapia et al. [27], surrogate modelling is typically discussed in reference to approximating expensive simulations using a simpler and more efficient model; however, at its core, surrogate modelling is the process of approximating the relationship between input feature vector, $\boldsymbol{x}$, and an observed response, y, based on limited data to make useful predictions [70]. Thus, as they originally argued, surrogate modelling is not only suitable for approximating expensive simulations but also for experimental data [27]. Therefore, in the present work, a more general perspective of surrogate modelling is adopted as a general framework that can approximate the underlying process of either simulation or experimental results based on limited observations.

The surrogate modelling process begins with the design of the experiment [71]. This stage defines a set of experiments that minimizes the experimental cost and maximizes the information obtained [72]. The data is then collected at parameter combinations identified by the experimental plan [71], in this study considered either through simulation or physical experiments, and the chosen surrogate model is constructed. The model's accuracy is tested and if acceptable, the model can be used. If not, further design points are generated, and the model is reconstructed until an acceptable level of accuracy is achieved

[31]. It is worth noting that there is evidence to suggest that by using surrogate models to approximate simulation data, there exists a risk of amplifying the inherent error of the simulation; however, these effects appear minimal in the recent works on LPBF in Refs. [26], [27].

2.6.1 Surrogate Modelling in LPBF

In general, in line with the formulation presented in Ref. [73] for the response surface methodology, it is assumed that the process can be described by **Eq 3**, where y is observed response, $f(\boldsymbol{x})$ is the unknown underlying process of design vector $\boldsymbol{x}$, and ε is the error term capturing the response's variability. The problem of surrogate modelling can then be expressed as finding a suitable function $\hat{f}(\boldsymbol{x})$ that adequately captures the underlying process [71].

$$y = f(\boldsymbol{x}) + \varepsilon \qquad \textbf{Eq 3}$$

As a key ingredient of the response surface methodology, multiple linear regression (MLR), typically taken as a low-order polynomial, can be used to model the relationship between a set of designs and their respective responses within a given design space [73], [74], [75]. Specifically, the second-order model is expressed as **Eq 4** [73], where β_0, β_j, β_{jj}, β_{ij} are the intercept, linear, quadratic, and interaction terms of the design vector.

$$f(\boldsymbol{x}) = \beta_0 + \sum_{j=1}^{k} \beta_j x_j + \sum_{j=1}^{k} \beta_{jj} x_j^2 + \sum_{i<} \sum_{j=2}^{k} \beta_{ij} x_i x_j \qquad \textbf{Eq 4}$$

Arguably the most popular surrogate model in engineering design [70], MLR has been widely applied as a method of approximating the LPBF process [8], [16], [66], [67], [69], [69], [76], [77], [78], [79]. Among the benefits of the MLR model is its simple expression, closed-form solution of the model parameters, and given certain statistical assumptions are obeyed, the ability to test for the significance of the model terms [7], [16], [73], [80]. Taking advantage of these benefits, Kuo et al. [81] developed a multiple linear regression model relating laser power, point distance, and exposure time to the relative density and dimensional accuracy of m-LPBF manufactured Ti64 on a pure titanium substrate. Although widely applied, Forrester and Keane [70] suggest polynomial regression has been shown to be inadequate when modelling non-linear, multi-modal, and higher dimensional problems, while Zhai and Chen [75] suggest using MLR may lead to optimizations of little significance. Due to these limitations, it is important to consider more accurate models that can capture the complexities of the AM process [75].

As an alternative to the MLR model, Gaussian process regression has recently been the recipient of increased attention in LPBF process modelling. Largely contributing to its recent popularity is the model's high accuracy for small data sets, its inherent approximation of the standard deviation of the predicted response, and its interpretable nature [22], [27], [28], [75], [82], [83]. The model assumes that the observed data can be represented by a joint Gaussian distribution, where similar inputs are expected to yield similar outputs [84]. The model’s covariance or kernel function, $k(\boldsymbol{x}, \boldsymbol{x}')$, is used to determine the degree to which the response at two inputs are similar, while the mean function, $m(\boldsymbol{x})$, describes the expected value [18]. Combined, these two functions uniquely define the Gaussian process model. The general form of the Gaussian process regression model is shown in **Eq 5** [7], [84].

$$f(\boldsymbol{x}) \sim GP(m(\boldsymbol{x}), k(\boldsymbol{x}, \boldsymbol{x}')) \qquad \textbf{Eq 5}$$

Regarded as one of the first to introduce Gaussian Process regression into metal-based AM, Tapia et al. [31] developed a framework to predict process-induced porosity as a function of key processing parameters using a Gaussian process model. In their influential work, their framework demonstrated promising results with a linear trend and Matérn ½ kernel achieving a cross-validated mean square predictive error of 0.2593, albeit over a limited parameter space [31], [83]. Following their own work, Tapia et al. [27] later demonstrated that their Gaussian process framework could generate processing windows based on limited experimental or simulation data by predicting the ratio of single-track melt pool depth to width as a function of laser power and scan speed – work later confirmed by Ref. [26].

Applying a similar Gaussian process model, Liu et al. [83] demonstrated that a wider range of optimal processing parameters can be obtained using this approach resulting in previously unattainable mechanical properties. As a result, it was suggested that desirable properties can be obtained without the need for a heat treatment process if the design space is exhaustively searched. Later, the same author illustrated that the hyperparameters of Gaussian process regression can provide insight into the underlying influence of the design variables and be related to the physical mechanisms, thus resulting in a more interpretable model [28].

Using Ti64, Maitra et al. have repeatedly illustrated the superior predictive ability of Gaussian process regression over MLR by modelling relative density [16], surface roughness [80], and hardness [7] based on an aggregation of data available in literature. Despite providing compelling and repeated evidence for the adoption of their framework, their data aggregation combines m-LPBF and c-LPBF observations by reducing exposure time and point distance to an equivalent scan speed and therefore does not capture their independent influence on the process. Thus, their model is not expected to be able to predict the response of the m-LPBF Ti64 fabricated components. Based on the above select examples and a growing body of supporting literature including, for example, Refs. [23], [52], [85], Gaussian process regression has repeatedly demonstrated the ability to model the LPBF process-property relationship for various properties, materials, and feature dimensions, presenting a promising surrogate model for the current work.

2.7 Frequentist vs. Bayesian Inference

Two fundamentally different paradigms can be considered to estimate the hyperparameters of the Gaussian process model: namely through the frequentist or Bayesian perspective. Atiyat [86] provides a comprehensive discussion of each paradigm as it applies to Gaussian processes. The following is largely based on Atiyat's original work and can be considered a brief summary supplemented where required. Further discussion can be found in Ref. [86].

The frequentist perspective considers the parameters to be fixed yet unknown values [86], [87]. Once data has been observed, the parameters are then estimated as those that maximize the probability of observing the data – a process known as maximum likelihood estimation [86], [87]. Diametrically, the Bayesian perspective considers the parameters to be random variables themselves over which there is some prior belief of their distribution [27], [31], [86], [87], [88]. Bayes rule of conditional probabilities is then used to update the prior belief of the parameters based on the information provided by the observed data to form the posterior distribution [86], [87], [88], [89].

In their graduate thesis, Atiyat [86] compared frequentist and Bayesian approaches for Gaussian process modelling, specifically considering geostatistical data. Their results indicate that either method can be suitable for hyperparameter estimation. Similarly, both methods have been applied successfully in metal-based AM with the Bayesian perspective being adopted in works such as in Refs. [27], [31] and the frequentist perspective adopted in works such as in Refs. [7], [16], [23], [80], [90]. Nevertheless, certain advantages to each of these methods may lend themselves to specific applications. Most generally, the Bayesian framework has been suggested to be more intuitive – particularly by using credible intervals in place of the frequentist's confidence interval [86]. More specifically, of particular importance in the current study, is that the Bayesian framework is able to capture the uncertainty in the hyperparameters themselves [86], [88]. The hyperparameter uncertainty is then captured in the posterior predictive distributions, leading to a more comprehensive representation of the true uncertainty - especially for small data sets, which is a recurrent issue in metal-based AM [86], [88], [90], [91]. Furthermore, if additional data becomes available, Bayesian inference lends itself toward incrementally increasing the amount of data as the current posterior simply becomes the next prior distribution if the observations are independent [88].

Considering the Bayesian inference of a regression model, an illustrative example of the effect of additional data on the posterior distribution was provided in the work of Tipping and is shown in **Figure 6** [88]. Their work suggests that upon observing an initial subset of the available data, the posterior distribution of the parameters is refined; however, it remains relatively diffuse, leading to large predictive variability away from the observed data [88]. They note that observing additional data refines the posterior distribution, leading to reduced uncertainty in the model parameters themselves and, by extension, in the model predictions [88]. Thus, it is argued herein that the Bayesian estimation of the model hyperparameters is suitable for the current study due to its ability to more accurately capture the uncertainty in the model, and its ability to monitor the evolution of the hyperparameters as additional data becomes available.

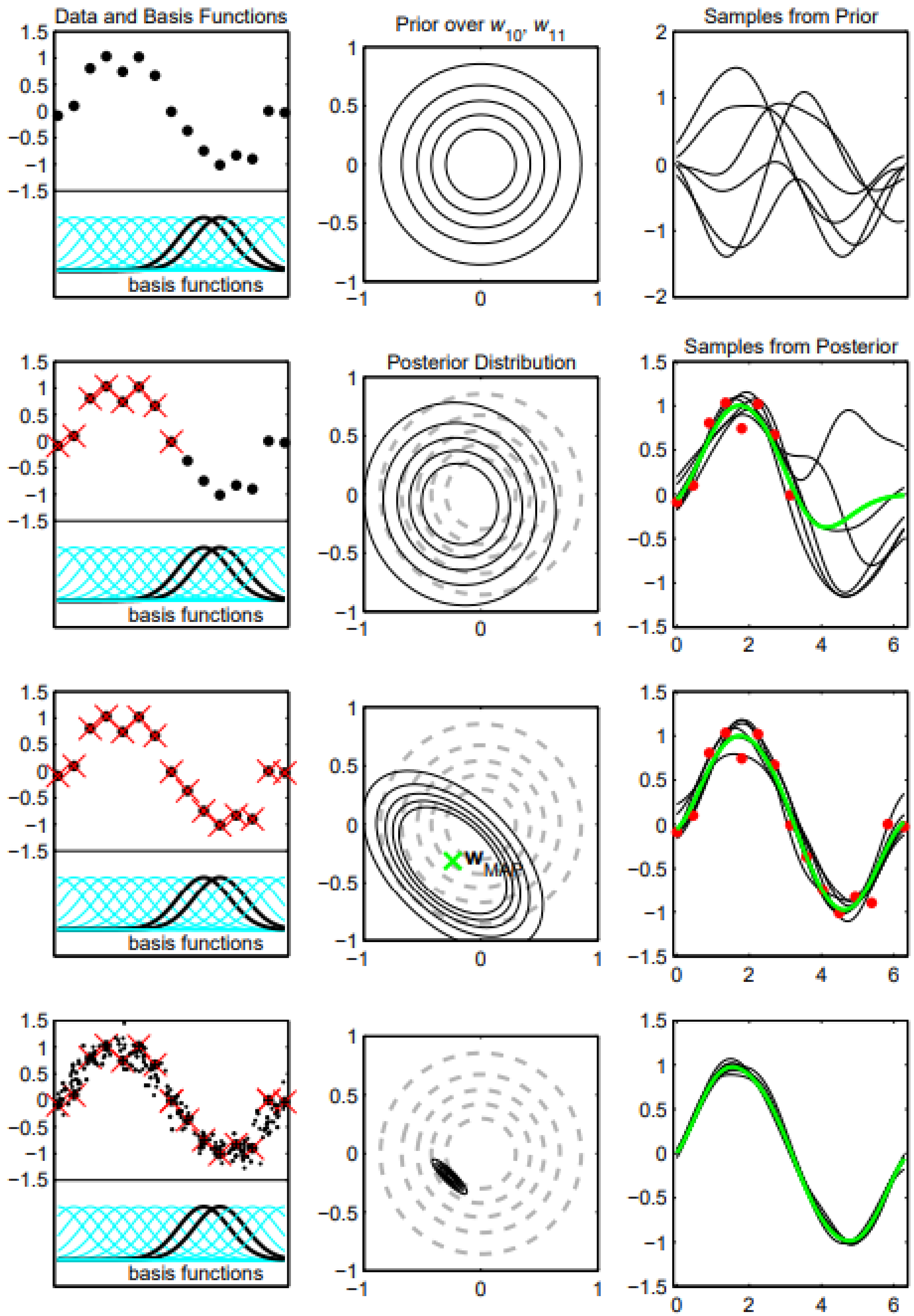

Figure 6. Effect of additional data on the posterior distribution [88].

Despite its advantages, Bayesian inference comes with its own set of limitations. Most notably for this work, these limitations include the need to explicitly define our prior beliefs and the need to compute the posterior distribution. Incorporating subjective prior beliefs has been criticized for introducing, as the name implies, subjectivity into the scientific method [86]. Conversely, it has been suggested that explicitly defining our assumptions in the form of a prior belief may be beneficial, for example by promoting transparency of our prior expectations [88]. Without strong prior beliefs, this limitation can be circumvented by defining noninformative priors [27], [87]; however, Atiyat [86] points out that even noninformative priors still impose some level of prior belief over the process.

The limitation imposed by the need to determine the posterior distribution is largely determined by the choice of the prior distribution and the model parameter set's dimensionality [87]. On one hand, if the prior is carefully selected using conjugate priors, the posterior distribution is of the same family as the prior and can be analytically calculated [87]. On the other hand, if the dimensionality is high or non-conjugate priors are used, there may not be a closed-form solution of the posterior distribution [87]. Even without an analytically tractable posterior, it can still be sampled using Markov Chain Monte Carlo (MCMC) methods [86], [87], [89].

2.8 Active Learning

A common belief in data-driven modelling is that additional data will result in a more accurate model [92], [93]. A limitation of applying data-driven modelling to metal-based AM is that obtaining a sufficiently large data set to develop a reasonably sophisticated model is often prohibitively time-consuming and expensive [25], [91]. To circumvent the above limitation, recent research has explored utilizing data available within literature for common material systems to rapidly develop accurate data-driven models as in Refs. [7], [16], [76], [80], [94], using adaptive sampling optimization algorithms as in Ref. [52], or both as in Ref. [95]. Nevertheless, it can be said these methods rely on large amounts of published work which does not apply to m-LPBF in its current state, or samples in regions near the expected optimum while failing to adequately capture the entire design space. In the latter case, this may limit the generalizability of the model in regions outside of the expected optimum if the model is adopted in future multi-objective optimization tasks involving a different set of objectives. As a result, researchers are beginning to recognize active learning as a potential solution [25], [91].

Active learning is built on the notion that data-driven models can be developed more efficiently if the model selects data from which it believes it can learn the most in an iterative manner [72], [93], [96]. This idea has been suggested to various degrees as a possible method to improve data-driven models in LPBF process modelling as in Refs. [16], [85], [90] and was even alluded to previously in the general surrogate modelling framework; however, limited research including Refs. [25], [28], [97], [98] has gone beyond a theoretical idea to a practical implementation. In fact, even the seminal work of Tapia et al. [31], from which this work builds upon, and in the author's opinion is in large part an extension of, describes sequential sampling based on predictive uncertainty and space filling. Nevertheless, their work fails to explicitly define and test a framework that easily extends to higher dimensional problems, and despite its significance to the field of LPBF process modelling, fails to comprehensively investigate the suitability and effectiveness of active learning in their Bayesian inference Gaussian process regression framework. Although the theoretical arguments and limited practical implementation presented in the works above are promising, alone they are insufficient to suggest active learning is beneficial in modelling the process. Attenberg and Provost point out that a distinct disjoint exists between theoretical active learning and its practical implementation, including determining a suitable hypothesis class, learning strategy, and cold starting [29]. Therefore, there exists a need to extend beyond the suggestion that active learning may be beneficial in data-driven model development in LPBF to determine its practical suitability.

As one of the types of active learning, pool-based active learning assumes there exists a large set of unlabeled instances readily available [93], [98]. The active learning problem then becomes determining which data should be labeled from the unlabeled pool based on a limited budget to yield the best model [72], [92], [99]. This framework naturally lends itself to the metal-based AM process in which all instances within some finite design space can often be enumerated; however, printing and the labeling of these instances is expensive.

Within pool-based active learning, samples can either be drawn sequentially or in batches. Sequential sampling maximizes the information provided from each sample by updating the model after each sample is labeled [92], [96], and smaller batches were observed to be more efficient in metal-based AM in the work of Ref. [98]. The author would argue that sequentially sampling lends itself to simulation studies utilizing a single annotator (in the case of a single computer for example); however, sequential sampling does not consider the efficient allocation of labeling resources [92], [98]. In the case of LPBF, experimental studies utilizing active learning arguably lend themselves to batch sampling – for example, an interesting study of batch experimentation for process optimization was implemented by Ref. [95] in which multiple samples are queried at once. Although reducing the efficiency of the sampling process as described above, even with a single annotator, in the current work batch mode sampling allows each iteration to be printed on a single substrate, thus reducing the cost and time required. Although not the driving motivation in this work, researchers such as Cai et al. [92] and Van Houtum and Vlasea [98] further advocate for the use of batch mode active learning in the case that multiple annotators are available.

Attenberg and Provost [29] suggest that one of the disjoints between theoretical active learning and its practical application is the selection of a suitable sampling strategy. Settles [93] summarizes various sampling strategies in their highly influential review among which they suggest uncertainty-based sampling is arguably the most popular. Nevertheless, the majority of active learning literature has focused on sequential sampling of classification problems leaving the current case of batch sampling regression relatively unexplored [72], [92], [96], [99].

Within LPBF, Mojumder et al. [97] developed a Gaussian process regression model through active learning using simulation results to relate key processing parameters (laser power, scan speed, hatch spacing, layer thickness) to lack-of-fusion porosity. An uncertainty-based sampling procedure was adopted in their work, which labels the top k most uncertain samples. Despite illustrating promising results, Cai et al. [92] criticize extending sequential sampling strategies in such a way, suggesting they fail to account for correlation among queried samples. Alternatively, the work Cai et al. [92] suggested that it is reasonable to expect that by selecting samples that cause the maximal change to the model parameters, the rate of convergence to the true model can be enhanced. Based on this premise Cai et al. [92] developed a batch active learning algorithm for linear regression by approximating sequential sampling and taking into consideration the correlation within a batch of samples. In their work, they suggest a possible extension for Gaussian process regression; however, their sampling strategy was later criticized by Zhao et al. [96] for being computationally expensive. Instead, Zhao et al. [96] introduced two maximum model change batch mode active learning algorithms specifically for Gaussian process regression by considering weight space information gain – one based on enumeration and the other on greedy sampling. Greedy sampling empirically demonstrated superior performance in terms of computational costs with negligible difference in accuracy compared to enumeration while also outperforming various alternative algorithms, including the algorithm proposed by Cai et al. [92], in terms of stability and convergence. The sampling strategy developed by Zhao et al. [96], and found in **Section 3.4**, presents a promising avenue for efficient data-driven model development in metal-based AM.

2.9 Process-Property Optimization

It has been established in **Section 2.2.1** that the properties of LPBF-produced components are highly dependent on the key processing parameters: laser power, exposure time, point distance, hatch spacing, and layer thickness when considering m-LPBF. Given the ability to model the LPBF process, a natural extension has considered optimizing the processing parameters to achieve suitable mechanical properties for a given application [75]. A fundamental review of recent efforts related to AM process optimization, particularly leveraging machine learning and surrogate models, can be found in the work of Zhai and Chen [75]. The general form of an optimization problem can be expressed as **Eq 6**, where $f_m(\boldsymbol{x})$ is the m^{th} objective function of design vector $\boldsymbol{x}$, $g_j(\boldsymbol{x})$ is the j^{th} inequality constraint, $h_i(\boldsymbol{x})$ is the i^{th} equality constraint, and each design variable x_k is bounded between a lower bound, ${x_k}^L$, and an upper bound, ${x_k}^U$ [100].

$$\min_{\boldsymbol{x}} f_m(\boldsymbol{x}), m = 1 \dots M$$
$$s.t. \begin{cases} h_i(\boldsymbol{x}) = 0, & i = 1 \dots I \\ g_j(\boldsymbol{x}) \leq 0, & j = 1 \dots J \\ {x_k}^L \leq x_k \leq {x_k}^U, & k = 1 \dots q \end{cases} \qquad \textbf{Eq 6}$$

A wealth of literature has been devoted to the special case in which there is only a single objective, and as a result a mature body of literature, both in theory and application, has been established. Traditionally, the LPBF community has adopted this single-objective framework to minimize defects or maximize a specific property, using various techniques, including most notably Taguchi's methods [19], traditional response surface methodology [8], process type maps or windows [20], [83], population-based algorithms [66], [101], and Bayesian optimization [52]. Despite forming the basis for today's practices, these methods fail to account for the competing objectives faced by industry. In particular, the industry must produce high-quality components meeting application standards while minimizing costs and abiding by environmental regulations - objectives that are intuitively conflicting. As such, there has been a paradigm shift from considering the metal-AM process as a single-objective to a multi-objective optimization problem.

The concept of optimality in multi-objective optimization becomes more ambiguous than its single-objective counterpart. Under multi-objective optimization, a design vector is said to be optimal if it is Pareto optimal [71], [102]. Pareto optimality is defined as a design vector, $\boldsymbol{x}^*$, with corresponding objectives, $\boldsymbol{f}^* = \boldsymbol{f}(\boldsymbol{x}^*)$, such that there is no other feasible design, $\boldsymbol{x}$, with corresponding objective vector, $\boldsymbol{f} = \boldsymbol{f}(\boldsymbol{x})$, for which $\boldsymbol{f} \leq \boldsymbol{f}^*$ with at least one objective $f_m < f_m^*$ [71], [102], [103]. The set of all Pareto optimal points forms the Pareto optimal set and defines the equally optimal solutions of a multi-objective optimization problem [70], [102], [104]**.** The Pareto set can be graphically depicted in the objective space, illustrated in **Figure 7**, known as the Pareto front [71].

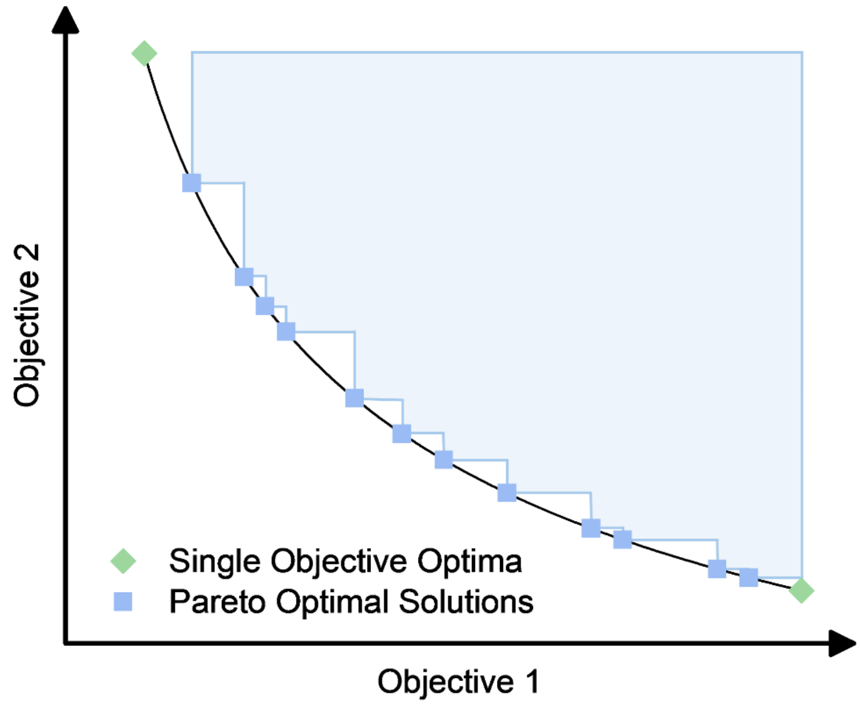

Figure 7. An illustrative example of a Pareto front in the objective space.

It is argued herein that from a theoretical perspective, given the ability to determine the Pareto front, it is of no detriment to extend the single-objective optimization problem from considering solely relative density to considering both relative density and processing rate. Given each objective has a unique minimum, in the bi-objective problem the single-objective optimal solutions are determined as the vertices of the Pareto front [103]. Thus, even in the extreme case where relative density must be maximized at all costs in the as-printed state, the optimal solution can still be determined by solving the multi-objective optimization problem.

Various methods have been proposed to determine Pareto optimal solutions, which can be categorized as either scalarization or vector methods [103]. Scalarization methods reduce multiple objectives into a single objective to leverage well-established single-objective optimization techniques [103]. Among these methods, the weighted sum and desirability function approaches aggregate the objectives based on their relative importance and have been adopted in metal-based AM, including the works of Refs. [77], [105], [106], [107], [108]. Specifically considering scalarization techniques applied to m-LPBF Ti64, Aboutaleb et al. [61] maximized relative density and elongation of m-LPBF Ti64 using their novel multi-objective accelerated process optimization algorithm, while Kuo et al. [81] used a weighting scheme to maximize relative density and dimensional accuracy. Despite their widespread adoption, scalarization methods have been criticized for the need to select objective preference *a priori,* their inability to solve for a Pareto set of solutions single run, and failing to determine a distributed Pareto front [70], [102], [103].

In contrast, vector methods consider each objective function independently to determine either a single or a set of Pareto optimal solutions [103]. One such method that has been applied in metal-based AM, as in the Refs. [76], [108], is to consider a single most important objective while treating the remaining objectives as inequality constraints. Nevertheless, if not judicious with the selection of constraint bounds the problem may be infeasible, and if feasible, only determines a single solution [76], [103], [108]. As an alternative, particular attention has been devoted to multi-objective evolutionary algorithms due to their population-based approaches, which allow the algorithms to determine a set of non-dominated solutions in a single iteration [102], [104]. Most notable of which is the non-dominated sorting genetic algorithm – II (NSGA-II) [70] originally proposed by Deb et al. [104] to address the limitation of their previously proposed non-dominated sorting genetic algorithm [102]. By cleverly extending the traditional genetic operators to the multi-objective problem, their algorithm has become highly influential in the field of multi-objective optimization with nearly 40,000 citations based on Scopus as of the time of writing, and has found applications in a wide range of fields including metal-based AM [75], [85], [109], [110].

Both Criales et al. [111] and Lu and Shi [67] formulated a multi-objective optimization problem considering the relative density, time, and energy of the LPBF process [67], [111]. Each of their works establishes a precedent for effectively determining a Pareto front to understand the tradeoff between time and quality in the LPBF process using NSGA-II. Furthermore, despite varying the analytical model used to describe build time and energy, both works illustrate that time and energy are positively correlated. Nevertheless, each of these works considers c-LPBF and models relative density using MLR, which has been shown as described above to inadequately capture the complexities of metal-based AM.

In summary, it is suggested that it is beneficial to consider the Pareto front in its entirety instead of defining a preference *a priori* to discover all possible tradeoffs among conflicting objectives. Furthermore, it is of little benefit to consider the Pareto front, or any optimization for that matter, if the surrogate model insufficiently captures the complexities of the metal AM process. Thus, it is currently the combination of a sufficient surrogate model, suggested to be Bayesian inference of Gaussian process regression, and a vector optimization scheme, most notably NSGA-II, that presents the most promise to determine the tradeoff of time and quality in m-LPBF manufactured Ti64 components.

2.10 Summary of Literature Review

LPBF offers the ability to produce high-quality near-net-shape components, albeit at lower processing rates than other metal-based AM techniques. Despite inconclusive evidence, c-LPBF has dominated both commercial machines and academic efforts, while its counterpart, m-LPBF, remains relatively unexplored. Nevertheless, recent works have suggested that under certain circumstances, it may be acceptable to induce some finite amount of defects into as-built components, most notably porosity, in exchange for higher processing rates. Incorporating processing rate as an objective and solving a multi-objective problem theoretically presents no hindrance to the strictest industries requiring the highest quality as-built components, while presenting alternative processing combinations for less stringent industries that may benefit from increased productivity. Although simple analytical approximations exist for processing rate, relative density is complex to model analytically and requires surrogate approximations. Surrogate model development for metal-based AM is often hindered by small data sets. Gaussian process regression has demonstrated superior ability with small data sets while providing uncertainty estimates. These estimates can be used within active learning to efficiently sample the design space and develop accurate models with limited data. All the while, the Bayesian framework provides a method of incorporating the uncertainty of the hyperparameters themselves and evaluating the progression of active learning. In conjunction, Bayesian inference of a Gaussian process regression model paired with active learning presents a promising framework for surrogate model development which can be used in model-based multi-objective optimization algorithms to balance both time and quality in m-LPBF. To the author's knowledge, no such study has been undertaken integrating all three techniques in metal-based AM. This work addresses this gap with the objective of further promoting the use of metal-based AM in various industries and the exploration of m-LPBF.

3. Methodology

3.1 Materials, Manufacturing, and Experimental Measurement

In this study, Ti64 powder with a nominal chemical composition range shown in **Table 1** was supplied by AP&C (Boisbriand, QC). Cylindrical samples (Ø 10 x 15 mm) were printed by TronosJet Manufacturing (Charlottetown, PEI) using a Renishaw AM250 m-LPBF machine. It is worth noting that the current study used reused powder particles to best represent the powder conditions used in commercial printing applications. Samples were spatially randomized and printed with independent control of laser power, exposure time, point distance, and hatch spacing. It has been suggested in the literature that layer thickness dictates surface finish and is often based on the printed component's application requirements [10], [20], while Costa et al. [66] note that layer thickness is often fixed for LPBF studies. In the current study, fixing layer thickness allowed all samples of a given active learning iteration to be printed within the same batch, minimizing both the time and cost of the iterative process. For these reasons, a fixed layer thickness of 30 μm was used in the current study.

Table 1. Nominal chemical composition of Ti64 powder [112].

Element	**Ti**	**O**	**Al**	**V**	**Fe**	**C**	**N**	**H**	**Y**
Max (Wt. %)	Balance	0.20	6.75	4.50	0.30	0.08	0.05	0.015	0.005
Min (Wt. %)	Balance	-	5.50	3.50	-	-	-	-	-

From their as-printed state, the samples were first ultrasonically cleaned in ethyl alcohol (95% volume) at a nominal temperature of 35 ºC for 5 minutes to remove any unfused powder and potential contaminants from the surface of the sample. The relative density, RD, was then determined according to Archimedes principle, **Eq 7** [113] **– Eq 8**, by comparing the mass of the samples in air, m_a, with the mass of the samples in a fluid of known density, m_w. In the current study, this fluid was taken to be distilled water with temperature-dependent density [113], ρ_w, while the density of air is denoted by ρ_a. The theoretical density of Ti64, ρ_{th}, was considered to be 4.43 g/cm$^{3.}$ This represents the mid-range of the theoretical density reported in literature for Ti64 as summarized by Ref. [16]. Three measurements of mass in both air and distilled water were taken for each sample using a high-precision digital scale (FX-300i, A&D Company Limited). To minimize the influence of the temperature-dependent properties of distilled water on the measured relative density, variation in the temperature of the distilled water was measured using a K-type thermocouple, and its density was accounted for in 5 sample increments. All samples were cleaned and measured in a temporally randomized order.

$$\rho = \frac{m_a}{m_a - m_w}(\rho_w - \rho_a) + \rho_a \qquad \textbf{Eq 7}$$

$$RD = \frac{\rho}{\rho_{th}} \qquad \textbf{Eq 8}$$

To impose the natural bounds of the LPBF process, the observed relative density, which is bound on the unit interval, was transformed to the unbounded real number line using the Logit transformation shown in **Eq 9**, as was discussed in the work of Costa et al. [66], where y and y' are the observed and transformed responses, respectively. In its absence, model violations and physically impermissible predictions can occur Costa et al. [66]. In particular, the normality of residuals, a common modelling assumption, can easily become violated when modelling a bound response [66], [114]. Furthermore, Maitra et al. [16] illustrated that the observed relative density in literature is heavily skewed towards higher relative densities, while La Fe-Perdomo et al. [22] suggest that data transformation may be required to normalize the response and mitigate the asymmetrical nature of the LPBF process. The Logit transformation compresses observations near the center of the interval and expands observations near the extremes. Thus, it was hypothesized that the Logit data transformation may be suitable for achieving a more symmetric distribution. In this work, all modelling efforts were performed in the Logit space, and by extension, any modelling assumptions and evaluations were made in this space as well.

$$y' = \ln \frac{y}{1 - y} \qquad \textbf{Eq 9}$$

3.2 Design of Experiments: Central Composite Design

The initial print consisted of a central composite design (CCD) – a 3-factor illustrative example of which is shown in **Figure 8** [73]. Traditionally used with 2^{nd}-order response surfaces, the design is composed of n_f factorial points, n_α axial points a distance α from the center of the design, and n_c center points which combined allow the estimation of linear, interaction, and quadratic effects as well as pure error in a traditional MLR model [73], [75], [101], [108]. In traditional MLR development, the properties of the design, among which rotatability and optimality are often considered, are largely influenced by α and n_c [73]. In the current work, a Gaussian process regression model was developed and α and n_c were used for alternative objectives. Axial distance was defined as 2 which allowed the design space to be described by a 4-dimensional sphere in coded units. Despite commonly being used with MLR, this choice presented two principal benefits to the current study: it avoided the vertices of the circumscribed hypercube, which present highly undesirable parameter combinations, and simplified the design space to a single inequality constraint.

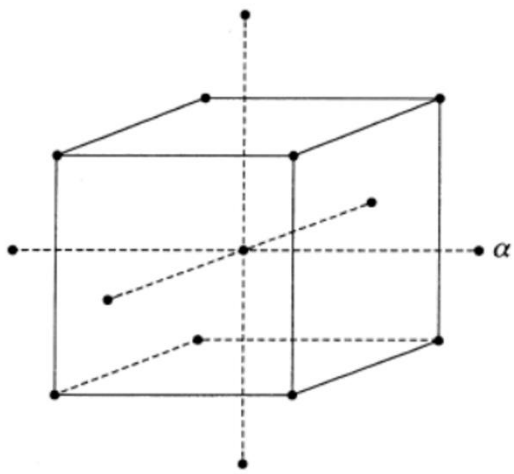

Figure 8. Illustrative 3-factor central composite design [73].

In the current active learning framework, all samples for a given iteration were printed within the same batch for consistency and cost considerations. In an effort to ensure between-batch consistency, the center points served as repeated measurements to determine if there was a statistically significant effect of batch on the relative density of the samples. Statistical significance was determined using a fixed effect one-way Analysis of Variance performed in Minitab 21.1, the null and alternative hypothesis of which is illustrated in **Eq 10** [115]. It is worth noting that this is considered a simplification of the consistency of the LPBF process as it only considers a single region of the design space, assuming consistency in the center of the design space is indicative of consistency throughout the design space, and considers each batch a fixed effect instead of utilizing a more realistic random effect model.

$$y_{ij} = \mu + \tau_i + \varepsilon_{ij} \begin{cases} i = 1,2,3 \\ j = 1, \dots, n_c \end{cases}$$
$$H_o: all\ \tau_i = 0 \qquad \textbf{Eq 10}$$
$$H_a: at\ least\ one\ \tau_i \neq 0$$

The physical parameters associated with the coded levels of the CCD design were determined based on the supplier's suggested parameters, as depicted in **Table 2**, for a layer thickness of 30 µm. The supplier's suggested processing parameters served as the center of the design space apart from laser power, whose supplier suggested value served as its upper limit. This was due to the maximum output power of 200 W associated with the LPBF machine used. The axial points of the other parameters were chosen such that the design space represented the author's best prior notion of a feasible design space while ensuring the coded levels represent integer values in the physical domain.

Table 2. Coded levels of the design space.

Level	**Laser Power (W)**	**Exposure Time (µs)**	**Point Distance (µm)**	**Hatch Spacing (µm)**
Supplier	200	50	75	50
-2	120	10	35	10
-1	140	30	55	30
0	160	50	75	50
1	180	70	95	70
2	200	90	115	90

In addition to the initial CCD design, the first print consisted of 6 validation samples. These samples were created by sequentially generating random feature vectors which satisfy the condition that the points lie within or near a 4-dimensional sphere of radius 2 centered at the origin, and mimic the space-filling properties of a Latin hypercube. That is, the feature vector was randomly generated such that the kth design variable of the feature vector is unique to the kth design variable of previously generated validation feature vectors. This was done to encourage diverse sampling within the design space. Thereafter, each subsequent print of active learning samples included 6 test samples with parameters selected randomly from the set of unlabeled data. After the last active learning iteration, the test samples from the previous iterations were amalgamated to form the final testing set and used to evaluate the developed model.

3.3 Gaussian Process Regression

Gaussian process regression assumes all observations are drawn from a Gaussian process uniquely defined by its' mean, $m(\cdot)$, and covariance or kernel, $k(\cdot,\cdot)$, functions. As a result, any finite collection of observations follows a joint multivariate Gaussian distribution [7], [80]. Given a collection of n observed q-dimensional feature vectors represented by a matrix, $\boldsymbol{X}$ $(n \times q)$, with known labels, $\boldsymbol{y}$ $(n \times 1)$, and a collection of m unobserved q-dimensional feature vectors represented by a matrix, $\boldsymbol{X}_*$ $(m \times q)$, with unknown labels, $\boldsymbol{y}_*$ $(m \times 1)$, their joint distribution can be expressed as **Eq 11**, where σ_f^2 and σ_n^2 are the signal and noise variance, respectively, and $\boldsymbol{I}$ is the identity matrix[27], [84]. Since in this work experimental observations with inherent noise were modelled, the Gaussian process regression model assumes there is independent and identically distributed normal noise accounted for by the additive $\sigma_n^2\boldsymbol{I}_{n+m}$ term [27].

$$\begin{bmatrix} \boldsymbol{y} \\ \boldsymbol{y}_* \end{bmatrix} \sim MVN\left(\begin{bmatrix} \boldsymbol{m}(\boldsymbol{X}) \\ \boldsymbol{m}(\boldsymbol{X}_*) \end{bmatrix}, \sigma_f^2 \begin{bmatrix} \boldsymbol{K}(\boldsymbol{X},\boldsymbol{X}) & \boldsymbol{K}(\boldsymbol{X},\boldsymbol{X}_*) \\ \boldsymbol{K}(\boldsymbol{X},\boldsymbol{X}_*)^T & \boldsymbol{K}(\boldsymbol{X}_*,\boldsymbol{X}_*) \end{bmatrix} + \sigma_n^2\boldsymbol{I}_{n+m}\right) \qquad \textbf{Eq 11}$$

The properties of the Gaussian process model are defined by its mean and kernel functions [18], [27]. In this work, two classes of popular anisotropic kernel functions were used: the squared exponential kernel, **Eq 12**, and the Matérn class of kernel, **Eq 13**.

$$K_{SE}(Q) = \exp\left(-\frac{1}{2}Q^2\right) \qquad \textbf{Eq 12}$$

$$K_{Ma}(Q) = \frac{2^{1-\nu}}{\Gamma(\nu)}\left(\sqrt{2\nu}Q\right)^{\nu}\kappa_{\nu}\left(\sqrt{2\nu}Q\right) \qquad \textbf{Eq 13}$$

To circumvent the computational burden of the general Matérn kernel, which requires the evaluation of the modified Bessel function, $\kappa_\nu(\cdot)$, where ν dictates the smoothness, two specific cases were considered in this work, $\nu = 3/2$, **Eq 14**, and $\nu = 5/2$, **Eq 15**. In these cases, the kernel function simplifies to the product of a polynomial and exponential function [84]. In all cases, the kernel is a function of the Q, **Eq 16**, as defined similarly in Tapia et al. [31], and can be considered the Euclidean distance between two q-dimensional vectors $\boldsymbol{x}$ and $\boldsymbol{x}'$ with the difference in each dimension scaled by its own characteristic length scale ℓ_i. That is the characteristic length scale of laser power, exposure time, point distance, and hatch spacing are denoted by ℓ_1, ℓ_2, ℓ_3, and ℓ_4, respectively. This unique characteristic length scale for each dimension gives the kernel its anisotropic property and was used to determine feature significance as discussed in **Section 4.5**.

$$K_{Ma_{3/2}}(Q) = \left(1+\sqrt{3}Q\right)\exp\left(-\sqrt{3}Q\right) \qquad \textbf{Eq 14}$$

$$K_{Ma_{5/2}}(Q) = \left(1+\sqrt{5}Q+\frac{5}{3}Q^2\right)\exp\left(-\sqrt{5}Q\right) \qquad \textbf{Eq 15}$$

$$Q(\boldsymbol{x},\boldsymbol{x}') = \sqrt{(\boldsymbol{x}-\boldsymbol{x}')diag(\boldsymbol{\ell}^{-2})(\boldsymbol{x}-\boldsymbol{x}')^T} \qquad \textbf{Eq 16}$$

Similar to the work of, for example, Maitra et al. [16], this work considered the use of various mean functions. Specifically, 3 mean functions were considered: constant, linear, and quadratic. Each of the mean functions can be expressed as $m(\boldsymbol{x}) = \boldsymbol{\phi}(\boldsymbol{x})\boldsymbol{\beta}$, where $\boldsymbol{\phi}(\boldsymbol{x})$ is an $(1 \times p)$ function of the feature vector $\boldsymbol{x}$, and $\boldsymbol{\beta}$ is a $(p \times 1)$ vector of mean function coefficients. Considering a q-dimensional feature vector, the constant, linear, and quadratic mean functions can be described by the functions, **Eq 17**, **Eq 18**, and **Eq 19**, respectively. Defining a combined $(n \times p)$ matrix $\boldsymbol{\Phi}(\boldsymbol{X})$ with its i^{th} row defined by $\boldsymbol{\phi}(\boldsymbol{x}_i)$, the $(n \times 1)$ mean vector evaluated at $\boldsymbol{X}$ can be calculated using $\boldsymbol{m}(\boldsymbol{X}) = \boldsymbol{\Phi}(\boldsymbol{X})\boldsymbol{\beta}$.

$$\boldsymbol{\phi}(\boldsymbol{x}) = [1] \qquad \textbf{Eq 17}$$

$$\boldsymbol{\phi}(\boldsymbol{x}) = [1 \quad x_1 \quad \cdots \quad x_q] \qquad \textbf{Eq 18}$$

$$\boldsymbol{\phi}(\boldsymbol{x}) = \begin{bmatrix}1 & x_1 & \cdots & x_q & x_1x_2 & \cdots & x_{q-1}x_q & x_1^2 & \cdots & x_q^2\end{bmatrix} \qquad \textbf{Eq 19}$$

Based on the above definition of mean and kernel functions, the Gaussian process model can be defined in terms of a set of hyperparameters, $\boldsymbol{\theta}$, given by $\{\sigma_f^2, \sigma_n^2, \boldsymbol{\beta}, \boldsymbol{\ell}\}$. From the marginalization property of multivariate Gaussian distributions [84], the labeled data are distributed as $\boldsymbol{y}|\boldsymbol{\theta} \sim MVN\left(\boldsymbol{m}(\boldsymbol{X}), \sigma_f^2\boldsymbol{K}(\boldsymbol{X},\boldsymbol{X}) + \sigma_n^2\boldsymbol{I}_n\right)$. Considering the Bayesian framework, up to proportionality the posterior distribution of the hyperparameters given the observations, $p(\boldsymbol{\theta}|\boldsymbol{y})$, is expressed as **Eq 20** [31], where $p(\boldsymbol{y}|\boldsymbol{\theta})$ is the likelihood of the observed data given the hyperparameters, and $p(\boldsymbol{\theta})$ is the prior belief of the hyperparameters.

$$p(\boldsymbol{\theta}|\boldsymbol{y})\ \alpha\ p(\boldsymbol{y}|\boldsymbol{\theta})\ p(\boldsymbol{\theta}) \qquad \textbf{Eq 20}$$

Hyperparameters were considered independent a priori, and their joint prior probability was calculated as the product of their independent prior distributions, **Eq 21 – Eq 24** [31]. In this work, similar prior distributions were used to the original work of Tapia et al. [31], all of which are of the same family of distribution. All priors used offer little information; however, they are not considered uninformative [86]. The inverse gamma distribution over σ_f^2 and σ_n^2 assigns infinite variance with means at 1 and 0.1, respectively [31], [86]. The multivariate Gaussian distribution over mean parameters indicates a prior belief that no mean function parameters should be included with a high uncertainty [31], while the uniform distribution defines an allowable range from which the characteristic length scale can take on values with equal probability, and by extension, limits the possible shapes of the kernel functions. All priors used imparted some amount of belief, although in the current work, they are all highly uncertain.

$$p\left(\sigma_f^2\right)\ \sim Inverse\ Gamma\ (2,1) \qquad \textbf{Eq 21}$$

$$p(\sigma_n^2)\ \sim Inverse\ Gamma\ (2,0.1) \qquad \textbf{Eq 22}$$

$$p(\boldsymbol{\beta}) \sim Multivariate\ Normal\ \left(\mathbf{0}, 10^4\boldsymbol{I}_p\right) \qquad \textbf{Eq 23}$$

$$p(\ell_i) \sim Uniform(0,4) \qquad \textbf{Eq 24}$$

The benefit of the conjugate multivariate Gaussian prior is that a closed-form posterior can be found as **Eq 25 – Eq 27**, where $\boldsymbol{\mu}_0$ and $\boldsymbol{\Sigma}_0$ are the prior mean and covariance, respectively [31].

$$p(\boldsymbol{\beta}|\boldsymbol{y}, \sigma_f^2, \sigma_n^2, \boldsymbol{\ell}) \sim MVN(\boldsymbol{\mu}_{\boldsymbol{\beta}|\cdot}, \boldsymbol{\Sigma}_{\boldsymbol{\beta}|\cdot}) \quad \textbf{Eq 25}$$

$$\boldsymbol{\Sigma}_{\boldsymbol{\beta}|\cdot} = \left(\boldsymbol{\Sigma}_0^{-1} + \boldsymbol{\Phi}^T\left(\sigma_f^2\boldsymbol{K}(\boldsymbol{X},\boldsymbol{X}) + \sigma_n^2\boldsymbol{I}_n\right)^{-1}\boldsymbol{\Phi}\right)^{-1} \quad \textbf{Eq 26}$$

$$\boldsymbol{\mu}_{\boldsymbol{\beta}|\cdot} = \boldsymbol{\Sigma}_{\boldsymbol{\beta}|\cdot}\left(\boldsymbol{\Sigma}_0^{-1}\boldsymbol{\mu}_0 + \boldsymbol{\Phi}^T\left(\sigma_f^2\boldsymbol{K}(\boldsymbol{X},\boldsymbol{X}) + \sigma_n^2\boldsymbol{I}_n\right)^{-1}\boldsymbol{y}\right) \quad \textbf{Eq 27}$$

With a complete closed-form solution of the conditional posterior distribution, MCMC sampling was performed using Gibbs sampling for mean function parameters, $\boldsymbol{\beta}$, while using Metropolis sampling with a Gaussian proposal distribution for the remaining hyperparameters. The complete sampling algorithm, adopted and modified from the previous work of Tapia (the overarching dissertation including the work in Refs. [27], [31]), is shown in **Algorithm 1** [18]. An initial burn-in period of 5000 iterations inclusive of the initial hyperparameter estimate was used to allow the Markov chain to reach its stationary distribution, while 50000 samples were collected thereafter from the posterior distribution to overcome correlation amongst samples and make meaningful inferences about the hyperparameters and the response at unobserved feature vectors.

Algorithm 1. MCMC sampling of hyperparameters. Modified from Ref. [18].

Input: Number of samples N, burn-in period B, initial sampling parameters $\boldsymbol{\theta}^{(0)} \leftarrow \left\{\boldsymbol{\beta}^{(0)}, \sigma_f^{2\,(0)}, \sigma_n^{2\,(0)}, \ell_1^{(0)}, \ell_2^{(0)}, \ell_3^{(0)}, \ell_4^{(0)}\right\}$, proposal distribution standard deviation $\boldsymbol{\sigma}_{\boldsymbol{\theta}^*} \leftarrow \left\{\sigma_{\sigma_f^{2*}}, \sigma_{\sigma_n^{2*}}, \sigma_{\ell_1^*}, \sigma_{\ell_2^*}, \sigma_{\ell_3^*}, \sigma_{\ell_4^*}\right\}$

Output: MCMC samples $\boldsymbol{\Theta}$ $(\mathrm{N} \times \mathrm{q})$

for i **in range**$(1, \mathrm{N}+\mathrm{B})$:

  $\boldsymbol{\beta}^{(\mathrm{i})} \sim \mathrm{p}\left(\boldsymbol{\beta} | \sigma_f^{2\,(\mathrm{i}-1)}, \sigma_n^{2\,(\mathrm{i}-1)}, \ell_1^{(\mathrm{i}-1)}, \ell_2^{(\mathrm{i}-1)}, \ell_3^{(\mathrm{i}-1)}, \ell_4^{(\mathrm{i}-1)}, \mathbf{y}\right)$

  for all $\theta_j \neq \boldsymbol{\beta}$:

    $\theta_j^* \sim \mathrm{p}\left(\theta_j | \theta_j^{(\mathrm{i}-1)}\right)$

    $$\mathrm{r} = \frac{\mathrm{p}\left(\theta_1^{(i)}, \dots, \theta_{j-1}^{(i)}, \theta_j^*, \theta_{j+1}^{(\mathrm{i}-1)}, \dots, \theta_q^{(\mathrm{i}-1)} | \mathbf{y}\right)}{\mathrm{p}\left(\theta_1^{(i)}, \dots, \theta_{j-1}^{(i)}, \theta_j^{(\mathrm{i}-1)}, \theta_{j+1}^{(\mathrm{i}-1)}, \dots, \theta_q^{(\mathrm{i}-1)} | \mathbf{y}\right)}$$

    $\mathrm{u} \sim \mathrm{Uniform}(0,1)$

    if $\mathrm{u} < \mathrm{r}$:

      $\theta_j^{(\mathrm{i})} \leftarrow \theta_j^*$

    else:

      $\theta_j^{(\mathrm{i})} \leftarrow \theta_j^{(\mathrm{i}-1)}$

  $\boldsymbol{\theta}^{(\mathrm{i})} \leftarrow \left\{\boldsymbol{\beta}^{(\mathrm{i})}, \sigma_f^{2\,(i)}, \sigma_n^{2\,(i)}, \ell_1^{(i)}, \ell_2^{(i)}, \ell_3^{(i)}, \ell_4^{(i)}\right\}$

return $\boldsymbol{\Theta} \leftarrow \left\{\boldsymbol{\theta}^{(\mathrm{B})}, \boldsymbol{\theta}^{(\mathrm{B}+1)}, \dots, \boldsymbol{\theta}^{(\mathrm{N}+\mathrm{B}-1)}, \boldsymbol{\theta}^{(\mathrm{N}+\mathrm{B})}\right\}$

From **Eq 11**, given a sampled set of hyperparameters $\boldsymbol{\theta}^{(\mathrm{i})}$ the conditional distribution of the unobserved response, $\boldsymbol{y}_*$, given the observed response, $\boldsymbol{y}$, was obtained as **Eq 28 – Eq 30** [31]. By sampling from the conditional distribution, **Eq 28,** for each of the posterior hyperparameter samples a Bayesian posterior predictive distribution was obtained.

$$\boldsymbol{y}_* | \boldsymbol{y}, \boldsymbol{\theta} \sim MVN\left(\boldsymbol{\mu}_{\boldsymbol{y}_*|\boldsymbol{y},\boldsymbol{\theta}}, \boldsymbol{\Sigma}_{\boldsymbol{y}_*|\boldsymbol{y},\boldsymbol{\theta}}\right) \quad \textbf{Eq 28}$$

$$\boldsymbol{\mu}_{\boldsymbol{y}_*|\boldsymbol{y},\boldsymbol{\theta}} = \boldsymbol{\Phi}(\boldsymbol{X}_*)\boldsymbol{\beta} + \boldsymbol{K}(\boldsymbol{X}, \boldsymbol{X}_*)^T \left(\sigma_f^2 \boldsymbol{K}(\boldsymbol{X}, \boldsymbol{X}) + \sigma_n^2 \boldsymbol{I}_n\right)^{-1} (\boldsymbol{y} - \boldsymbol{\Phi}(\boldsymbol{X})\boldsymbol{\beta}) \quad \textbf{Eq 29}$$

$$\boldsymbol{\Sigma}_{\boldsymbol{y}_*|\boldsymbol{y},\boldsymbol{\theta}} = \boldsymbol{K}(\boldsymbol{X}_*,\boldsymbol{X}_*) + \sigma_n^2\boldsymbol{I}_m - \boldsymbol{K}(\boldsymbol{X},\boldsymbol{X}_*)^{\boldsymbol{T}}\left(\sigma_f^2\boldsymbol{K}(\boldsymbol{X},\boldsymbol{X}) + \sigma_n^2\boldsymbol{I}_n\right)^{-1}\boldsymbol{K}(\boldsymbol{X},\boldsymbol{X}_*) \quad \textbf{Eq 30}$$

The posterior predictive distribution of relative density was obtained using the inverse Logit transformation for each of the samples from the posterior predictive distribution. For simple model inference the computation of the complete predictive posterior distribution was not prohibitively expensive; however, in the case that a complete Bayesian posterior distribution was too expensive to compute, as in the case of pool-based greedy active learning and multi-objective optimization, alternatives were considered. In greedy sampling with active learning discussed in **Section 3.4**, the computational complexity was principally driven by the large candidate pool and the complexity introduced by requiring the observed response in determining the predictive distribution, and thus inference about the response at unobserved feature vectors was obtained using **Eq 28** with the maximum *a posteriori* point estimate of the hyperparameters. On the other hand, in multi-objective optimization, the burden was principally associated with a large number of iterations, and thinning, as implemented in the work of Tapia et al. [27], was utilized. Preliminary investigations suggested thinning every 10^{th} iteration had a negligible impact on the model's predictive accuracy and was thus used in the iterative optimization procedure. The implementation of **Algorithm 1** and all related equations was realized using Python.

3.4 Active Learning: Batch Sampling

Due to the cost structure associated with AM as previously discussed in **Section 2.8**, pool-based batch active learning was selected as opposed to its sequential counterpart. In this work, the weight information gain expected model change maximization algorithm proposed by Zhao et al. [96] was implemented. Due to the size of the design space considered, it was not possible to solve for the maximum weight information gain by enumeration. Therefore, the approximate solution was determined using their greedy implementation, **Algorithm 2** [96].

Algorithm 2. Greedy sampling weight information gain [96].

Input: Labeled data set D, unlabeled data set U, candidate set $C \subset U$, batch size m, hyperparameters θ_{MAP}
Output: Query set C^*, unlabeled data set U
$C^* = \emptyset$
for i **in range**$(1, m)$:
  $D^* = D \cup C^*$
  $\boldsymbol{x}_i = \underset{x \in C}{\operatorname{argmax}}\, \rho(\boldsymbol{x})$
  $C = C / \boldsymbol{x}_i$
  $C^* = C^* \cup \boldsymbol{x}_i$
$U = U / C^*$
return C^*, U

In **Algorithm 2**, $\rho(\boldsymbol{x})$ is calculated according to **Eq 31**. It is interesting to note that **Eq 31** is equivalent to **Eq 30**, without the additional variance attributed to noise. Thus, it could be concluded that Zhao et al. [96] indirectly illustrated that greedy sampling of uncertainty considering the correlation among selected, but not yet labeled, samples approximates the set of samples which causes the greatest model change in the weight space. This can be computed since, given a point estimate of the Gaussian process regression hyperparameters, the predicted uncertainty is only dependent on the '*observed'* feature vectors and not their labels. Thus, in this work, the sampling algorithm will be referred to as greedy uncertainty sampling due to the popularity of uncertainty sampling and its more intuitive interpretation; however, with a note that it is based on the greedy sampling weight information gain algorithm presented in Ref. [96]. Nevertheless, from a greedy uncertainty sampling perspective, a maximum a posteriori point estimate of the hyperparameters, θ_{MAP}, was used to evaluate **Eq 31** since although the point estimate of the predictive uncertainty is label independent, the complete posterior distribution is label dependent. Lastly, for consistency with **Eq 30**, a constant noise term σ_n^2 was included in the active learning query strategy; however, this is a constant and thus does not affect the query strategy.

$$\rho(\boldsymbol{x}) = k(\boldsymbol{x},\boldsymbol{x}) - \boldsymbol{k}(\boldsymbol{D}^*,\boldsymbol{x})^T\left(\sigma_f^2\boldsymbol{K}(\boldsymbol{D}^*,\boldsymbol{D}^*) + \sigma_n^2\boldsymbol{I}\right)^{-1}\boldsymbol{k}(\boldsymbol{D}^*,\boldsymbol{x}) \qquad \textbf{Eq 31}$$

In this work, it was infeasible to even consider greedy sampling on the whole unlabeled pool, and thus a candidate set, C, comprised of $M = 1000$ candidate vectors, was randomly subsampled from the unlabeled pool at each iteration. Thereafter, an active learning iteration was composed of a batch of 24 unique feature vectors selected according to **Algorithm 2** and 8 center replicates from the CCD design. Due to the costs associated with LPBF and the timeline of the current project, a maximum of 3 prints were conducted consisting of the initial print and 2 active learning iterations. The implementation of **Algorithm 2** and all related equations was realized using Python.

3.5 Multi-Objective Optimization: NSGA-II

The implementation of NSGA-II was performed using *pymoo* – an open-source multi-objective optimization framework recently developed in collaboration between the original NSGA-II developer and their graduate student [100]. Based on the general multi-objective optimization problem formulation outlined in **Eq 6**, the current problem was expressed as **Eq 32**, where $f_1(\cdot)$ and $f_2(\cdot)$ represent relative density and build rate, respectively. In agreement with the *pymoo* framework, the problem was expressed strictly as a minimizing problem subject to less than or equal to constraints.

$$\min_{\boldsymbol{x}} -f_1(\boldsymbol{x}), -f_2(\boldsymbol{x}) \\ s.t.\ \boldsymbol{x}\boldsymbol{x}^{\boldsymbol{T}} - \alpha^{\boldsymbol{2}} \leq 0 \qquad \textbf{Eq 32}$$

Two main processes contribute to the controllable build rate during LPBF: laser scanning and powder recoating [67], [76]. Neglecting the LPBF process's auxiliary operations, including powder-related operations, **Eq 33** presents a commonly used simplified build rate model [4], [21], [22], [48], [76], [111]. In the build rate model, an equivalent scan speed is calculated using **Eq 34** defined similarly in [19], [21], where jump time, JT, is the time elapsed between laser pulses. Jump time directly influences the equivalent velocity, and due to its direct impact on the duty cycle, the average power of the modulated laser. Nevertheless, it was considered fixed in the current study. In this work, omitting powder-related considerations was deemed reasonable as Schwerz et al. [10] suggest that the scanning primarily determines the build time; however, it has been noted that the build rate is sensitive to print specific considerations, including build area utilization, geometric complexity, build layout, and build orientation [10], [48]. It is important to note that the build rate was evaluated in terms of physical units in the optimization framework.

$$Build\ Rate\ = vth \qquad \textbf{Eq 33}$$

$$v = \frac{PD}{ET + JT} \qquad \textbf{Eq 34}$$

The original NSGA-II algorithm proposed by Deb et al. is replicated in **Algorithm 3** [104]. In summary, an initial population is first constructed randomly, and an initial offspring population is generated. While the termination criteria, in this work less than a maximum number of iterations, is true, a combined population consisting of the parent and offspring populations is defined and sorted based on rank and crowding distance. While the size of the parent set of the next iteration remains below the population size, N, it is formed by sequentially adding the sorted fronts from the lowest rank onward. The final members are selected as the solutions with the highest crowding distance from the front which does not fit entirely in the next parent population until its population size is reached. A more complete description of NSGA-II along with the fast sorting and crowding distance algorithms can be found in the original work of Deb et al. [104], while an excellent summary of NSGA-II within LPBF related literature can be found in [67].

Algorithm 3. NSGA-II multi-objective optimization algorithm [104].

Input: Population size N, maximum generations T, crossover probability P_c, mutation probability P_m
Output: Non-dominated set of solutions, P_T
$P_0 = initialize\ population(N)$
$Q_0 = generate\ offspring(P_0)$
for t **in** range$(0, T - 1)$:
    $R_t = P_t \cup Q_t$
    $\mathcal{F} = sort(R_t)$
    $P_{t+1} = \emptyset; i = 1$
    while $|P_{t+1}| + |\mathcal{F}_i| \leq N$:
        $crowding\ distance(\mathcal{F}_i)$
        $P_{t+1} = P_{t+1} \cup \mathcal{F}_i$
        $i = i + 1$
    $sort(\mathcal{F}_i, \prec_n)$
    $P_{t+1} = P_{t+1} \cup \mathcal{F}_i[1\colon(N - |P_{t+1}|)]$
    $Q_{t+1} = generate\ offspring(P_{t+1})$
return P_T

Significant variations in the algorithm configuration can be observed in the literature, for example, in Refs. [109], [110], [111], [116], [117]. The current work adopted a similar configuration as presented in the original work [104] for real coded variables, with variations similar to the range of the above references. That is, the current work used a population size of 100, 150 iterations, crossover probability of 0.9, mutation probability of 0.25, simulated binary crossover with $\eta_c = 15$, and polynomial mutation with $\eta_m = 20$. The hypervolume metric, thought of as the volume enclosed in light blue in **Figure 7**, was used to estimate the convergence of the algorithm, while 3 runs were performed to determine the validity of the obtained non-dominated solutions.

4. Results and Discussion

4.1 Powder Characteristics

A representative particle size distribution of the Ti64 powders used in the work was measured using laser – diffraction particle size analysis, the results of which are shown in **Table 3** and **Figure 9 (a)**. The results show an increased presence of larger particles compared to the supplier reported distribution as indicated by the shifting of the distribution – most noticeable at the 90th percentile. In fact, the 10th and 50th percentiles remain marginally within the supplier-specified range for the virgin powder [112]. Nevertheless, the measured particle size distribution remains within common ranges for Ti64 based on the summary of Maitra et al. [16].

Table 3. Measured particle size distribution.

		D10 (µm)	D50 (µm)	D90 (µm)
Measured		23.3	35.2	52.6
AP&C [112]	(min)	17.0	30.0	42.0
	(max)	24.0	36.0	50.0

The corresponding particle morphology was examined using scanning electron microscopy – a representative image of which is shown in **Figure 9 (b)**. Despite the shifted particle size distribution, it is noted that the particles retain their spherical morphology – a characteristic of the plasma atomization process [48]. The shifting of the measured particle size distribution compared to their virgin counterparts can be attributed to the reusing of powder. The qualitative spheroidicity of the particles suggests that in contrast to agglomeration, particles with a diameter less than the nominal layer thickness are consumed during the printing process. Studying the effect of powder recycling on 316L stainless steel feedstock, Lu et al. [56] observed a similar shift of the particle distribution compared to their virgin counterpart, which they attribute to the favorable deposition of fine powders and the generation of spatter particles. Furthermore, Alfaify et al. [19] and Brika et al. [48] used similar arguments to explain observing near-identical properties of samples printed with drastically different particle size distributions and observing an increase in powder bed density with a decrease in layer thickness, respectively. As a result, it is suggested that particles larger than the nominal layer thickness are reused while smaller particles are consumed, leading to the observed drift of the distribution.

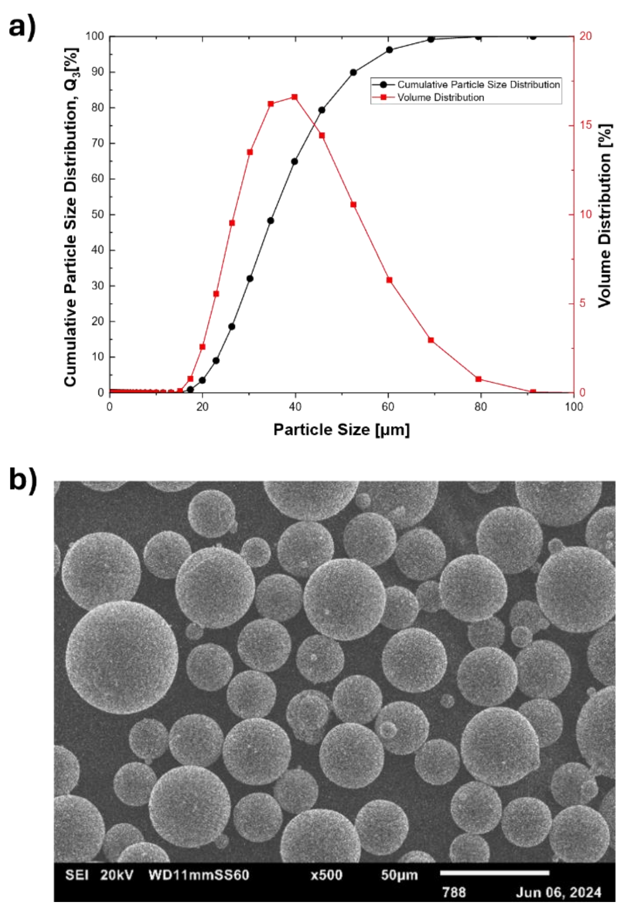

Figure 9. a) Particle size distribution, and b) particle morphology.

4.2 Initial Print: Central Composite Design

The relative density measurements of the initial central composite design are displayed in **Figure 10**. The uncertainty has been determined considering the resolution of the digital scale described in **Section 3.1** and the standard deviation of the experimental measurements. A 95 % confidence interval of the relative density of each sample is considered in this work using a t-distribution of 2 degrees of freedom ($t_{\alpha/2,n-1} = 4.303$). The lower and upper confidence limits are then used to determine the bounds of the transformed uncertainty.

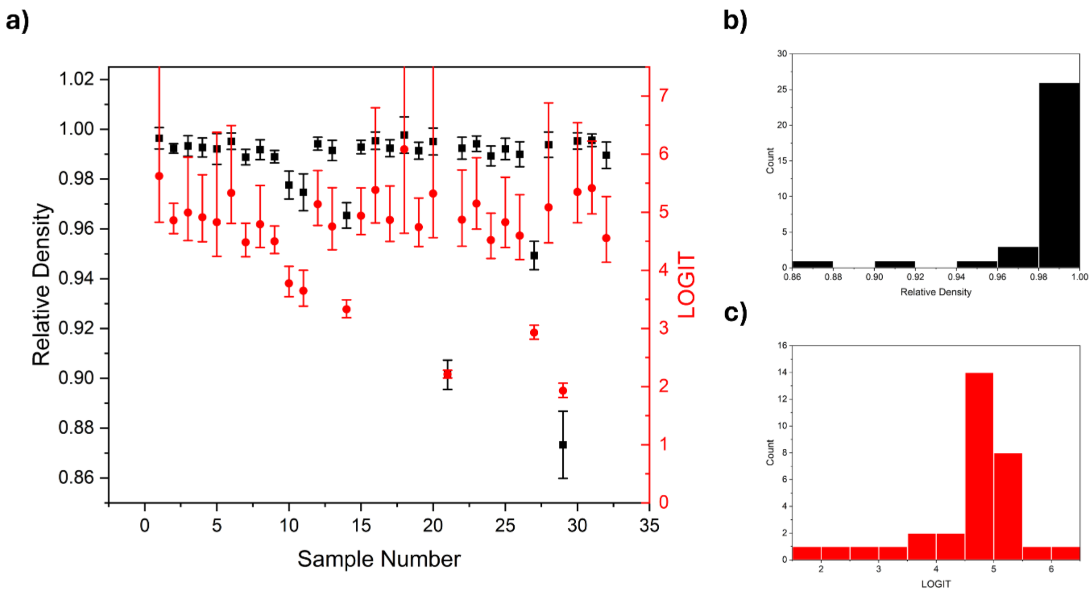

Figure 10. a) Relative density measurements and the Logit transformed response, b) histogram of the relative density, and c) histogram of the Logit transformed relative density.

Figure 10 (a) indicates three instances in which the uncertainty suggests achieving an experimental density greater than the theoretical density is feasible. This results in an upper confidence limit greater than 1 in the physical domain or an undefined confidence limit in the Logit domain. This can be explained by considering variability in alloying elements due to elemental vaporization during the melting and solidification process or simply by the sampling distribution. As summarized in the reviews of Oliveira et al. [9] and DebRoy et al. [2], due to the high melt pool temperature achieved in the LPBF process, volatile alloying elements may selectively vaporize and alter the chemical composition of the printed material. In the case of Ti64, aluminum may vaporize and sufficiently perturb the chemical composition to result in an observable change in theoretical density. Decreasing the concentration of aluminum (or any lightweight alloying elements) can increase the theoretical density of the printed material, and thus decrease its relative density.

Conversely, due to the limited number of measurements for each sample, $\nu = 2$, the t-distribution is relatively heavy-tailed compared to the normal distribution. This results in a wide confidence interval simply due to sampling. Since the width of the confidence interval is directly related to the sample size, increasing the sample size would likely reduce the width of the confidence interval such that its upper limit remains below 1. To accommodate for this, in this work the upper limit of these irregular confidence intervals is considered unbounded in the Logit domain for illustration.

Figure 10 (b) and **(c)** illustrate the effect of the data transformation on the distribution of the relative density. It is observed that the relative density distribution exhibits relatively severe negative skewness ($\gamma_1 = -3.22$) with 90 % of all observations exhibiting relative density greater than 95 %, similar to the summary reported by Maitra et al. [16]. After the Logit transformation, a more symmetric ($\gamma_1 = -1.52$), albeit rather leptokurtic ($\gamma_2 = 2.30$), distribution is achieved.

4.3 Model Configuration

4.3.1 Preliminary Model Configuration

It has been widely established that the mean and covariance functions determine the predictive ability of the Gaussian process regression model. Clear evidence of this pertaining to LPBF was presented in the previous work of Maitra et al. [16] and Zhang et al. [52] who clearly showed the variability of models' predictive ability depending on the kernel function. Among others, Quiepo et al. [71] and Forrester and Keane [70] suggest that an estimate of the model's predictive ability in terms of its generalization error is helpful in determining a suitable model. In this work, a suitable model refers to a suitable combination of mean and covariance functions. Based on the possible combinations of mean and covariance functions, the most suitable combination is chosen as that which minimizes the predictive error on the validation set. In this work average absolute relative error (AARE), **Eq 35**, and mean square error (MSE), **Eq 36**, were used to evaluate the predictive ability of each model configuration, where y and $\hat{y}$ are the observed and predicted response, respectively.

$$AARE = \frac{1}{n}\sum_{i=1}^{n}\frac{|y_i - \hat{y}_i|}{y_i} \times 100\% \qquad \textbf{Eq 35}$$

$$MSE = \frac{1}{n}\sum_{i=1}^{n}(y_i - \hat{y}_i)^2 \qquad \textbf{Eq 36}$$

Table 4 summarizes this predictive error of each model configuration. Based on the results and selection criteria, the constant and squared exponential functions were chosen as the most suitable mean and covariance functions, respectively.

Table 4. Gaussian process model predictive performance with various model configurations (AARE [%], MSE).

Mean Function	Kernel Function		
	Matérn 3/2	Matérn 5/2	Squared Exponential
Constant	10.88, 0.20	10.21, 0.18	**9.70, 0.15**
Linear	11.34, 0.21	10.76, 0.19	10.12, 0.17
Quadratic	11.65, 0.23	11.70, 0.24	11.58, 0.23

Table 4 indicates that the squared exponential kernel function paired with the constant mean function yields the highest predictive accuracy on the validation set. Furthermore, it is observed that the predictive accuracy generally deteriorates with increasing model complexity – that is, more parameterized mean functions and less smooth covariance functions. This is reasonably expected since overparameterized models with limited data tend to overfit the training data and generalize poorly to testing data [118]. Considering the quadratic mean function, the chosen covariance functions appear to exert little influence on the model's predictive ability.

The observations above support the previous work of Zhang et al. who demonstrated either the squared exponential or highly smoothed Matérn ($\nu = 18$) kernels were the most desirable kernels in terms of predictive accuracy using limited training data ($n = 20$) [52]. Nevertheless, the above results contradict the previous work of Maitra et al. [16], who found the constant mean and exponential kernel – a special case of the Matérn kernel with $\nu = 1/2$ - outperformed the squared exponential kernel chosen in this work. This is likely attributed to the larger training data set utilized in the prior work (446 unique feature vectors compared to the 25 unique feature vectors utilized in the current work) which likely has more intricate patterns due to the inherent non-linear nature of the LPBF process, thus requiring a kernel function which is able to produce less smooth function approximations.

4.3.2 Preliminary Model Convergence

Ill-convergence of MCMC sampling chains can result in misleading inferences based on an inaccurate representation of the posterior distribution and its summary statistics [87], [89], [119]. Considering the chosen model configuration, convergence was graphically evaluated using the marginal posterior distribution sample trace – a time sequence plot of the marginal posterior samples. More effective theoretically founded convergence criteria, such as those discussed in Ref. [119], remains as future work and outside the current scope. **Figure 11** illustrates the trace and kernel density estimate of the marginal posterior distribution for each hyperparameter over 11 independent sampling trials. The initial hyperparameters of each trial were randomly sampled with similar space filling properties to a Latin hypercube over-dispersed within the support of each of the prior distributions. Samples from the marginal posterior probability distribution of each hyperparameter were obtained from the sampled joint distribution by considering only the samples of the hyperparameter of interest [87], [120].

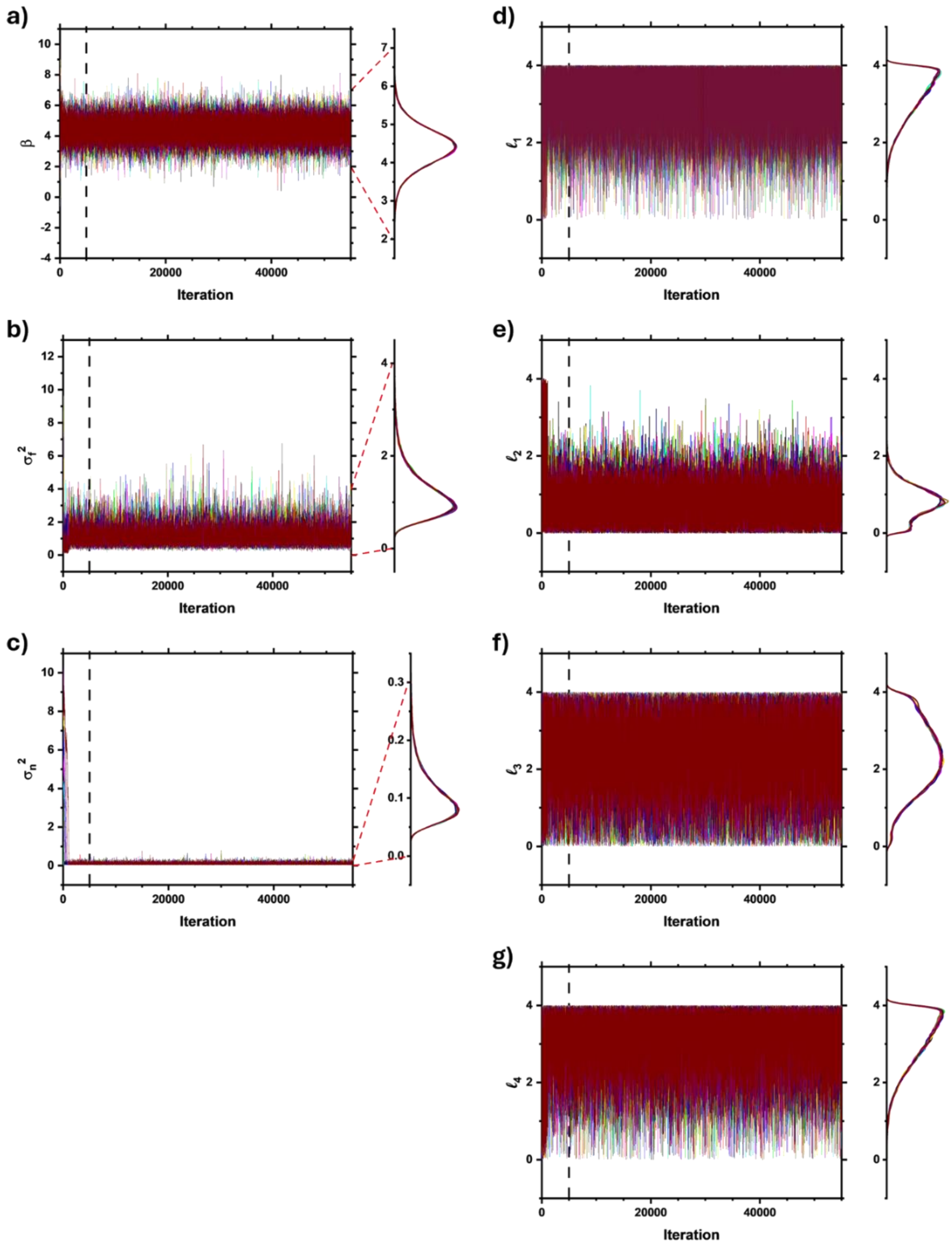

Figure 11. Trace of the marginal posterior distribution of a) β, b) σ_f^2, c) σ_n^2, d) ℓ_1, e) ℓ_2, f) ℓ_3, and g) ℓ_4 using the constant mean and squared exponential kernel functions over 11 independent sampling trials. The burn-in period is denoted by the dashed vertical line. The kernel density estimate of the sampled marginal distribution after the burn-in period for each trace is illustrated to the right. Positive density outside the support of the prior distribution is attributed to the kernel density estimate, as no samples exist in these regions. Marginal chains and distributions from each trial are plotted using different colors but become indistinguishable.

Roy discusses evaluating convergence in terms of determining when the Markov chain has reached the stationary distribution and determining when the sampling statistics are sufficiently close to the population statistics [119] – or more colloquially, they described this as determining when to start sampling and when to stop sampling, respectively. Using a burn-in period to address the convergence of the Markov chain to the stationary distribution, it is observed that during the burn-in period, clear and distinguishable traces are observed. This is more easily observed in the early iterations of the marginal trace of σ_n^2, **Figure 11 (c)**. This indicates the Markov chain has not reached its stationary distribution [89]. After the burn-in period, the traces become indistinguishable from one another indicating that all chains have converged to the stationary distribution. Thus, a burn-in period of 5000 is sufficient to suggest that all samples thereafter are drawn from the posterior distribution.

Among the various methods of estimating convergence, in this work, the convergence of the means of the multiple marginal chains with over-dispersed initial parameters is considered indicative that the sampling statistics reasonably approximate the population statistics of interest. A running mean plot of the marginal posterior distribution of each hyperparameter is shown in **Figure 12**. The running mean plot indicates reasonable convergence of the mean of each of the hyperparameters, thus indicating that 50000 iterations are sufficient to achieve a reasonable approximation of the population statistics. Furthermore, it is noted that the mean function hyperparameter converges much quicker and closer than the remaining hyperparameters. This is likely attributed to the conjugacy of its prior distribution, which allows its conditional posterior to be sampled directly using

Gibbs sampling. In conjunction with the trace plots of **Figure 11**, it is suggested that the MCMC sampling has converged.

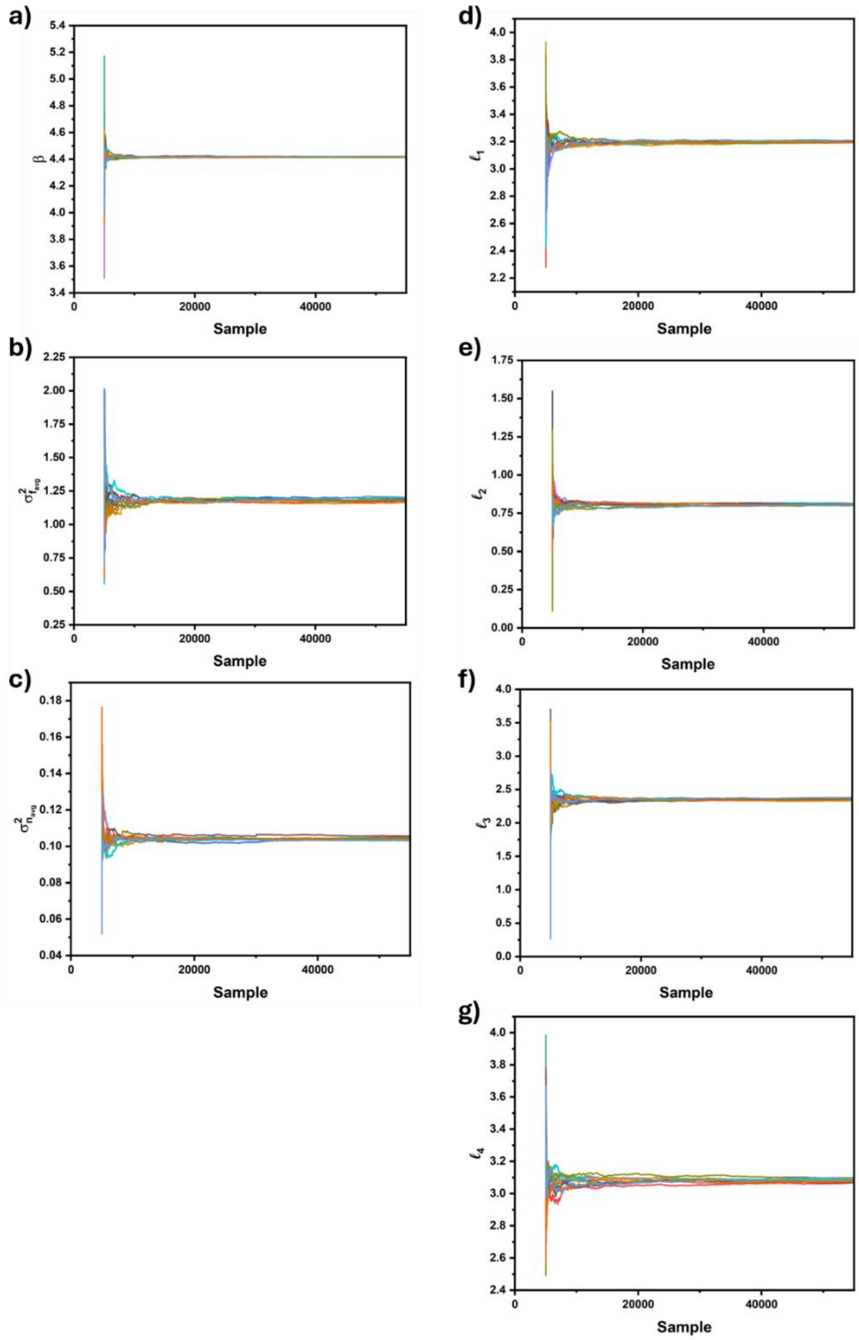

Figure 12. Running mean plot of the marginal posterior distribution of a) β, b) σ_f^2, c) σ_n^2, d) ℓ_1, e) ℓ_2, f) ℓ_3, and g) ℓ_4. The running mean considers only samples taken after the burn-in period using the constant mean and squared exponential kernel functions.

Despite appearing to have converged in the marginal posterior distribution, it is observed, as in the original work of Tapia et al., that the model scale hyperparameters tend to yield a relatively wide marginal distribution [31]. Tapia et al. originally attribute this to insufficient data – an argument supported in part by Ref. [87]. Both Congdon [87] and Qian [120] present a convincing alternative that suggests that marginal posterior distributions of highly correlated hyperparameters can cause poor convergences and may overestimate their uncertainty. Nonetheless, the posterior samples indicate minimal correlation with one another, which tends to support the original conclusions of Tapia and their collaborators. This further supports that active learning may be a viable approach to increase the precision of the hyperparameters' marginal posterior distribution, as Tapia et al. [31] has previously alluded.

4.4 Active Learning

4.4.1 Evolution of Marginal Posterior Probability Distribution

In general, additional data is expected to refine the posterior distribution as summarized in **Section 2.7** [31], [88]. **Figure 13** illustrates the evolution of the marginal posterior distribution of each hyperparameter as more data is collected through active learning. It is noted that **Figure 13** depicts the kernel density estimate of the sampled marginal distribution. The non-zero probability of the scale hyperparameters outside the prior support is attributed to kernel smoothing - no MCMC samples exist in this region as it is not permissible by the prior.

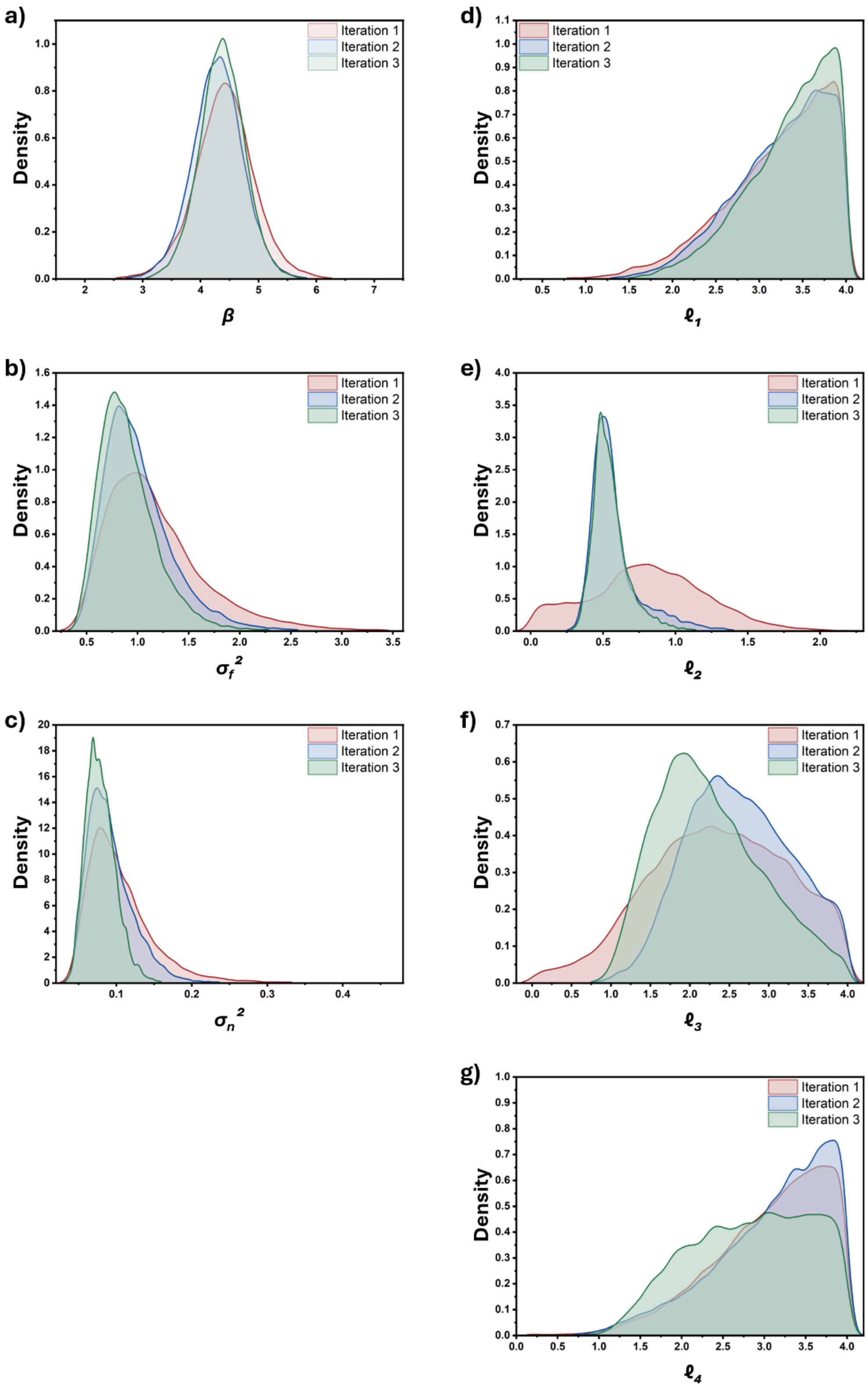

Figure 13. Evolution of the marginal posterior distribution of the hyperparameters a) β, b) σ_f^2, c) σ_n^2, d) ℓ_1, e) ℓ_2, f) ℓ_3, and g) ℓ_4.

The notion of increased precision with additional data, in general, is clearly evidenced in **Figure 13**, supporting the original work of Tapia et al. [31] and **Section 2.7**. As an example, paying particular attention to the marginal posterior probability distribution of σ_f^2, **Figure 13 (b)**, the width of the 95 % posterior credible interval decreases from 1.959 to 1.326, and finally 1.105 as additional data is accumulated between iterations 1, 2, and 3, respectively. **Figure 13 (e)**, corresponding to ℓ_2, illustrates the largest relative refinement in the marginal posterior distribution with the width of its 95 % credible interval decreasing from 1.581 to 0.736 before decreasing to 0.516 between iterations 1, 2, and 3, respectively. The refinement of the posterior distribution in conjunction with a denser sampling of the design space attributed to active learning is expected to decrease the predictive uncertainty of the response of an unobserved feature vector.

As the most notable exception to the notion of posterior refinement, a shift of the marginal posterior distribution of ℓ_4, **Figure 13 (g)**, is observed after the 3rd iteration. That is, the marginal posterior distribution appears to become more diffuse between the 2nd and 3rd iterations- a phenomenon counterintuitive to Bayesian inference and thus worth further investigation. It is worth noting again that analyzing a joint distribution in terms of its marginal distributions may overestimate the true variance of the parameters if they are correlated [120]; however, like the first iteration in **Section 4.3.1** the correlation among MCMC samples appears mild, albeit slightly higher. In similar vein as the illustrative example given in Tipping [88], given the assumption that all observations follow a joint Gaussian distribution imposed by the Gaussian process, the likelihood of all observations can be decomposed into the conditional likelihood of the current iteration given the previous iterations as **Eq 37**. In essence, the posterior distribution of the preceding iteration serves as the prior distribution of the current iteration as described in Ref. [88]; however, the likelihood is now conditioned on the observations of the previous iterations.

$$p(\boldsymbol{\theta}|\boldsymbol{y}_1, \boldsymbol{y}_2, \boldsymbol{y}_3)\ \alpha\ \underbrace{p(\boldsymbol{y}_3|\boldsymbol{y}_1, \boldsymbol{y}_2, \boldsymbol{\theta})}_{Iteration\ 3} \cdot \underbrace{p(\boldsymbol{y}_2|\boldsymbol{y}_1, \boldsymbol{\theta})}_{Iteration\ 2} \cdot \underbrace{p(\boldsymbol{y}_1|\boldsymbol{\theta})}_{Iteration\ 1} \cdot \underbrace{p(\boldsymbol{\theta})}_{Prior} \qquad \textbf{Eq 37}$$

Since the prior is unchanged throughout the active learning iterations, the shifting of the marginal posterior must be related to a corresponding shift in the likelihood. As such, **Figure 14** illustrates the contribution of each batch of samples on the overall likelihood of the data as a function of ℓ_4 over all MCMC sampling iterations. This can be thought of as the likelihood evaluated in the Metropolis algorithm acceptance probability, **Algorithm 1**, over all possible values of ℓ_4, and not just its proposed and current values.

Figure 14 indicates that the shift in the marginal distribution can be attributed not only to the 3rd iteration but also to the 2nd. That is, **Figure 14 (a)** illustrates a negatively skewed likelihood function with a large density associated with the upper range of the support of the prior distribution of ℓ_4 in agreement with the marginal posterior distribution after the 1st iteration illustrated in **Figure 13 (g)**. This may be attributed to the inherent nature of Occam's razor present in both the Gaussian likelihood [84], and Bayesian inference even under uninformative priors [88]. As additional data is collected and the design space becomes more densely sampled, **Figure 14 (b)** indicates that the conditional likelihood of $\boldsymbol{y}_2$ tends to assign a larger density to ℓ_4 in the lower range than originally present in **Figure 14 (a)**, indicating that the simpler representation initially favored no longer captures the observed data. This tends to support the discussion of **Section 4.3.1**, which suggested that increasing the amount of data may merit the consideration of a more non-linear mean and kernel function. Nevertheless, the low density of **Figure 14 (a)** outweighs the high density of **Figure 14 (b)** and their product, **Figure 14 (c)**, largely resembles the likelihood of **Figure 14 (a)**. As a result, minimal change is observed between the first two iterations of **Figure 13 (g)**. The shift in the marginal posterior distribution occurs when the conditional likelihood of $\boldsymbol{y}_3$, **Figure 14 (d)**, again assigns a larger density to ℓ_4 in the lower range than originally present in **Figure 14 (a)** which is sufficient to overcome its initial low density. Thus, the observed shift is not solely the result of the 3rd iteration but the culmination of the two active learning iterations as the sampling in the design space becomes denser.

As discussed in **Section 4.5**, the shifting of the marginal posterior distribution towards smaller values indicates a more significant effect of hatch spacing than initially inferred. Ozsoy et al. suggest that since point distance and hatch spacing play similar roles in terms of controlling the spatial energy distribution, their effects on the observed relative density are expected to be similar [17]. Thus, it is expected to observe a similar marginal posterior distribution of their corresponding hyperparameters. Therefore, although the marginal distribution of ℓ_4 after the 3rd iteration appears to be less informative than its predecessors, it is argued that it is more representative of the expected physical process than in the preceding iterations. Based on these results, it is postulated that if additional sampling were performed, its conditional likelihood would more closely resemble **Figure 14 (b)** and **(d)**, and the posterior marginal distribution would become more precise in the mid-region of the prior support of ℓ_4; however, the confirmation of this remains future work.

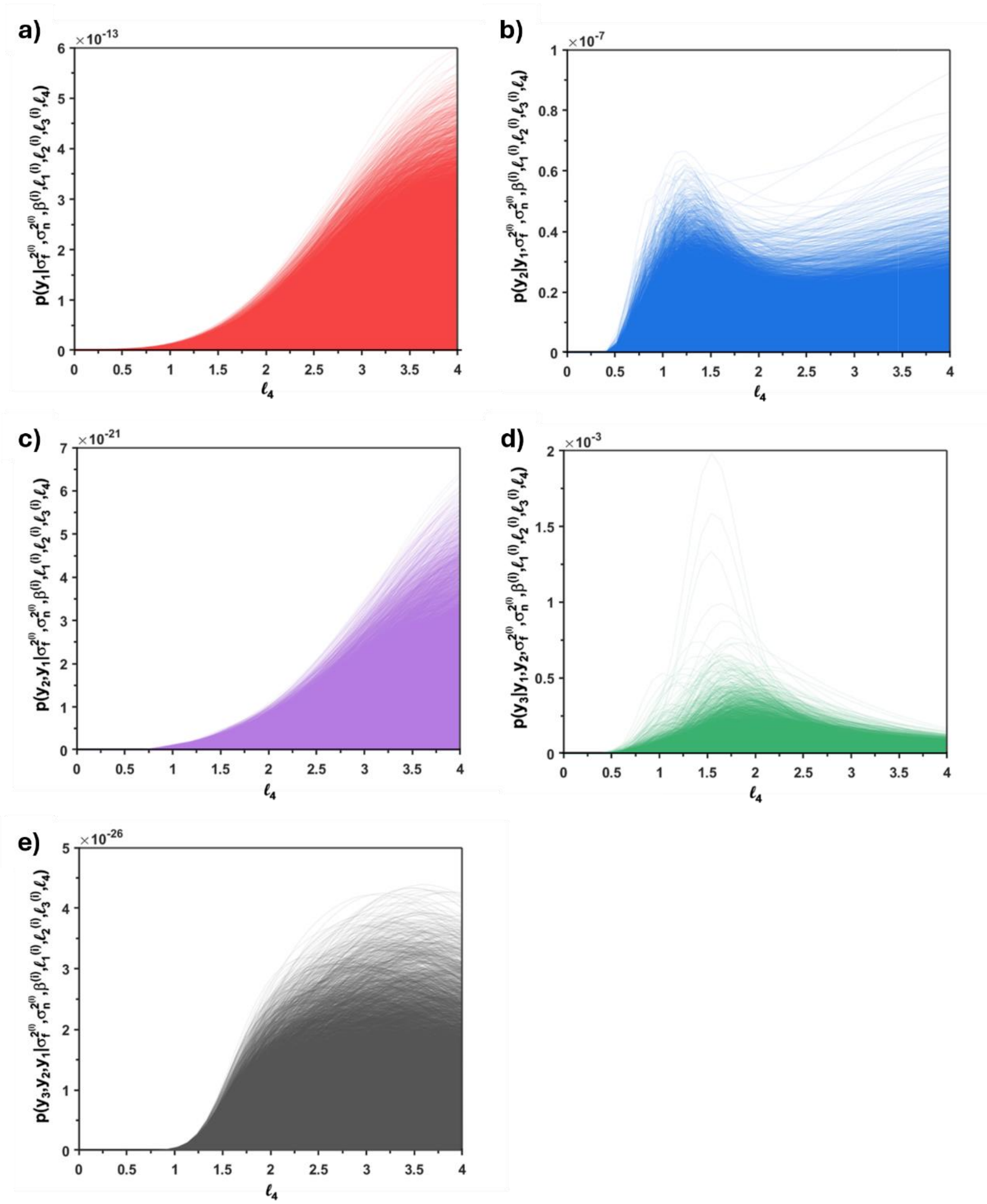

Figure 14. Evolution of the likelihood function for each iteration of MCMC as a function of ℓ_4, a) $p\left(\boldsymbol{y_1}|\beta^{(i)}, \sigma_f^{2^{(i)}}, \sigma_n^{2^{(i)}}, \ell_1^{(i)}, \ell_2^{(i)}, \ell_3^{(i)}, \ell_4\right)$, b) $p\left(\boldsymbol{y_2}|\boldsymbol{y_1}, \beta^{(i)}, \sigma_f^{2^{(i)}}, \sigma_n^{2^{(i)}}, \ell_1^{(i)}, \ell_2^{(i)}, \ell_3^{(i)}, \ell_4\right)$, c) $p\left(\boldsymbol{y_2}, \boldsymbol{y_1}|\, \beta^{(i)}, \sigma_f^{2^{(i)}}, \sigma_n^{2^{(i)}}, \ell_1^{(i)}, \ell_2^{(i)}, \ell_3^{(i)}, \ell_4\right)$, d) $p\left(\boldsymbol{y_3}|\boldsymbol{y_2}, \boldsymbol{y_1}, \beta^{(i)}, \sigma_f^{2^{(i)}}, \sigma_n^{2^{(i)}}, \ell_1^{(i)}, \ell_2^{(i)}, \ell_3^{(i)}, \ell_4\right)$, and e) $p\left(\boldsymbol{y_3}, \boldsymbol{y_2}, \boldsymbol{y_1}|\, \beta^{(i)}, \sigma_f^{2^{(i)}}, \sigma_n^{2^{(i)}}, \ell_1^{(i)}, \ell_2^{(i)}, \ell_3^{(i)}, \ell_4\right)$.

If the sampling of the design space is sparse with limited data, the model may not be able to accurately capture the influence of processing parameters and lead to inaccurate predictions and misleading conclusions. In the case of uncertainty-based active learning, inaccurate initial hyperparameters are detrimental as they can lead to inaccurate estimates of the predictive uncertainty and non-optimal querying of the candidate pool – a concept referred to as *starting cold* in Ref. [29]. A detrimental limitation of the application of active learning is that alone, it cannot be concluded if the querying strategy performed better than a baseline random sampling for the given problem or if starting cold was detrimental enough to render the active querying inferior to random sampling. Nevertheless, it is summarized that using active learning, the Bayesian inference Gaussian process regression model was able to more accurately capture the expected underlying mechanisms present in m-LPBF which were missed initially based on the initial experimental design.

4.4.2 Experimental Learning Curves

Figure 15 illustrates the evolution of the predictive distribution of the validation set as additional data is aggregated through active learning – the transformed experimental relative density and the corresponding 95 % confidence interval are illustrated as the grey vertical line and band superimposed over the predictive distribution, respectively. The width of the 95 % credible interval of the predictive distribution of all validation samples decreases through the active learning process, which can be attributed to two mechanisms: refinement of the posterior distribution and a denser sampling of the design space. In alignment with the observations of **Figure 13**, the width of the 95 % credible interval of the predictive distribution decreases most significantly between the 1st and 2nd iterations, while a more meager reduction is observed between the 2nd and 3rd iterations. Omitted from this work for brevity, the above results hold for the testing set.

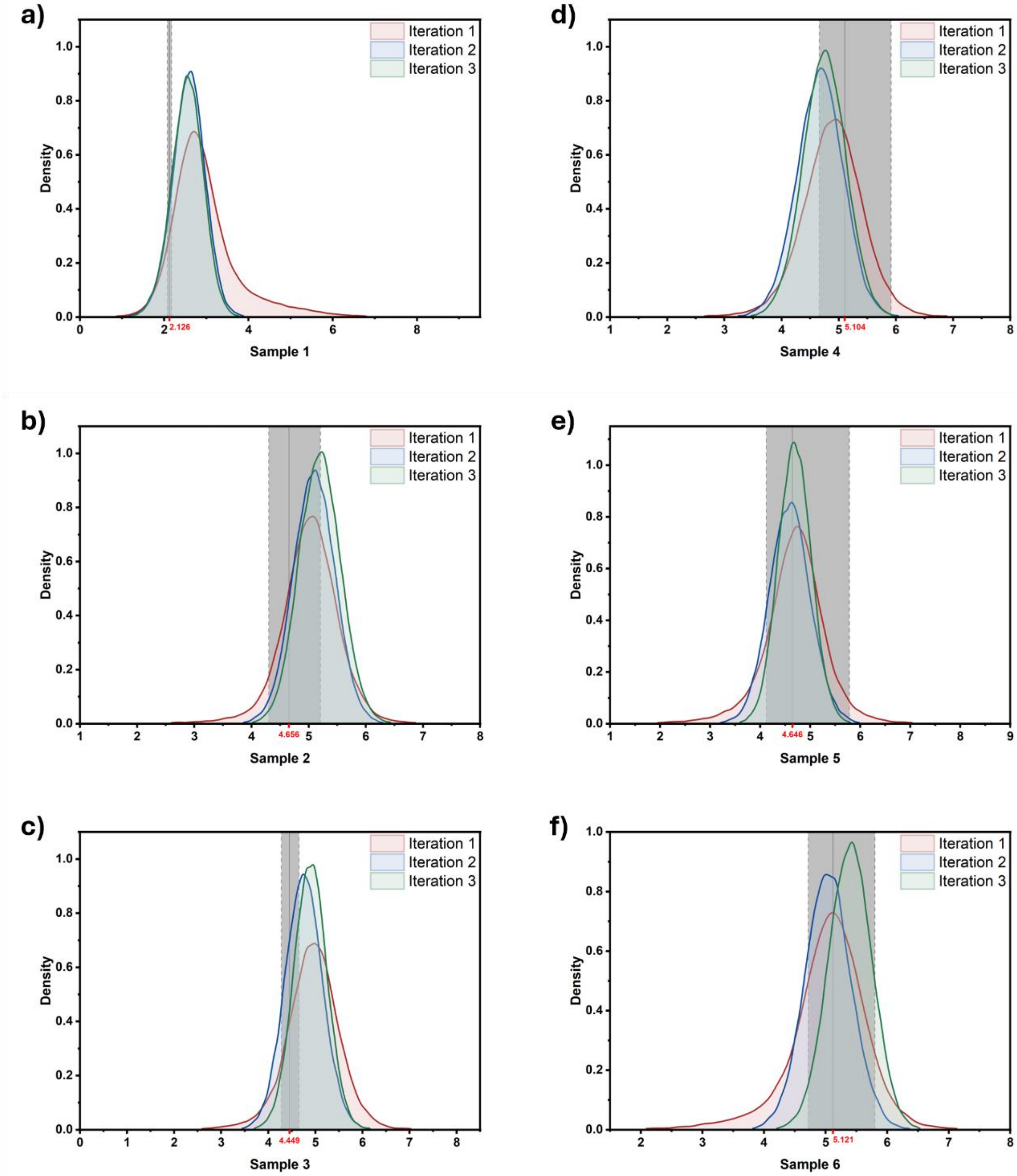

Figure 15. Evolution of the predictive distribution of the validation samples.

Although the reduction in the predictive credible interval's width is promising, it is insufficient to suggest that active learning efforts have been beneficial. In fact, if the width of the predictive distribution decreases so much so that the observed data is no longer within its bounds, the efforts of active learning would simply yield increased confidence in inaccurate predictions – a dangerous combination at best. **Figure 15** indicates that the measured response of the validation samples remains within the 95 % credible intervals over all 3 iterations, while although omitted this holds true for the testing set, thus reinforcing the effectiveness of active learning.

The error progression, or learning curve, of both the validation data set as well as the testing data set is presented in **Figure 16**.

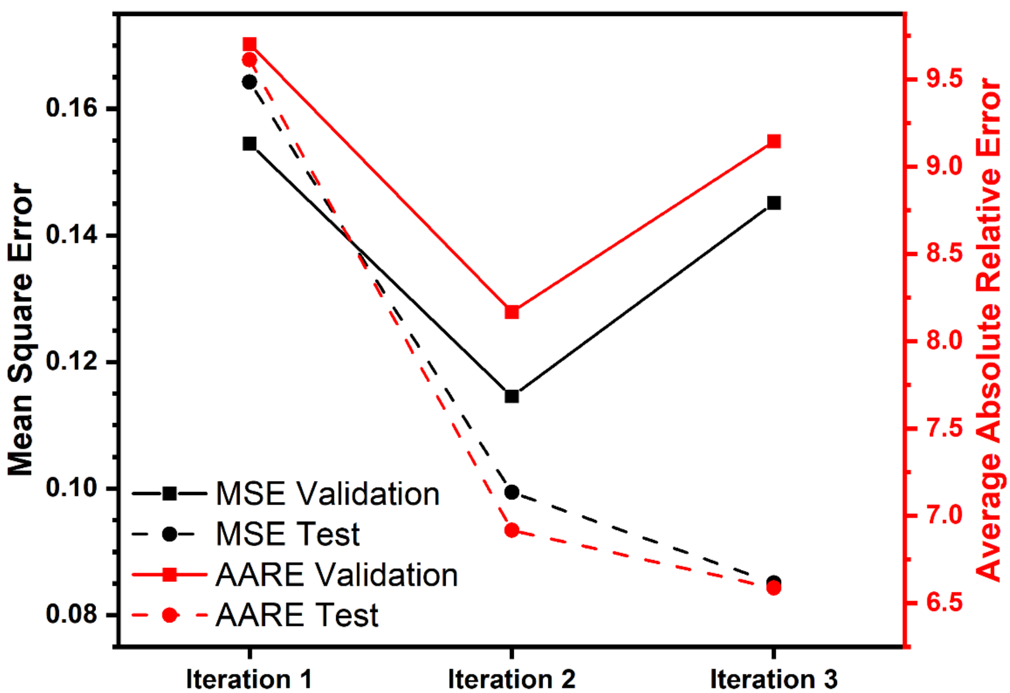

Figure 16. Error progression of both validation and testing data sets.

Figure 16 illustrates a significant reduction in AARE and MSE on the testing data set attributed to active learning, whereas a milder improvement on the validation set is observed. Considering the validation set's error progression, the AARE first decreases from 9.70 % to 8.17 % from the 1^{st} to 2^{nd} iteration, respectively, followed by a slight increase to 9.14 % in the 3^{rd} iteration, indicating an overall reduction of 0.56 %. On the other hand, the error progression of the testing set decreases from 9.61 % to 6.92 % between the 1^{st} and 2^{nd} iterations, and from 6.92 % to 6.59 % between the 2^{nd} and 3^{rd} iterations, respectively, indicating an overall reduction of 3.02 %. Overall, the progression of error indicates that active learning can effectively increase both the accuracy and the precision of the Gaussian process model.

4.4.3 Process Consistency

Levene's test of homogeneity indicates that there is strong evidence (p=0.009) to suggest that the variance of at least one iteration is statistically different than the variance of another iteration at a level of significance of 0.05. Considering **Figure 17 (a)** it becomes apparent that there is evidence to suggest inequality of variance between the first and third iterations. This may be attributable to the reproducibility of Archimedes method. The decreasing variance observed, but in the author's opinion not thoroughly mentioned or discussed, in the work of Bruce et al. [121] and the current study may be attributable to increased proficiency with the measurement technique, which Montgomery [115] attributes to be a potential source of heteroskedasticity.

Irrespective of the source of the heteroskedasticity, the unequal variance ANOVA, **Figure 17 (b)**, indicates that there is insufficient evidence (p=0.677) to suggest at a level of significance of α = 0.05 that the central tendency of the observations deviates between prints. Based on Levene's test, the unequal variance ANOVA, more specifically Welch's ANOVA, was adopted as it has been shown to be preferable to the traditional ANOVA when considering empirically obtained Type I and II error rates in many cases with heteroscedasticity in the work of Delacre et al. [114] and Liu [122]. Despite relaxing the assumption of homoscedasticity, Welch's ANOVA assumes independence and normality [122].

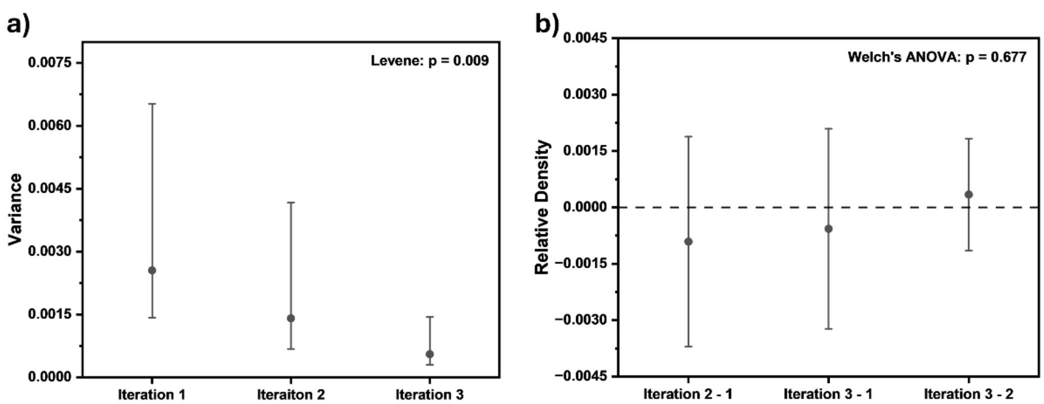

Figure 17. a) Levene's test of homogeneity (p=0.009). Confidence intervals of variance estimates with Bonferroni correction for family-wise significance, $\alpha = 0.05$, and b) Welch's ANOVA with unequal variance (p=0.677) with Games-Howell multiple comparisons.

Residual analysis reveals insufficient evidence of non-normality; however, despite best efforts through randomization and temperature accommodation, a slight temporal dependence appears in the first iteration which is not clearly apparent in later iterations. It is possible that this slight temporal dependence can be attributable to increasing proficiency throughout the active learning process; however, it also likely that this is related to temperature-dependent variations in the surface tension of the distilled water and the high surface roughness of the LPBF components, or through the introduction of impurities in the distilled water as measurements progress. Both the surface tension and the purity of the fluid have been previously established as a limitation of Archimedes method [113], [123]. Furthermore, Spierings et al. [113] suggest that the density of the fluid used in Archimedes should be less than 20% of that of the sample being measured - a threshold marginally surpassed in the current study, and which may contribute to higher experimental error. Thus, using acetone in place of distilled water, as explored in the study of Spierings et al. [113], may be beneficial due to its lower density and surface tension.

Future work could explore measuring relative density using other techniques such as optical microscopy or X-ray CT. The former is better suited for localized or microstructural studies rather than bulk density measurements, and has been shown in Spierings et al. [113] to exhibit high variability with low-density samples. Since low density samples are not only expected but encouraged in this study, optical microscopy may not be suitable. The latter may not be economically viable due to its high cost, time, and resolution required for quantitative and accurate measurements of relative density. Furthermore, the ASTM F3637-23 standard [123] suggests that it may be beneficial to incorporate the use of multiple measurement techniques; however, this is in direct conflict with the current objective of efficient model development. Moving forward, if the current framework adopts the Archimedes method (a cost and time-effective approach for bulk density measurement [113], [123]), it is strongly recommended to carefully control the temperature of the fluid used, change it regularly to ensure its purity, and independently examine center points after each batch. This would help mitigate potential issues and enable the early detection of potential temporal trends. Furthermore, the slight temporal trend, if driven by surface tension, may be mitigated through the use of a wetting agent as recommended by

Spierings et al. [113], and for example adopted by Brika et al. [48], if it has a negligible effect on the density of distilled water or if the effect can be accounted. Nevertheless, the temporal trend appears moderate, and thus, it is assumed that the results of Levene's test and Welches ANOVA are reasonable and the data from each iteration with distinct prints can be aggregated together.

4.5 Model Inference

Given the developed model, preliminary inference can be made: most notably, does the model support the fundamental argument of this work that exposure time and point distance must be considered independently for the m-LPBF process, and which parameters most significantly affect the relative density? To address the former, **Figure 18** depicts the predicted Logit response as a function of exposure time and point distance at various levels of hatch spacing. Laser power is held constant at 160 W. Similar to the work of Herzog et al. [4], the processing window in which a given relative density can be obtained decreases with increasing hatch spacing.

Bearing in mind that a unit change in the upper range of the response is less significant than a unit change in the lower range due to the Logit transformation, significant variation in the predicted response can be observed along the constant velocity profiles. In fact, **Figure 18 (b)** shows that at a constant velocity of 2000 mm/s, the predicted Logit response ranged from 2.183 to 4.872 corresponding to 89.87 % and 99.24 % relative density, respectively. This confirms the foundation of this work, and the previously reported works including for example Ozsoy et al. [17] and Alfaify et al. [19] - both of whom suggest that exposure time and point distance must be considered independently.

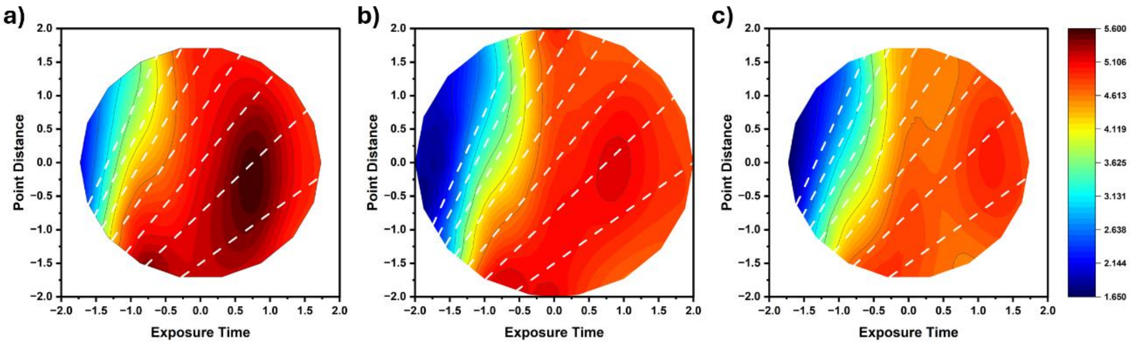

Figure 18. Predicted Logit relative density as a function of exposure time and point distance. Hatch spacing of a) 30 μm, b) 50 μm, and c) 70 μm. The dashed white lines indicate constant equivalent velocity.

Considering the latter, the magnitude of the scale hyperparameters for each input feature has been said to reflect their influence on the modelled response, for example, in Refs. [27], [28]. In the current work, the response is the Logit-transformed relative density. Considering the anisotropic squared exponential kernel function in **Eq 12**, larger length scales yield smaller exponents and a larger covariance, indicating a relatively small change in response with respect to the corresponding feature. On the other hand, smaller length scales yield larger exponents and a smaller covariance, indicating a more significant change in response with respect to the corresponding feature. Thus, features with smaller length scales can be considered to have a more significant effect on the response [28], [84].

Although the Logit-transformed response is used, in this work a more influential parameter on the transformed response is assumed to still be considered more influential on the observed response; however, it is important to note that Stevens et al. point out that a significant change in the transformed domain may not correspond to a significant change in the observed domain, most notable at the extremes [124]. Based on the median of the marginal posterior distribution after the 3rd iteration shown in **Figure 13**, the most to least significant parameters appear to be exposure time, point distance, hatch spacing, and laser power. More specifically, in the aforementioned order, the median of the marginal posterior distribution for each characteristic length scale hyperparameter is 0.53, 2.16, 2.89, and 3.44, respectively. It is worth noting that the above order remains consistent with the maximum *a posteriori* hyperparameter sample, although the magnitude differs.

Adopting a similar line of thought to Ozsoy et al. [17] and Panahizadeh et al. [110], the order of significance can be related to the physical process in terms of their effect on power density, q, as expressed by the Gaussian heat source model, **Eq 38**, [17], where LP and ET, are laser power and exposure time, respectively, a is the radius of the laser heat source, and r is the radial distance from its center.

$$q = 3\frac{LP \cdot ET}{\pi a^2}\exp\left(\frac{-3r^2}{a^2}\right) \qquad \textbf{Eq 38}$$

Figure 19 graphically depicts the effects of laser power and exposure time on the applied power density of a single pulse. Both parameters are varied from their lower factorial level, -1, to their upper factorial level, +1, of the CCD design while all other parameters are held constant at their center level.

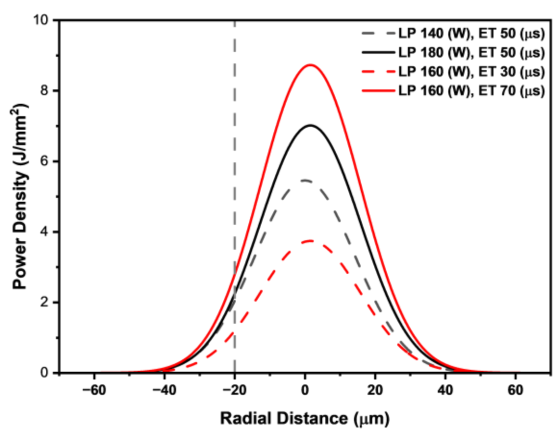

Figure 19. Effect of laser power and exposure time on power density.

It is observed that the applied power density is more significantly affected by variation in exposure time than laser power within the current design space. This can be attributed to the coding associated with the initial CCD design and the chosen parameter levels. For exposure time and laser power, an increase from their lower to upper coded levels indicates an increase in their magnitude of 40 μs and W, respectively. Despite equivalent magnitude, the above represents a 2.33- and 1.29-fold increase in exposure time and laser power over their lower factorial levels in physical units, respectively. Since q is proportional to their product, a change in exposure time more significantly affects power density than a change of laser power of equivalent coded magnitude simply due to the coding scale within the given design space.

With exposure time at its center level, the upper and lower power density profiles of **Figure 19** can be achieved with a laser power of 224 W and 96 W, respectively. Not only are these outside of the bounds of the current design space, 224 W is outside of the bounds of what is permissible using the Renishaw AM250 machine equipped with a 200 W ytterbium fiber laser source. Exposure time, on the contrary, is not constrained by the machine and is controlled instead by the slicing software, thus providing greater control over the process and resulting relative density.

Despite its significance, there are limits to the ability of exposure time alone to produce high-density components. As observed in **Figure 19**, increasing exposure time increases the power density near the center of the power source. This has been shown to increase the depth and diameter of the melt pool [21]. Irrespective of the exposure time applied, the power density appears to saturate near a radial distance of 50 μm, implying a saturation limit to the melt pool diameter. This issue can be exacerbated by the decreased thermal conductivity associated with the powder bed, which tends to promote heat transfer to bulk material over the surrounding powder [20], [125]. Saturation of the melt pool diameter was experimentally confirmed in the work of Onal et al. [126] who found the melt pool diameter of Ti64 saturated at approximately 520 μm, albeit at significantly higher energy conditions than considered in this work. Thus, this suggests that point distance and hatch spacing must be selected appropriately to ensure sufficient overlap between the discrete pools, and hence their intermediate importance. This supports the experimental work of Demir et al. [14] who, using 18Ni300 maraging steel, concluded that the temporal characteristics of the laser emission are more influential than the spatial characteristics of the laser emission on the observed porosity.

Under similar experimental conditions, Alfaify et al. [19] determined the order of significance of the m-LPBF parameters to be in descending order: point distance, hatch spacing, layer thickness, laser power, and exposure time. Excluding layer thickness which is not considered in the current study, the notable discrepancy between the current work and that of Alfaify is the effect of exposure time – the most and least significant parameter in the former and latter works, respectively. Although both works use similar ranges for point distance, hatch spacing, and laser power, there is a large discrepancy between the ranges of exposure time – 10 to 90 μs in the current work and 50 to 200 μs in the study conducted by Alfaify. **Figure 18** indicates the Gaussian process model predicts a minimal effect of exposure time above 50 μs in agreement with the work of Alfaify. The significance of exposure time becomes apparent at its lower range – an effect surmised to be related to the formation of lack-of-fusion porosity. It is postulated that the current work primarily explores the lack-of-fusion domain of the design space in an effort to increase the build rate, while the work of Alfaify et al. primarily explores the conduction and keyhole melting modes, the transition between which is less apparent than the lack-of-fusion to conduction transition [21], [39], [127]. Thus, it is suggested that results which indicate exposure time is both the most and least influential design parameter can both be true, depending on the design space explored.

4.6 Multi-Objective Optimization: Pareto Front

With reasonable confidence in the developed model, both through acceptable error metrics and physically interpretable and consistent model inference, NSGA-II is adopted to approximately determine the Pareto front. The set of non-dominated solutions approximating the Pareto front after 150 iterations for 3 independent trials is illustrated in **Figure 20**. It is observed from **Figure 20** that all 3 trials are in high agreement for relative density between 86.7 % and 99.7%, with each being nearly indistinguishable from one another. Nevertheless, they illustrate reasonably poor convergence below this threshold and moderate convergence above this threshold where the build rate and relative density single objective solutions exist, respectively. Thus, the theoretical argument presented in **Section 2.9** that incorporating a second objective will not affect the ability to determine the single objective solution appears to be highly dependent on the optimization algorithms' ability to converge to the extremes of the Pareto front. Nonetheless, all independent trials indicate convergence regarding hypervolume and stagnation in progress, thus representing converged solutions for the given trial.

Similar to the work of Lu and Shi [67], it is reasonable to define only a portion of the Pareto front as suitable solutions for implementation, in essence imposing a post hoc constraint on the optimization problem. In their work, Lu and Shi [67] define the suitable range as above 97 % relative density; however, the work of Herzog et al. [4] and Kaletsch et al. [63] illustrated the detrimental effects of porosity to a level of 5 % and 9.9 %, or relative density as low as 95 % and 90.1 %, respectively, can be mitigated through HIP. Herzog et al. further summarize that a relative density as low as near 90% can be suitable for the HIP process. Thus in this work, 3 distinct regions are defined as illustrated in **Figure 20**: Zone 3 - regions conforming to the traditional threshold of relative density greater than 99 %, Zone 1 - regions below 90 % in which poor NSGA-II convergence is observed and little industry relevance is expected, and Zone 2 - regions between 90 and 99 % expected to be used either with HIP postprocessing or in their as-built state if deemed suitable for the desired application.

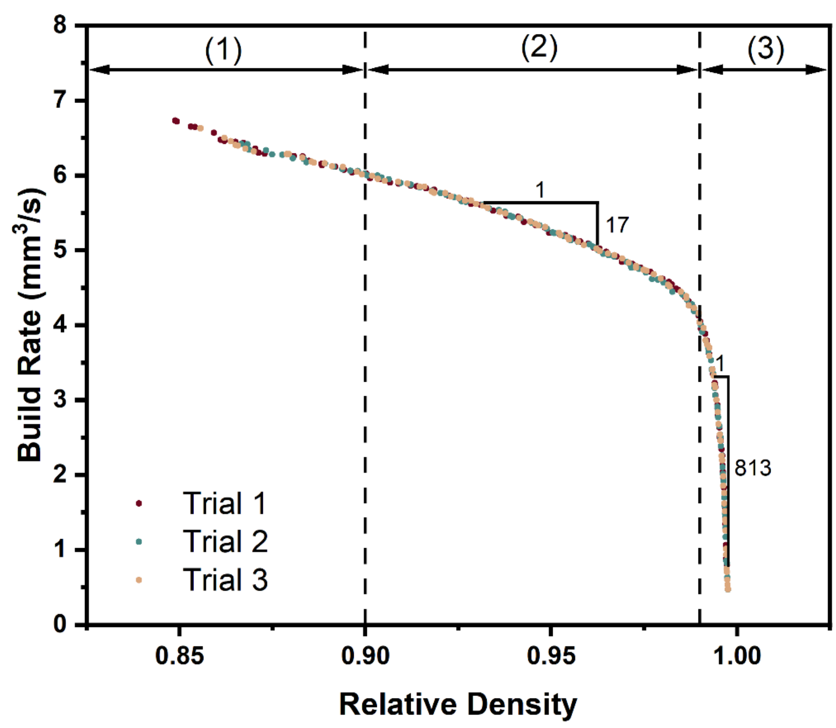

Figure 20. Pareto front: relative density and build rate. Region (1) indicates relative density less than 90 %, region (2) indicates relative density between 90 % and 99 %, and region (3) indicates relative density greater than 99 %. The slope is illustrative and not to scale, or representative of the precise data used in its approximation.

Again, like Lu and Shi [67], diminishing returns are observed when sacrificing relative density in exchange for increased build rates. Diminishing returns were also discussed in Lu and Shi [108] with respect to relative density and surface roughness when considering a weighted sum scalarization method. In this work, two distinct regions are identified in **Figure 20**. The first region identifies a significant increase in build rate from 0.47 to 3.17 mm^3/s by decreasing relative density from 99.8 to 99.4 % with an approximate best fit slope of 8.13 mm^3/s per unit % within the given range. However, outside of this region a significantly larger decrease in relative density from 96.9 to 90.2 % is required to achieve a more mild increase from 4.89 to 5.99 mm^3/s, with an approximate best fit slope of 0.17 mm^3/s per unit % within the given range. Thus, as discussed in the previous work, there is initially a large incentive to increase the build rate at the expense of decreasing relative density when the relative density is above 99 %. At the same time, there are diminishing returns as the relative density decreases, thus supporting the original conclusion of [67].

Lastly, Herzog et al. [4] report that EOS [128], a prominent LPBF equipment supplier, suggests Ti64 can be processed at 5 mm^3/s with a layer thickness of 30 μm, albeit under a c-LPBF machine equipped with a 400 W laser. In their report, EOS [128] suggests that under these conditions, a density of 4.41 g/cm^3 can be achieved, which they report as approximately 100 % relative density. In the current study, a theoretical density of 4.43 g/cm^3 is considered and thus the EOS density is converted as 99.5 %. This corresponds to an approximately 1.9-fold increase over the build rate obtained in the current study for a similar relative density. This increase can be attributed to the increased laser power compared to the current study, which widens the processing window, allowing for increased build rate [10], as well as the additional time consumed between pulses in the m-

LPBF process compared to its c-LPBF counterpart. Nevertheless, Ding et al. [15] suggested in their simulation study that under the same energy density the m-LPBF process required nearly 4 times the processing time per layer compared to c-LPBF; however, without a direct comparison of the resulting relative density. Despite the increased laser power capabilities of the EOS machine compared to the current study, this work illustrates that the discrepancy between the production abilities of m-LPBF and c-LPBF machines can be reduced by simultaneously optimizing relative density and processing rate.

5. Conclusion

Despite ambiguity over the preferred mode of laser emission in the LPBF process, c-LPBF has received a disproportionate amount of research efforts compared to m-LPBF. Traditionally considering c-LPBF, research efforts were devoted toward optimizing a single objective, most notably relative density or equivalently porosity. Recent trends have demonstrated the need to account for the competing objectives faced by today's industry. This work considers these recent trends and the limited efforts on m-LPBF by optimizing both the quality and time of the m-LPBF process in terms of relative density and build rate, respectively. To this end, the integration of Bayesian inference of a Gaussian process regression model with both batch-mode active learning and the popular NSGA-II multi-objective optimization algorithm was used to efficiently determine the tradeoff between quality and time of m-LPBF produced Ti64 samples. As a result of this work, the following conclusions have been made:

1) Batch mode active learning provided a means of efficiently improving the accuracy of the developed model, reducing the test set error from 9.61 % to 6.59 % over two iterations of 24 unique feature vectors each. Not only does predictive accuracy increase, but a noticeable increase in predictive precision was observed.
2) The Bayesian framework allowed for the evaluation of the progression of the marginal distribution of the hyperparameters. As expected, the marginal distributions typically exhibited increased precision with increasing amounts of data, the notable exception to which was the characteristic length scale of hatch spacing, ℓ_4. Decomposing the likelihood into the contributions of each iteration

revealed that both the 2nd and 3rd iterations suggest a shift in the marginal distribution, which agrees with the physical interpretation of the hyperparameter. However, without additional data, it is suggested that the initial model is unable to adequately capture the underlying process.

3) Model inferences support the established literature that point distance and exposure time must be considered independent parameters in m-LPBF, with relative density predicted to vary as much as from 89.87 % to 99.24 % at a constant equivalent velocity, laser power, hatch spacing, and layer thickness. The anisotropic squared exponential kernel indicated that exposure time is the most influential parameter within the design space. This is attributed to its significant influence on the applied power density.
4) Using NSGA-II, the relative density and build rate were optimized as a function of laser power, exposure time, point distance, and hatch spacing. Three independent optimization trials indicated that the NSGA-II was able to converge to a well-distributed non-dominated set of solutions; however, it shows inconsistency in the obtained extreme solutions. Based on the combined solutions, three distinct regions of the Pareto optimal front were established: regions that abide by traditional quality standards, regions that have been shown to be capable of being mended using HIP, and regions that, to the author's knowledge, are relatively unexplored.

To advance the work presented herein, various directions can be considered. As briefly mentioned previously, with limited data, there appears to be a trend to favor simpler mean and smoother kernel functions with the Gaussian process model. At the same time, the author's interpretation of the literature suggests that more non-linear models may be favored in LPBF with increasing data. Thus, a turning point may exist during active learning in which a simpler model is preferred initially while a more complex model can be exploited as the data set increases in size. The concept of changing models during the active learning process was briefly discussed in Ref. [29] and may present a promising direction for future work in metal-based AM. A well-established limitation of the current work, and for this reason it was omitted from **Section 1.2**, is that the optimal parameters are material and system dependent [12], [17], [28]. Lu et al. recently demonstrated transfer learning between two similar material systems using Bayesian inference and Gaussian process regression [94]. It is postulated in this work that a similar concept could be adopted in which the current posterior serves as the prior distribution of a similar material system to efficiently develop an accurate surrogate model and reduce the gap between the technological maturity of c-LPBF and m-LPBF. Lastly, in this work the conventional Gaussian process regression model has been adopted following the standard independent and identically distributed assumptions; however, the results indicate that a more flexible error structure in the model may be more effective in modelling the LPBF process. One potential solution may be the heteroskedastic models recently implemented in the works of Refs. [85], [90]. Nevertheless, this work serves as a foundation to close the gap between c-LPBF and m-LPBF and demonstrates the ability of batch-mode active learning and Bayesian inference with Gaussian process regression to efficiently optimize the m-LPBF process.

Bibliography

[1] J. J. Beaman, D. L. Bourell, C. C. Seepersad, and D. Kovar, “Additive Manufacturing Review: Early Past to Current Practice,” *Journal of Manufacturing Science and Engineering*, vol. 142, no. 11, Sep. 2020, doi: 10.1115/1.4048193.

[2] T. DebRoy *et al.*, “Additive manufacturing of metallic components – Process, structure and properties,” *Progress in Materials Science*, vol. 92, pp. 112–224, Mar. 2018, doi: 10.1016/j.pmatsci.2017.10.001.

[3] W. E. Frazier, “Metal Additive Manufacturing: A Review,” *J. of Materi Eng and Perform*, vol. 23, no. 6, pp. 1917–1928, Jun. 2014, doi: 10.1007/s11665-014-0958-z.

[4] D. Herzog, K. Bartsch, and B. Bossen, “Productivity optimization of laser powder bed fusion by hot isostatic pressing,” *Additive Manufacturing*, vol. 36, p. 101494, Dec. 2020, doi: 10.1016/j.addma.2020.101494.

[5] A. Khaimovich, A. Balyakin, M. Oleynik, A. Meshkov, and V. Smelov, “Optimization of Process Parameters for Powder Bed Fusion Additive Manufacturing Using a Linear Programming Method: A Conceptual Framework,” *Metals*, vol. 12, no. 11, Art. no. 11, Nov. 2022, doi: 10.3390/met12111976.

[6] W. E. King *et al.*, “Observation of keyhole-mode laser melting in laser powder-bed fusion additive manufacturing,” *Journal of Materials Processing Technology*, vol. 214, no. 12, pp. 2915–2925, Dec. 2014, doi: 10.1016/j.jmatprotec.2014.06.005.

[7] V. Maitra and J. Shi, “Predictability assessment of as-built hardness of Ti-6Al-4V alloy fabricated via laser powder bed fusion,” *Manufacturing Letters*, vol. 35, pp. 785–796, Aug. 2023, doi: 10.1016/j.mfglet.2023.08.113.

[8] B. J. Martins Freitas, G. Yuuki Koga, S. Arneitz, C. Bolfarini, and S. de Traglia Amancio-Filho, “Optimizing LPBF-parameters by Box-Behnken design for printing crack-free and dense high-boron alloyed stainless steel parts,” *Additive Manufacturing Letters*, vol. 9, p. 100206, Apr. 2024, doi: 10.1016/j.addlet.2024.100206.

[9] J. P. Oliveira, A. D. LaLonde, and J. Ma, “Processing parameters in laser powder bed fusion metal additive manufacturing,” *Materials & Design*, vol. 193, p. 108762, Aug. 2020, doi: 10.1016/j.matdes.2020.108762.

[10] C. Schwerz, F. Schulz, E. Natesan, and L. Nyborg, “Increasing productivity of laser powder bed fusion manufactured Hastelloy X through modification of process parameters,” *Journal of Manufacturing Processes*, vol. 78, pp. 231–241, Jun. 2022, doi: 10.1016/j.jmapro.2022.04.013.

[11] J. C. Snyder and K. A. Thole, “Understanding Laser Powder Bed Fusion Surface Roughness,” *Journal of Manufacturing Science and Engineering*, vol. 142, no. 071003, May 2020, doi: 10.1115/1.4046504.

[12] C. A. Biffi, J. Fiocchi, P. Bassani, and A. Tuissi, “Continuous wave vs pulsed wave laser emission in selective laser melting of AlSi10Mg parts with industrial optimized process parameters: Microstructure and mechanical behaviour,” *Additive Manufacturing*, vol. 24, pp. 639–646, Dec. 2018, doi: 10.1016/j.addma.2018.10.021.

[13] K. Fryzowicz, R. Dziurka, R. Bardo, M. Marciszko-Wiąckowska, and P. Bała, “Point-by-point laser exposure for crack susceptibility reduction in Powder Bed Fusion processing of H11 tool steel,” *Journal of Materials Processing Technology*, vol. 316, p. 117946, Jul. 2023, doi: 10.1016/j.jmatprotec.2023.117946.
[14] A. G. Demir, P. Colombo, and B. Previtali, “From pulsed to continuous wave emission in SLM with contemporary fiber laser sources: effect of temporal and spatial pulse overlap in part quality,” *Int J Adv Manuf Technol*, vol. 91, no. 5, pp. 2701–2714, Jul. 2017, doi: 10.1007/s00170-016-9948-7.
[15] X. Ding, L. Wang, and S. Wang, “Comparison study of numerical analysis for heat transfer and fluid flow under two different laser scan pattern during selective laser melting,” *Optik*, vol. 127, no. 22, pp. 10898–10907, Nov. 2016, doi: 10.1016/j.ijleo.2016.08.123.
[16] V. Maitra, J. Shi, and C. Lu, “Robust prediction and validation of as-built density of Ti-6Al-4V parts manufactured via selective laser melting using a machine learning approach,” *Journal of Manufacturing Processes*, vol. 78, pp. 183–201, Jun. 2022, doi: 10.1016/j.jmapro.2022.04.020.
[17] A. Ozsoy, E. Yasa, M. Keles, and E. B. Tureyen, “Pulsed-mode Selective Laser Melting of 17-4 PH stainless steel: Effect of laser parameters on density and mechanical properties,” *Journal of Manufacturing Processes*, vol. 68, pp. 910–922, Aug. 2021, doi: 10.1016/j.jmapro.2021.06.017.
[18] G. A. Tapia Imbaquingo, “Quantifying and reducing uncertainty in metal-based additive manufacturing laser powder-bed fusion processes,” Texas A&M University, 2018.
[19] A. Y. Alfaify, J. Hughes, and K. Ridgway, “Critical evaluation of the pulsed selective laser melting process when fabricating Ti64 parts using a range of particle size distributions,” *Additive Manufacturing*, vol. 19, pp. 197–204, Jan. 2018, doi: 10.1016/j.addma.2017.12.003.
[20] M. Saunders, “X marks the spot - find ideal process parameters for your metal AM parts,” Renishaw. Accessed: Dec. 14, 2024. [Online]. Available: http://www.renishaw.com/en/x-marks-the-spot-find-ideal-process-parameters-for-your-metal-am-parts--44325
[21] H. C. Hyer and C. M. Petrie, “Effect of powder layer thickness on the microstructural development of additively manufactured SS316,” *Journal of Manufacturing Processes*, vol. 76, pp. 666–674, Apr. 2022, doi: 10.1016/j.jmapro.2022.02.047.
[22] I. L. Fé-Perdomo, J. A. Ramos-Grez, R. Quiza, I. Jeria, and C. Guerra, “A novel optimization framework for minimizing the surface roughness while increasing the material processing rate in the SLM process of 316L stainless steel,” *Rapid Prototyping Journal*, vol. 29, no. 10, pp. 2216–2231, Sep. 2023, doi: 10.1108/RPJ-11-2022-0390.
[23] J. Li, J. Hu, L. Cao, S. Wang, H. Liu, and Q. Zhou, “Multi-objective process parameters optimization of SLM using the ensemble of metamodels,” *Journal of Manufacturing Processes*, vol. 68, pp. 198–209, Aug. 2021, doi: 10.1016/j.jmapro.2021.05.038.

[24] M. Marrey, E. Malekipour, H. El-Mounayri, and E. J. Faierson, “A Framework for Optimizing Process Parameters in Powder Bed Fusion (PBF) Process Using Artificial Neural Network (ANN),” *Procedia Manufacturing*, vol. 34, pp. 505–515, Jan. 2019, doi: 10.1016/j.promfg.2019.06.214.
[25] A. S. Raihan *et al.*, “A Data-Efficient Sequential Learning Framework for Melt Pool Defect Classification in Laser Powder Bed Fusion,” Nov. 16, 2024, *arXiv*: arXiv:2411.10822. doi: 10.48550/arXiv.2411.10822.
[26] L. Meng and J. Zhang, “Process Design of Laser Powder Bed Fusion of Stainless Steel Using a Gaussian Process-Based Machine Learning Model,” *JOM*, vol. 72, no. 1, pp. 420–428, Jan. 2020, doi: 10.1007/s11837-019-03792-2.
[27] G. Tapia, S. Khairallah, M. Matthews, W. E. King, and A. Elwany, “Gaussian process-based surrogate modeling framework for process planning in laser powder-bed fusion additive manufacturing of 316L stainless steel,” *Int J Adv Manuf Technol*, vol. 94, no. 9, pp. 3591–3603, Feb. 2018, doi: 10.1007/s00170-017-1045-z.
[28] Q. Liu, W. Chen, V. Yakubov, J. J. Kruzic, C. H. Wang, and X. Li, “Interpretable machine learning approach for exploring process-structure-property relationships in metal additive manufacturing,” *Additive Manufacturing*, vol. 85, p. 104187, Apr. 2024, doi: 10.1016/j.addma.2024.104187.
[29] J. Attenberg and F. Provost, “Inactive learning? difficulties employing active learning in practice,” *SIGKDD Explor. Newsl.*, vol. 12, no. 2, pp. 36–41, Mar. 2011, doi: 10.1145/1964897.1964906.
[30] R. Baker, “Method of Making Decorative Articles,” 1533300, Apr. 14, 1925
[31] G. Tapia, A. H. Elwany, and H. Sang, “Prediction of porosity in metal-based additive manufacturing using spatial Gaussian process models,” *Additive Manufacturing*, vol. 12, pp. 282–290, Oct. 2016, doi: 10.1016/j.addma.2016.05.009.
[32] A. Khaimovich, A. Balyakin, M. Oleynik, A. Meshkov, and V. Smelov, “Optimization of Process Parameters for Powder Bed Fusion Additive Manufacturing Using a Linear Programming Method: A Conceptual Framework,” *Metals*, vol. 12, no. 11, Art. no. 11, Nov. 2022, doi: 10.3390/met12111976.
[33] R. Huang *et al.*, “Energy and emissions saving potential of additive manufacturing: the case of lightweight aircraft components,” *Journal of Cleaner Production*, vol. 135, pp. 1559–1570, Nov. 2016, doi: 10.1016/j.jclepro.2015.04.109.
[34] S. H. Huang, P. Liu, A. Mokasdar, and L. Hou, “Additive manufacturing and its societal impact: a literature review,” *Int J Adv Manuf Technol*, vol. 67, no. 5, pp. 1191–1203, Jul. 2013, doi: 10.1007/s00170-012-4558-5.
[35] Y. Tian, R. Palad, and C. Aranas, “Microstructural evolution and mechanical properties of a newly designed steel fabricated by laser powder bed fusion,” *Additive Manufacturing*, vol. 36, p. 101495, Dec. 2020, doi: 10.1016/j.addma.2020.101495.
[36] S. Torres-Carrillo, H. R. Siller, C. Vila, C. López, and C. A. Rodríguez, “Environmental analysis of selective laser melting in the manufacturing of aeronautical turbine blades,” *Journal of Cleaner Production*, vol. 246, p. 119068, Feb. 2020, doi: 10.1016/j.jclepro.2019.119068.

[37] F. Bartolomeu, M. Gasik, F. S. Silva, and G. Miranda, "Mechanical Properties of Ti6Al4V Fabricated by Laser Powder Bed Fusion: A Review Focused on the Processing and Microstructural Parameters Influence on the Final Properties," *Metals*, vol. 12, no. 6, Art. no. 6, Jun. 2022, doi: 10.3390/met12060986.
[38] S. Cao, Y. Zou, C. V. S. Lim, and X. Wu, "Review of laser powder bed fusion (LPBF) fabricated Ti-6Al-4V: process, post-process treatment, microstructure, and property," *gxjzz*, vol. 2, no. 3, pp. 313–332, Sep. 2021, doi: 10.37188/lam.2021.020.
[39] A. du Plessis, "Effects of process parameters on porosity in laser powder bed fusion revealed by X-ray tomography," *Additive Manufacturing*, vol. 30, p. 100871, Dec. 2019, doi: 10.1016/j.addma.2019.100871.
[40] R. Smith, "3D Printing And The New Economics Of Manufacturing," Forbes. Accessed: Dec. 11, 2024. [Online]. Available: https://www.forbes.com/sites/ricksmith/2015/06/22/henry-ford-3d-printing-and-the-new-economics-of-manufacturing/
[41] R. D'Aveni, "3-D Printing Will Change the World." Accessed: Dec. 11, 2024. [Online]. Available: https://hbr.org/2013/03/3-d-printing-will-change-the-world
[42] Statutes of Canada, *Canadian Net-Zero Emissions Accountability Act*. 2021.
[43] C. R. Deckard, "Method and apparatus for producing parts by selective sintering," 4,863,538, Sep. 05, 1989
[44] R. Mertens, B. Vrancken, N. Holmstock, Y. Kinds, J.-P. Kruth, and J. Van Humbeeck, "Influence of Powder Bed Preheating on Microstructure and Mechanical Properties of H13 Tool Steel SLM Parts," *Physics Procedia*, vol. 83, pp. 882–890, Jan. 2016, doi: 10.1016/j.phpro.2016.08.092.
[45] D. Wang, Y. Liu, Y. Yang, and D. Xiao, "Theoretical and experimental study on surface roughness of 316L stainless steel metal parts obtained through selective laser melting," *Rapid Prototyping Journal*, vol. 22, no. 4, pp. 706–716, Jan. 2016, doi: 10.1108/RPJ-06-2015-0078.
[46] Y. Tian, K. Nyamuchiwa, K. Chadha, Y. He, and C. Aranas, "Laser powder bed fusion of M789 maraging steel on Cr–Mo N709 steel: Microstructure, texture, and mechanical properties," *Materials Science and Engineering: A*, vol. 839, p. 142827, Apr. 2022, doi: 10.1016/j.msea.2022.142827.
[47] L. Caprio, A. G. Demir, and B. Previtali, "Understanding the effects of temporal waveform modulation of the laser emission power in laser powder bed fusion: Part I - Analytical modelling," *J. Phys. D: Appl. Phys.*, vol. 55, no. 49, p. 495101, Oct. 2022, doi: 10.1088/1361-6463/ac984c.
[48] S. E. Brika, M. Letenneur, C. A. Dion, and V. Brailovski, "Influence of particle morphology and size distribution on the powder flowability and laser powder bed fusion manufacturability of Ti-6Al-4V alloy," *Additive Manufacturing*, vol. 31, p. 100929, Jan. 2020, doi: 10.1016/j.addma.2019.100929.
[49] H. D. Carlton, A. Haboub, G. F. Gallegos, D. Y. Parkinson, and A. A. MacDowell, "Damage evolution and failure mechanisms in additively manufactured stainless steel," *Materials Science and Engineering: A*, vol. 651, pp. 406–414, Jan. 2016, doi: 10.1016/j.msea.2015.10.073.
[50] Q. Liu, "Machine-Learning Assited Process Optimization for Laser Powder Fusion," The University of New South Wales, 2020.

[51] J. Reijonen, A. Revuelta, T. Riipinen, K. Ruusuvuori, and P. Puukko, "On the effect of shielding gas flow on porosity and melt pool geometry in laser powder bed fusion additive manufacturing," *Additive Manufacturing*, vol. 32, p. 101030, Mar. 2020, doi: 10.1016/j.addma.2019.101030.
[52] J. Zhang *et al.*, "A data-driven framework to improve the wear resistance of a low-alloy steel fabricated by laser powder bed fusion," *Journal of Manufacturing Processes*, vol. 115, pp. 56–67, Apr. 2024, doi: 10.1016/j.jmapro.2024.01.083.
[53] Y. W. Luo *et al.*, "Pore-affected fatigue life scattering and prediction of additively manufactured Inconel 718: An investigation based on miniature specimen testing and machine learning approach," *Materials Science and Engineering: A*, vol. 802, p. 140693, Jan. 2021, doi: 10.1016/j.msea.2020.140693.
[54] X. Yang, Y. Li, and B. Li, "Formation mechanisms of lack of fusion and keyhole-induced pore defects in laser powder bed fusion process: A numerical study," *International Journal of Thermal Sciences*, vol. 188, p. 108221, Jun. 2023, doi: 10.1016/j.ijthermalsci.2023.108221.
[55] Z. Wu *et al.*, "Study of Powder Gas Entrapment and Its Effects on Porosity in 17-4 PH Stainless Steel Parts Fabricated in Laser Powder Bed Fusion," *JOM*, vol. 73, no. 1, pp. 177–188, Jan. 2021, doi: 10.1007/s11837-020-04491-z.
[56] C. Lu *et al.*, "A comprehensive characterization of virgin and recycled 316L powders during laser powder bed fusion," *Journal of Materials Research and Technology*, vol. 18, pp. 2292–2309, May 2022, doi: 10.1016/j.jmrt.2022.03.125.
[57] S. A. Khairallah, A. T. Anderson, A. Rubenchik, and W. E. King, "Laser powder-bed fusion additive manufacturing: Physics of complex melt flow and formation mechanisms of pores, spatter, and denudation zones," *Acta Materialia*, vol. 108, pp. 36–45, Apr. 2016, doi: 10.1016/j.actamat.2016.02.014.
[58] L. Wang, Y. Zhang, H. Y. Chia, and W. Yan, "Mechanism of keyhole pore formation in metal additive manufacturing," *npj Comput Mater*, vol. 8, no. 1, pp. 1–11, Jan. 2022, doi: 10.1038/s41524-022-00699-6.
[59] W. E. King *et al.*, "Observation of keyhole-mode laser melting in laser powder-bed fusion additive manufacturing," *Journal of Materials Processing Technology*, vol. 214, no. 12, pp. 2915–2925, Dec. 2014, doi: 10.1016/j.jmatprotec.2014.06.005.
[60] K. Darvish, Z. W. Chen, and T. Pasang, "Reducing lack of fusion during selective laser melting of CoCrMo alloy: Effect of laser power on geometrical features of tracks," *Materials & Design*, vol. 112, pp. 357–366, Dec. 2016, doi: 10.1016/j.matdes.2016.09.086.
[61] A. M. Aboutaleb, M. J. Mahtabi, M. A. Tschopp, and L. Bian, "Multi-objective accelerated process optimization of mechanical properties in laser-based additive manufacturing: Case study on Selective Laser Melting (SLM) Ti-6Al-4V," *Journal of Manufacturing Processes*, vol. 38, pp. 432–444, Feb. 2019, doi: 10.1016/j.jmapro.2018.12.040.
[62] J. Sripada *et al.*, "Effect of hot isostatic pressing on microstructural and micromechanical properties of additively manufactured 17–4PH steel," *Materials Characterization*, vol. 192, p. 112174, Oct. 2022, doi: 10.1016/j.matchar.2022.112174.

[63] A. Kaletsch, S. Qin, S. Herzog, and C. Broeckmann, “Influence of high initial porosity introduced by laser powder bed fusion on the fatigue strength of Inconel 718 after post-processing with hot isostatic pressing,” *Additive Manufacturing*, vol. 47, p. 102331, Nov. 2021, doi: 10.1016/j.addma.2021.102331.
[64] G. Kasperovich, J. Haubrich, J. Gussone, and G. Requena, “Correlation between porosity and processing parameters in TiAl6V4 produced by selective laser melting,” *Materials & Design*, vol. 105, pp. 160–170, Sep. 2016, doi: 10.1016/j.matdes.2016.05.070.
[65] U. Scipioni Bertoli, A. J. Wolfer, M. J. Matthews, J.-P. R. Delplanque, and J. M. Schoenung, “On the limitations of Volumetric Energy Density as a design parameter for Selective Laser Melting,” *Materials & Design*, vol. 113, pp. 331–340, Jan. 2017, doi: 10.1016/j.matdes.2016.10.037.
[66] A. Costa, G. Buffa, D. Palmeri, G. Pollara, and L. Fratini, “Hybrid prediction-optimization approaches for maximizing parts density in SLM of Ti6Al4V titanium alloy,” *J Intell Manuf*, vol. 33, no. 7, pp. 1967–1989, Oct. 2022, doi: 10.1007/s10845-022-01938-9.
[67] C. Lu and J. Shi, “Simultaneous consideration of relative density, energy consumption, and build time for selective laser melting of Inconel 718: A multi-objective optimization study on process parameter selection,” *Journal of Cleaner Production*, vol. 369, p. 133284, Oct. 2022, doi: 10.1016/j.jclepro.2022.133284.
[68] K. G. Prashanth, S. Scudino, T. Maity, J. Das, and J. Eckert, “Is the energy density a reliable parameter for materials synthesis by selective laser melting?,” *Materials Research Letters*, vol. 5, no. 6, pp. 386–390, Nov. 2017, doi: 10.1080/21663831.2017.1299808.
[69] G. Miranda *et al.*, “Predictive models for physical and mechanical properties of 316L stainless steel produced by selective laser melting,” *Materials Science and Engineering: A*, vol. 657, pp. 43–56, Mar. 2016, doi: 10.1016/j.msea.2016.01.028.
[70] A. I. J. Forrester and A. J. Keane, “Recent advances in surrogate-based optimization,” *Progress in Aerospace Sciences*, vol. 45, no. 1, pp. 50–79, Jan. 2009, doi: 10.1016/j.paerosci.2008.11.001.
[71] N. V. Queipo, R. T. Haftka, W. Shyy, T. Goel, R. Vaidyanathan, and P. Kevin Tucker, “Surrogate-based analysis and optimization,” *Progress in Aerospace Sciences*, vol. 41, no. 1, pp. 1–28, Jan. 2005, doi: 10.1016/j.paerosci.2005.02.001.
[72] D. Wu, “Pool-Based Sequential Active Learning for Regression,” May 12, 2018, *arXiv*: arXiv:1805.04735. doi: 10.48550/arXiv.1805.04735.
[73] R. H. Myers, D. C. Montgomery, and C. M. Anderson-Cook, *Response Surface Methodology Process and Product Optimization Using Designed Experiments*, 4th ed., 1 online resource (855 p.). vols. in New York Academy of Sciences Ser. Newark: John Wiley & Sons, Incorporated, 2016.
[74] A. I. Khuri and S. Mukhopadhyay, “Response surface methodology,” *WIREs Computational Statistics*, vol. 2, no. 2, pp. 128–149, 2010, doi: 10.1002/wics.73.
[75] X. Zhai and F. Chen, “A Review of Process Optimization for Additive Manufacturing Based on Machine Learning,” *Annals of Applied Mathematics*, vol. 39, no. 4, pp. 493–543, Jan. 2023, doi: 10.4208/aam.OA-2023-0023.

[76] H. Abdulla, H. An, I. Barsoum, and M. Maalouf, "Mathematical Modeling of Multi-Performance Metrics and Process Parameter Optimization in Laser Powder Bed Fusion," *Metals*, vol. 12, no. 12, Art. no. 12, Dec. 2022, doi: 10.3390/met12122098.
[77] M. Vilanova, R. Escribano-García, T. Guraya, and M. San Sebastian, "Optimizing Laser Powder Bed Fusion Parameters for IN-738LC by Response Surface Method," *Materials*, vol. 13, no. 21, Art. no. 21, Jan. 2020, doi: 10.3390/ma13214879.
[78] M. Yakout, M. A. Elbestawi, and S. C. Veldhuis, "Density and mechanical properties in selective laser melting of Invar 36 and stainless steel 316L," *Journal of Materials Processing Technology*, vol. 266, pp. 397–420, Apr. 2019, doi: 10.1016/j.jmatprotec.2018.11.006.
[79] Y. Yin, J. Zhang, J. Gao, Z. Zhang, Q. Han, and Z. Zan, "Laser powder bed fusion of Ni-based Hastelloy X superalloy: Microstructure, anisotropic mechanical properties and strengthening mechanisms," *Materials Science and Engineering: A*, vol. 827, p. 142076, Oct. 2021, doi: 10.1016/j.msea.2021.142076.
[80] V. Maitra and J. Shi, "Evaluating the Predictability of Surface Roughness of Ti–6Al–4V Alloy from Selective Laser Melting," *Advanced Engineering Materials*, vol. 25, no. 14, p. 2300075, 2023, doi: 10.1002/adem.202300075.
[81] C. Kuo, C. Su, and A. Chiang, "Parametric optimization of density and dimensions in three-dimensional printing of Ti-6Al-4V powders on titanium plates using selective laser melting," *Int. J. Precis. Eng. Manuf.*, vol. 18, no. 11, pp. 1609–1618, Nov. 2017, doi: 10.1007/s12541-017-0190-5.
[82] C. Kamath and Y. J. Fan, "Regression with small data sets: a case study using code surrogates in additive manufacturing," *Knowledge and Information Systems*, vol. 57, no. 2, pp. 475–493, Nov. 2018, doi: 10.1007/s10115-018-1174-1.
[83] Q. Liu *et al.*, "Machine-learning assisted laser powder bed fusion process optimization for AlSi10Mg: New microstructure description indices and fracture mechanisms," *Acta Materialia*, vol. 201, pp. 316–328, Dec. 2020, doi: 10.1016/j.actamat.2020.10.010.
[84] C. E. Rasmussen and C. K. I. Williams, *Gaussian processes for machine learning*. in Adaptive computation and machine learning. Cambridge, Mass: MIT Press, 2006.
[85] D. Y. Kononenko, D. Chernyavsky, W. E. King, J. K. Hufenbach, J. van den Brink, and K. Kosiba, "Designing materials by laser powder bed fusion with machine learning-driven bi-objective optimization," *Journal of Materials Research and Technology*, vol. 30, pp. 6802–6811, May 2024, doi: 10.1016/j.jmrt.2024.05.046.
[86] M. Atiyat, "A Comparison of Frequentist and Bayesian Approaches for Linear Gaussian Process Models," Pennsylvania State University, 2008.
[87] P. Congdon, *Applied Bayesian modelling*, Second edition., 1 online resource (ix, 437 pages) : illustrations vols. Chichester, West Sussex: John Wiley & Sons, 2014.
[88] M. E. Tipping, "Bayesian Inference: An Introduction to Principles and Practice in Machine Learning," in *Advanced Lectures on Machine Learning: ML Summer Schools 2003, Canberra, Australia, February 2 - 14, 2003, Tübingen, Germany, August 4 - 16, 2003, Revised Lectures*, O. Bousquet, U. von Luxburg, and G. Rätsch, Eds., Berlin, Heidelberg: Springer, 2004, pp. 41–62. doi: 10.1007/978-3-540-28650-9_3.

[89] D. van Ravenzwaaij, P. Cassey, and S. D. Brown, “A simple introduction to Markov Chain Monte-Carlo sampling,” *Psychon Bull Rev*, vol. 25, no. 1, pp. 143–154, Feb. 2018, doi: 10.3758/s13423-016-1015-8.
[90] D. Chernyavsky, D. Y. Kononenko, J. H. Han, H. J. Kim, J. van den Brink, and K. Kosiba, “Machine learning for additive manufacturing: Predicting materials characteristics and their uncertainty,” *Materials & Design*, vol. 227, p. 111699, Mar. 2023, doi: 10.1016/j.matdes.2023.111699.
[91] D. Fullington, E. Yangue, M. M. Bappy, C. Liu, and W. Tian, “Leveraging small-scale datasets for additive manufacturing process modeling and part certification: Current practice and remaining gaps,” *Journal of Manufacturing Systems*, vol. 75, pp. 306–321, Aug. 2024, doi: 10.1016/j.jmsy.2024.04.021.
[92] W. Cai, M. Zhang, and Y. Zhang, “Batch Mode Active Learning for Regression With Expected Model Change,” *IEEE Transactions on Neural Networks and Learning Systems*, vol. 28, no. 7, pp. 1668–1681, Jul. 2017, doi: 10.1109/TNNLS.2016.2542184.
[93] B. Settles, “Active Learning Literature Survey,” University of Wisconsin-Madison Department of Computer Sciences, Technical Report, 2009. Accessed: Dec. 11, 2024. [Online]. Available: https://minds.wisconsin.edu/handle/1793/60660
[94] C. Lu, X. Jia, J. Lee, and J. Shi, “Knowledge transfer using Bayesian learning for predicting the process-property relationship of Inconel alloys obtained by laser powder bed fusion,” *Virtual and Physical Prototyping*, vol. 17, no. 4, pp. 787–805, Oct. 2022, doi: 10.1080/17452759.2022.2068447.
[95] A. M. Aboutaleb, L. Bian, A. Elwany, N. Shamsaei, S. M. Thompson, and G. Tapia, “Accelerated process optimization for laser-based additive manufacturing by leveraging similar prior studies,” *IISE Transactions*, vol. 49, no. 1, pp. 31–44, Jan. 2017, doi: 10.1080/0740817X.2016.1189629.
[96] Y. Zhao, J. Lin, J. Lin, and E. Q. Wu, “Batch-Mode Active Learning of Gaussian Process Regression With Maximum Model Change,” *IEEE Transactions on Systems, Man, and Cybernetics: Systems*, vol. 53, no. 12, pp. 7894–7900, Dec. 2023, doi: 10.1109/TSMC.2023.3323137.
[97] S. Mojumder, Z. Gan, Y. Li, A. A. Amin, and W. K. Liu, “Linking process parameters with lack-of-fusion porosity for laser powder bed fusion metal additive manufacturing,” *Additive Manufacturing*, vol. 68, p. 103500, Apr. 2023, doi: 10.1016/j.addma.2023.103500.
[98] G. J. J. van Houtum and M. L. Vlasea, “Active learning via adaptive weighted uncertainty sampling applied to additive manufacturing,” *Additive Manufacturing*, vol. 48, p. 102411, Dec. 2021, doi: 10.1016/j.addma.2021.102411.
[99] D. Wu, V. J. Lawhern, S. Gordon, B. J. Lance, and C.-T. Lin, “Offline EEG-Based Driver Drowsiness Estimation Using Enhanced Batch-Mode Active Learning (EBMAL) for Regression,” May 12, 2018, *arXiv*: arXiv:1805.04737. doi: 10.48550/arXiv.1805.04737.
[100] J. Blank and K. Deb, “Pymoo: Multi-Objective Optimization in Python,” *IEEE Access*, vol. 8, pp. 89497–89509, 2020, doi: 10.1109/ACCESS.2020.2990567.
[101] F. Murat, İ. Kaymaz, A. T. Şensoy, and İ. H. Korkmaz, “Determining the Optimum Process Parameters of Selective Laser Melting via Particle Swarm

Optimization Based on the Response Surface Method," *Met. Mater. Int.*, vol. 29, no. 1, pp. 59–70, Jan. 2023, doi: 10.1007/s12540-022-01205-9.

[102] N. Srinivas and K. Deb, "Muiltiobjective Optimization Using Nondominated Sorting in Genetic Algorithms," *Evolutionary Computation*, vol. 2, no. 3, pp. 221–248, Sep. 1994, doi: 10.1162/evco.1994.2.3.221.

[103] J. S. Arora, *Introduction to optimum design*, Fourth edition. Amsterdam: Academic Press is an imprint of Elsevier, 2017.

[104] K. Deb, A. Pratap, S. Agarwal, and T. Meyarivan, "A fast and elitist multiobjective genetic algorithm: NSGA-II," *IEEE Transactions on Evolutionary Computation*, vol. 6, no. 2, pp. 182–197, Apr. 2002, doi: 10.1109/4235.996017.

[105] F. Ahsan, J. Razmi, and L. Ladani, "Process Parameter Optimization in Metal Laser-Based Powder Bed Fusion Using Image Processing and Statistical Analyses," *Metals*, vol. 12, no. 1, Art. no. 1, Jan. 2022, doi: 10.3390/met12010087.

[106] S. E. Brika, Y. F. Zhao, M. Brochu, and J. Mezzetta, "Multi-Objective Build Orientation Optimization for Powder Bed Fusion by Laser," *Journal of Manufacturing Science and Engineering*, vol. 139, no. 111011, Sep. 2017, doi: 10.1115/1.4037570.

[107] Y. Deng, Z. Mao, N. Yang, X. Niu, and X. Lu, "Collaborative Optimization of Density and Surface Roughness of 316L Stainless Steel in Selective Laser Melting," *Materials*, vol. 13, no. 7, Art. no. 7, Jan. 2020, doi: 10.3390/ma13071601.

[108] C. Lu and J. Shi, "Relative density and surface roughness prediction for Inconel 718 by selective laser melting: central composite design and multi-objective optimization," *Int J Adv Manuf Technol*, vol. 119, no. 5, pp. 3931–3949, Mar. 2022, doi: 10.1007/s00170-021-08388-2.

[109] J. Li, J. Hu, L. Cao, S. Wang, H. Liu, and Q. Zhou, "Multi-objective process parameters optimization of SLM using the ensemble of metamodels," *Journal of Manufacturing Processes*, vol. 68, pp. 198–209, Aug. 2021, doi: 10.1016/j.jmapro.2021.05.038.

[110] V. Panahizadeh, A. H. Ghasemi, Y. D. Asl, and M. Davoudi, "Optimization of LB-PBF process parameters to achieve best relative density and surface roughness for Ti6Al4V samples: using NSGA-II algorithm," *Rapid Prototyping Journal*, vol. 28, no. 9, pp. 1821–1833, Jun. 2022, doi: 10.1108/RPJ-09-2021-0238.

[111] L. E. Criales, Y. M. Arısoy, B. Lane, S. Moylan, A. Donmez, and T. Özel, "Predictive modeling and optimization of multi-track processing for laser powder bed fusion of nickel alloy 625," *Additive Manufacturing*, vol. 13, pp. 14–36, Jan. 2017, doi: 10.1016/j.addma.2016.11.004.

[112] AP&C, "Plasma Atomized Powder Specifications: PA-PS-020/Rev.1." Nov. 18, 2022.

[113] A. B. Spierings, M. Schneider, and R. Eggenberger, "Comparison of density measurement techniques for additive manufactured metallic parts," *Rapid Prototyping Journal*, vol. 17, no. 5, pp. 380–386, 2011, doi: 10.1108/13552541111156504.

[114] M. Delacre, C. Leys, Y. L. Mora, and D. Lakens, "Taking Parametric Assumptions Seriously: Arguments for the Use of Welch's F-test instead of the Classical F-test in

One-Way ANOVA,” *International Review of Social Psychology*, vol. 32, no. 1, Aug. 2019, doi: 10.5334/irsp.198.
[115] D. C. Montgomery, *Design and analysis of experiments*, 5th ed. New York: John Wiley, 2001.
[116] F. Ma, H. Zhang, K. K. B. Hon, and Q. Gong, “An optimization approach of selective laser sintering considering energy consumption and material cost,” *Journal of Cleaner Production*, vol. 199, pp. 529–537, Oct. 2018, doi: 10.1016/j.jclepro.2018.07.185.
[117] C. Zhu *et al.*, “Multi-Objective Optimization of Selective Laser Melting Processes for Minimizing Energy Consumption and Maximizing Product Tensile Strength,” *Metals*, vol. 12, no. 11, Art. no. 11, Nov. 2022, doi: 10.3390/met12111782.
[118] R. O. Mohammed and G. C. Cawley, “Over-Fitting in Model Selection with Gaussian Process Regression,” in *Machine Learning and Data Mining in Pattern Recognition*, P. Perner, Ed., Cham: Springer International Publishing, 2017, pp. 192–205. doi: 10.1007/978-3-319-62416-7_14.
[119] V. Roy, “Convergence Diagnostics for Markov Chain Monte Carlo,” *Annual Review of Statistics and Its Application*, vol. 7, no. Volume 7, 2020, pp. 387–412, Mar. 2020, doi: 10.1146/annurev-statistics-031219-041300.
[120] S. S. Qian, “On model coefficient estimation using Markov chain Monte Carlo simulations: A potential problem and the solution,” *Ecological Modelling*, vol. 247, pp. 302–306, Dec. 2012, doi: 10.1016/j.ecolmodel.2012.08.020.
[121] D. Bruce *et al.*, “A critical assessment of the Archimedes density method for thin-wall specimens in laser powder bed fusion: Measurement capability, process sensitivity and property correlation,” *Journal of Manufacturing Processes*, vol. 79, pp. 185–192, Jul. 2022, doi: 10.1016/j.jmapro.2022.04.059.
[122] H. Liu, “Comparing Welch’s ANOVA, a Kruskal-Wallis test and traditional ANOVA in case of Heterogeneity of Variance,” Virginia Commonwealth University, 2015. [Online]. Available: https://scholarscompass.vcu.edu/etd/3985
[123] ASTM, *Standard Guide for Additive Manufacturing of Metal - Finished Part Properties - Methods for Relative Density Measurement*, ASTM F3637-23.
[124] S. Stevens, J. M. Valderas, T. Doran, R. Perera, and E. Kontopantelis, “Analysing indicators of performance, satisfaction, or safety using empirical logit transformation,” *BMJ: British Medical Journal*, vol. 352, 2016, doi: 10.1136/bmj.i1114.
[125] Z. Li, B.-Q. Li, P. Bai, B. Liu, and Y. Wang, “Research on the Thermal Behaviour of a Selectively Laser Melted Aluminium Alloy: Simulation and Experiment,” *Materials*, vol. 11, no. 7, Art. no. 7, Jul. 2018, doi: 10.3390/ma11071172.
[126] E. Onal, A. E. Medvedev, M. A. Leeflang, A. Molotnikov, and A. A. Zadpoor, “Novel microstructural features of selective laser melted lattice struts fabricated with single point exposure scanning,” *Additive Manufacturing*, vol. 29, p. 100785, Oct. 2019, doi: 10.1016/j.addma.2019.100785.
[127] T. Montalbano *et al.*, “Uncovering the coupled impact of defect morphology and microstructure on the tensile behavior of Ti-6Al-4V fabricated via laser powder bed fusion,” *Journal of Materials Processing Technology*, vol. 294, p. 117113, Aug. 2021, doi: 10.1016/j.jmatprotec.2021.117113.

[128] EOS, “Material Data Sheet, EOS Titanium Ti64,” 2022.

Curriculum Vitae

Candidate's Full Name: Thomas McCarthy

Universities Attended: University of New Brunswick, B.Sc. Mechanical Engineering, 2023

Publications:

1. **T. McCarthy**, H. Bongao, M. Tolentino, F. Zvavamwe, J. Pasco, G. Saha, and C. Aranas Jr, "Microstructural evolution of a low-carbon steel fabricated via wire-arc additive manufacturing: The effect of interpass time and number of layers," Eng. Res. Express, 2025, doi: 10.1088/2631-8695/adb541.

2. J. Pasco, C. Aranas, and **T. McCarthy**, "Gaussian process regression modelling and texture control during hot deformation of additively manufactured maraging steels," in *Supplemental UE: TMS 2025 Conference Proceedings*, 2025 (in press)

3. **T. McCarthy**, J. Pasco, and C. Aranas Jr, "Surrogate Modelling of Ti6Al4V Manufactured Via Pulsed Laser Powder Bed Fusion," in *Key Engineering Materials*, 2025 (under review).

4. A. Sankar, M. Manjaiah, **T. McCarthy**, J. Pasco, S. K. Ejera, and C. Aranas, "Grain disintegration and dynamic recrystallization during impact tests of additively manufactured nickel-based alloy 718," *J. Mater. Res. Technol.*, vol. 33, pp. 4844–4857, Nov. 2024, doi: 10.1016/j.jmrt.2024.10.157.

5. H. Bongao, M. Manjaiah, P. de Yro, J. Pasco, **T. McCarthy**, K. Nyamuchiwa, and C. Aranas, "High-temperature mechanical properties of additively manufactured 420 stainless steel," *Mater. Res. Express*, vol. 11, no. 5, p. 056501, May 2024, doi: 10.1088/2053-1591/ad425d.

6. K. Nyamuchiwa, J. Pasco, **T. McCarthy**, A. Keshavarzkermani, T. Wang, and C. Aranas, “Analysis of dynamic recrystallization through austenite grain reconstruction of additively manufactured martensitic M789 steel,” *Mater. Sci. Eng. A*, vol. 897, p. 146345, Apr. 2024, doi: 10.1016/j.msea.2024.146345.
7. H. Bongao, J. Pasco, **T. McCarthy**, K. Nyamuchiwa, and C. Aranas, “Softening Mechanisms in Additively Manufactured 420 Stainless Steel at Elevated Temperatures,” in *TMS 2024 153rd Annual Meeting & Exhibition Supplemental Proceedings*, Cham: Springer Nature Switzerland, Feb. 2024, pp. 244–253. doi: 10.1007/978-3-031-50349-8_23.

8. A. Sankar, M. Mallaiah, **T. McCarthy**, J. Pasco, M. Harding, and C. Aranas, “High-Strain Rate and High-Temperature Properties of Additively Manufactured Nickel-Based Alloy 718,” in *TMS 2024 153rd Annual Meeting & Exhibition Supplemental Proceedings*, Cham: Springer Nature Switzerland, Feb. 2024, pp. 224–234. doi: 10.1007/978-3-031-50349-8_21.

9. C. J. Aranas, K. Nyamuchiwa, K. Chadha, J. Pasco, and **T. McCarthy**, “Themomechanical Response of an Additively Manufactured Hybrid Alloy by Means of Powder Bed Fusion,” *Key Eng. Mater.*, vol. 964, pp. 117–122, Nov. 2023, doi: 10.4028/p-299lzX.
10. C. Aranas, J. Pasco, and **T. McCarthy**, “Material constitutive modelling of Fe-based, Ni-based and high-entropy alloys: Development of Simu-Mat 1.0,” *MRS Commun.*, vol. 12, no. 5, pp. 585–591, Oct. 2022, doi: 10.1557/s43579-022-00201-9.

11. J. Lewis, J. Pasco, **T. McCarthy**, K. Chadha, M. Harding, and C. Aranas, "High strain rate and high temperature mechanical response of additively manufactured alloy 625," *J. Manuf. Process.*, vol. 81, pp. 922–944, Sep. 2022, doi: 10.1016/j.jmapro.2022.07.047.

12. J. Pasco, **T. McCarthy**, J. Parlee, N. Nazri, S. Padmajan, S. Rodrigues, and C. Aranas, "Constitutive modeling of modified-H13 steel," *MRS Commun.*, vol. 12, no. 3, pp. 343–351, Jun. 2022, doi: 10.1557/s43579-022-00182-9.

13. C. Brown, **T. McCarthy**, K. Chadha, S. Rodrigues, C. Aranas, and G. C. Saha, "Constitutive modeling of the hot deformation behavior of CoCrFeMnNi high-entropy alloy," *Mater. Sci. Eng. A*, vol. 826, p. 141940, Oct. 2021, doi: 10.1016/j.msea.2021.141940.

Conference Presentations:

1. **T. McCarthy**, J. Pasco, and C. Aranas Jr, "Surrogate Modelling of Ti6Al4V Manufactured Via Pulsed Laser Powder Bed Fusion," presented at the International Conference on Materials Science and Engineering in the Philippines, 2025. (Oral Presentation)
2. **T. McCarthy**, J. Pasco, and C. Aranas Jr, "A Comparison of the Generalizability of Machine Learning and Constitutive Modeling of Flow Stress," presented at the TMS 2024 153rd Annual Meeting & Exhibition, 2024. (Poster Presentation)
3. H. Bongao, J. Pasco, **T. McCarthy**, K. Nyamuchiwa, and C. Aranas, "Softening Mechanisms in Additively Manufactured 420 Stainless Steel at Elevated

Temperatures," presented on behalf of H. Bongao at the TMS 2024 153rd Annual Meeting & Exhibition, 2024. (Oral Presentation)